ABSTRACT

Title of Dissertation: DIRECT NONLINEAR TRAJECTORY OPTIMIZATION AND STATE ESTIMATION FOR A TETHERED UNDERWATER ENERGY HARVESTING KITE

Debapriya Bhattacharjee
Doctor of Philosophy, 2022

Dissertation Directed by: Professor Hosam K. Fathy
Department of Mechanical Engineering

This dissertation addresses the coupled challenges of state estimation and trajectory optimization for a marine hydro-kinetic energy harvesting kite. The optimization objective is to maximize the kite's average mechanical power output. This work is motivated by the potential of "pumping-mode" tethered kites to provide attractive levelized costs of electricity, especially when cross-current motion is exploited to maximize energy harvesting. In "pumping-mode" kites, the kite is tethered to platform carrying a motor/generator, and electricity generation is achieved by reeling the kite out and in at high and low tether tension levels, respectively.

Marine hydro-kinetic (MHK) systems are heavily influenced by wind energy systems. In both contexts, for instance, tethered kites can be used for electricity generation instead of stationary turbines. Similar to airborne wind energy (AWE) systems, the power production capacities of MHK kites are heavily influenced by their flight trajectories. While trajectory optimization is a well-established research area for AWE systems, it is a nascent but growing field for MHK kites.

Moreover, although both AWE and MHK kites have the potential to benefit from trajectory optimization, the lessons learned from AWE systems might not be directly applicable to MHK kites, since MHK systems are often close to neutral buoyancy whereas AWE systems are not. Finally, there is little work in the literature that co-optimizes the spooling and cross-current trajectories of a pumping-mode MHK kite.

The first contribution of this dissertation is to explore the simultaneous optimization of the cross-current trajectory and the spooling motion of a pumping-mode kite using direct transcription. While the results highlight the degree to which simultaneous optimization can be beneficial for these systems, they also motivate the need for a solution approach that satisfies the constraints imposed by the kite dynamics exactly, as opposed to approximately. This leads to the second contribution of this dissertation, namely, finding an analytic solution to the inverse dynamics of the MHK kite, i.e., mapping a desired combination of kite position, velocity, and acceleration onto the corresponding actuation inputs. The dissertation then proceeds to its third contribution, namely, solving the kite trajectory optimization problem based on the above exact solution of the kite's inverse dynamics. The resulting simulation provides more realistic optimization results. However, all of the above work focuses on the special case where the free-stream fluid velocity is known and spatio-temporally constant. This motivates the fourth and final contribution of this dissertation, namely, the development of an unscented Kalman filter for simultaneously estimating both the kite's state and the free-stream fluid velocity. One interesting outcome of the estimation study is the finding that simple unscented Kalman filtering is not able to estimate the fluid velocity accurately without the direct measurement of the attitude of the kite.

DIRECT NONLINEAR TRAJECTORY OPTIMIZATION AND STATE
ESTIMATION FOR A TETHERED UNDERWATER ENERGY
HARVESTING KITE

by

Debapriya Bhattacharjee

Dissertation submitted to the Faculty of the Graduate School of the
University of Maryland, College Park in partial fulfillment
of the requirements for the degree of
Doctor of Philosophy
2022

Advisory Committee:
      Professor Hosam K. Fathy, Chair/Advisor
      Professor P.S. Krishnaprasad, Dean's Representative
      Professor Balakumar Balachandran
      Professor Christopher Vermillion
      Professor Eleanora Tubaldi

Table of Contents

List of Tables

List of Figures

Chapter 1:   Introduction

1.1   Vision and Motivation

More than half of the US population lives within 50 miles of the nation's coast, making marine hydro-kinetic (MHK) systems lucrative for renewable electricity generation [1]. MHK systems are particularly attractive in regions with fast ocean currents, such as the Gulf Stream. MHK systems convert the energy of (i) tides, (ii) waves, (iii) ocean currents, and (iv) the temperature difference between surface and deep water to electricity. As listed in Table 1.1, the annual average amount of energy that is hypothetically available from these resources, known as the *theoretical resource potential*, can range from 445 to 2,640 TW h per year depending on the resource [2]. Moreover, the *technical resource potential*, defined as the portion of the theoretical resource potential that can be practically harvested, can range from 45 to 1,298 TW h per year [2].

Table 1.1: Theoretical and Technical Resource Potentials of Marine Hydro-Kinetic Systems

Resource	Theoretical [TW h per year]	Technical [TW h per year]
Wave	$1594 - 2640$	$898 - 1298$
Tidal Stream	445	$222 - 334$
River Currents	1381	120
Ocean Currents	200	$45 - 163$

One approach for harvesting MHK energy generation is to deploy an energy harvesting

kite. The kite is attached to a launch platform using a tether, and can be configured to operate in one of two modes. In *drag mode*, the kite harvests energy using an onboard generator, and transmits it to the launch platform through an electrified tether. Alternatively, in *pumping mode*, a motor/generator on the platform periodically reels the kite out at high tension then reels it in at low tension, thereby generating positive net power. Figure 1.1 shows an illustration of a pumping mode MHK kite, which will be the focus of the dissertation.
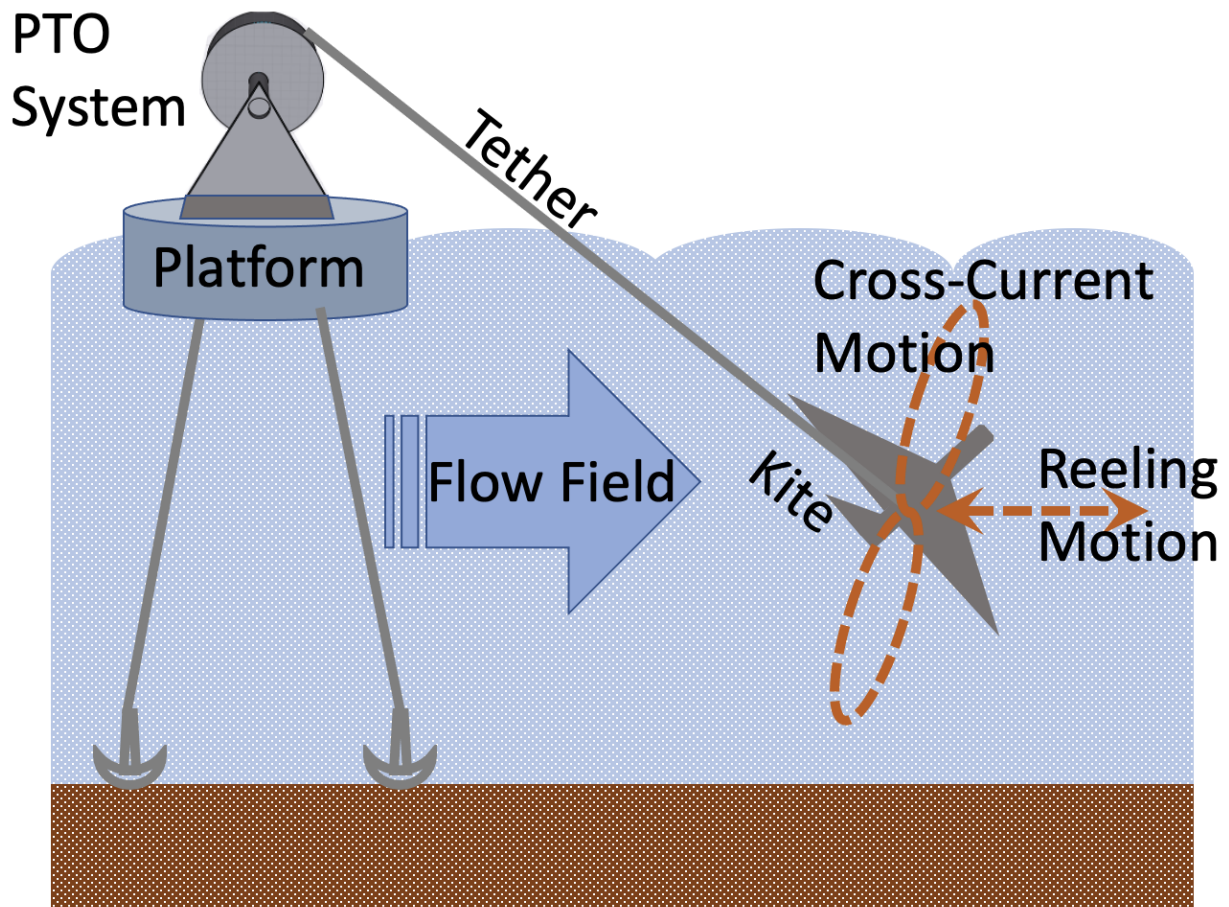
Figure 1.1: Illustration of a Pumping Mode MHK Kite

Tethered kites have significant advantages compared to towered turbines. Firstly, they can fly at cross-current speeds significantly faster than the prevailing flow, thereby generating power an order of magnitude higher than towered turbines. Secondly, they can reach greater distance

compared to turbines. For example, in the case aerial tethered kites are capable of reaching an altitude of 600m. This is important, considering the fact that at such an altitude, wind typically has five times the power density of wind at ground level [3]. As shown in Eq. (1.1), the power generated is a function of the magnitude of the true (i.e., free stream) fluid velocity, v_w, the reference area of the kite, A_{ref}, lift coefficient, C_L, fluid density, ρ, and a multiplicative factor, F representing the energy harvesting benefits of the specific kite configuration and trajectory [4].

$$P = \frac{1}{2}\rho v_w^3 A_{ref} C_L F \tag{1.1}$$

The literature shows that energy harvesting kites on average produce more power when flying in a cross-current motion, as opposed to remaining stationary [4]. Cross-current motion is defined as when the kite moves perpendicular to the free stream fluid velocity. Therefore, maximizing power production for such kites depends on (i) optimizing the kite trajectory for a given free stream fluid velocity and (ii) accurately estimating this fluid velocity. Maximizing the net power output of a pumping mode MHK kite requires the simultaneous co-optimization of the cross-current trajectory and the spooling (reel in/reel out) motion. This dissertation addresses the interrelated challenges of: (i) the simultaneous optimization of the cross-current trajectory and spooling motion of an MHK kite using various methods; as well as (ii) estimating the kite's state and free stream fluid velocity using an unscented Kalman filter. The remainder of this chapter reviews the existing literature on these two topics, thereby motivating the dissertation's contributions.

3

1.2 Literature Review

1.2.1 Optimization of Tethered Kites

There is a rich existing literature on the modeling, optimization, and control of tethered kites. This literature spans both marine hydro-kinetic (MHK) and airborne wind energy system (AWES) applications. The models have various levels of fidelity and complexity. For example, previous research by Li *et al.* modeled a tethered kite as a six degree-of-freedom (dof) aircraft that incorporated rotational pitch, roll, and yaw dynamics, and utilized a Lyapunov based controller for the translational and rotational motions [5], [6]. Later work incorporated added mass effects to accurately capture fluid-structure interactions [7]. Vermillion *et al.* also presented a 6-dof model that was validated experimentally both in air and in water channel experiments [8], [9]. Denlinger *et al.* later used the water channel experiment data to develop a 2-dof model of the tethered kite, whose trajectory was optimized online through extremum seeking control [10]. Taking into account the kite's added mass and inertia, Cobb *et al.* built a "unifoil" MHK kite model, which was later extended to a 6-dof model [11], [12]. Canale *et al.* introduced a model of a pumping mode kite and used it to optimize the kite's trajectory through model predictive control [13], [14], [15]. Numerical optimization via a direct multiple shooting method was used by Houska and Diehl for both a power generating and a towing kite [16], [17]. Estimating the velocity vector orientation using a target switching strategy, Wood *et al.* built a tracking controller for an autonomous kite [18], [19]. Rapp *et al.* designed a cascaded controller complete with an aircraft, tether, and ground station model [20], [21]. Finally, Reed *et al.* explored the problem of building a hierarchical controller for a marine tethered kite in a turbulent flow environment [22], [23]. This

hierarchical control work reflects the growing realization in the research community of the importance of different feedback control methods for ensuring the robust management of tethered energy-harvesting kite flight, particularly given the importance of such robustness for ultimate commercial deployment. Hierarchical feedback control is also valuable for ensuring that the true physical control inputs for a given kite system (e.g., aileron, elevator, and rudder actuation angles, etc.) are manipulated in a manner that tracks desired trajectories of higher-level variables (e.g., angle of attack, induced roll angle, etc.). This, in turn, makes it possible to focus higher-level trajectory optimization research on simplified problem settings with higher-level actuation commands: an approach that this dissertation adopts by treating the kite's induced roll angle, angle of attack, and tether tension as the kite's "control inputs". Finally, in recent years, there has been a push to commercialize energy harvesting kites by companies including Minesto, WindLift, and Makani [24], [25], [26].

As mentioned in Section 1.1, maximizing the net power of a pumping mode kite requires the optimization of both the cross-current trajectory and the spooling motion. Existing work in the literature examines important subsets of this problem, such as: (i) optimizing the spooling motion and the trajectory separately as in [15], [27], [28]; or (ii) optimizing just the spooling motion as in [29]; or (iii) optimizing the spooling motion and the path (as opposed to the trajectory) simultaneously, as in [11], [30]. Different representations of system dynamics are used in these optimization studies. For example, [30] and [31] incorporate tether dynamics into the main plant models, whereas [32] presents a model-free optimization strategy.

A significant part of the above literature focuses on characterizing and solving the *forward* kite dynamics, often with the goal of optimizing these dynamics (e.g., by optimizing the kite trajectory). Given a kite's position, velocity, and actuation inputs, the equations governing its

forward dynamics furnish its accelerations. Solving the corresponding *inverse* dynamics, in the sense of being able to map a desired combination of kite position, velocity, and acceleration onto the corresponding actuation inputs, is equally important for multiple reasons. First, knowledge of a kite's inverse dynamics enables easy vetting of any prescribed trajectories, i.e., determination of whether the trajectories are feasible. Moreover, if the trajectories are not feasible, the inverse dynamics can provide insights into why they are infeasible. Second, the solution to the inverse kite dynamics problem is not necessarily unique, which means that solving these inverse dynamics analytically provides insight into the multiplicity of possible solution arcs. Third, an analytic solution to the inverse dynamics problem can be quite valuable for solving trajectory optimization, online estimation, and tracking control problems, both exactly and in a computationally tractable manner. Initial work by the author, included in this dissertation, examined the problem of optimizing energy harvesting kite trajectories using direct transcription methods [33]. Such optimization required the approximate solution of inverse kite dynamics. Such an approximate inverse dynamics solution can be obtained using tools such as the DASSL solver in OpenModelica [34], but adds to the computational complexity of the optimization approach. This motivates the need for an exact analytic solution of the kite's inverse dynamics, as presented in this dissertation.

1.2.2 Estimation of States and Fluid Velocity

The optimal flight trajectory of a given MHK kite depends on the surrounding free stream fluid velocity. Initial work by the author, presented in this dissertation, examines the special case where this velocity is both known and spatio-temporally constant [35], [36]. Other re-

search in the literature examines trajectory optimization and/or adaptation in the presence of a spatially and/or temporally varying flow field. For instance, work by Cobb *et al.* uses wind profiles from NREL [37], [38] and the Mid-Atlantic Bight South-Atlantic Bight Regional Ocean Model [11], [12]. The most common free stream fluid velocity modeling approach in the MHK literature has been the use of simple fluid flow models that describe vertical flow shear, i.e., the change in fluid velocity with height, [39], [13], [15]. Beyond this modeling and optimization work, there is a critical need for research on online fluid flow field estimation for tethered energy harvesting kites. Such fluid flow estimation has been explored in towered turbine and aircraft/unmanned aerial vehicle (UAV) literature, as discussed below, but is a relatively nascent field for underwater kite systems, with some initial work by investigators including Leonard et a. [40].

Light Detection and Ranging (LIDAR) systems have been widely used in the literature to measure different aspects of the wind field for a singular wind turbine and for wind farms. There is a robust field of literature that looks into flow field estimation based on LiDAR measurements. In [41], Kapp *et al.* presented an algorithm that produces wind field parameter estimates using a single scanning, hub based, continuous wave Light Detection and Ranging (LiDAR) device. The parameters were: averaged streamwise wind speed, linear horizontal and vertical shear, and averaged horizontal and vertical stream direction. The paper assumed that the wind speed in a two-dimensional measurement plane upwind the turbine is perfectly measurable. Using two wind speeds in this plane, a wind vector projection was calculated, which is then used to estimate the parameters. Tower and Jones in [42] used Unscented Kalman Filtering to estimate the wind field upstream of the turbine. In this work, a dual-beam LiDAR measured the radial velocity of the true wind field at regularly spaced ranges and discrete time instants. Since the Unscented

Kalman Filter requires a wind model, the paper derived a low-fidelity simplified model from the Navier-Stokes equation. The state variables for the above model were the radial and azimuthal wind velocities.

The above approaches deal with estimating the wind flow for individual turbines. A rich literature in estimating the wind flow in a wind farm has also been developed. Doekemeijer *et al.* [43], designed a state estimator using Ensemble Kalman Filtering to reconstruct the states of a flow model described in [44]. The model used is of medium fidelity and is based on an unsteady two-dimensional Navier Stokes equation that has been discretized temporally and spatially. It predicts the 2D velocity vectors and pressure terms over a predefined grid in a wind farm at hub height at discrete time instants. It relies on actuator disk theory to model interactions between turbines and their surrounding flow. The state variables of the model were the two-dimensional flow velocity vector terms and the pressure at hub height. The measurements for the model were a subset of the state vector: the longitudinal and lateral flow velocity at a small number of points in the wind field. Previously, the authors had used Ensemble Kalman Filtering and Approximate Kalman Filtering to build an estimator that would reconstruct the states based on the same model [45]. The overarching goal of both these studies was to build a close-loop dynamic-model based controller for the wind farm.

The above methods deployed in wind turbines cannot be used to estimate the fluid speed for marine hydro-kinetic kites, mainly because of the reliance on LIDARs, which cannot be used underwater. The literature on unmanned aerial vehicles and aircraft, however, shows that it is possible to estimate fluid flow without the use of LIDARs. Wind flow estimation techniques in the field of unmanned aerial vehicles (UAVs) and aircraft can be categorized as employing: (i) graphical methods employing the velocity triangle vector [46], [47], [48], [49], (ii) constant

8

wind models plus Kalman filtering [48], [50], (iii) time varying wind models without Kalman filtering [51], and (iv) time varying wind models with Kalman filtering [52]. All four methods require the knowledge of the ground speed of an aircraft or UAV from radar or GPS. However, since GPS sensors are not usable underwater, these methods cannot be used to estimate the fluid speed of a marine hydro-kinetic kite.

1.2.3   Open Challenges and Contribution

The above review shows that there is a rich existing literature in the areas of AWES and/or MHK kite trajectory optimization, state estimation, and surrounding flow field estimation. However, multiple challenges remain relatively unexplored, including the four main challenges addressed in the next four chapters of this dissertation, respectively. First, the literature shows extensive efforts in the area of both AWES and MHK kite trajectory optimization. However, to the best of the authors' knowledge, pumping system trajectory co-optimization (i.e., the simultaneous optimization of spooling and cross-current motions) remains unexplored in the MHK literature. Moreover, insights from AWE system co-optimization may not be directly translatable to the MHK literature due to the contrast between MHK kites (which are typically close to neutral buoyancy) versus AWE kites (which are often heavier than air). Second, there is need for an analytic solution to the inverse dynamics of a tethered MHK kite. Such a solution can enable more computationally efficient trajectory optimization, state estimation, and tracking control. Third, there is a need to examine the MHK kite trajectory optimization problem using the above analytic solution of its inverse dynamics, in order to ensure accurate optimization results. Fourth, there is a need for online algorithms to estimate the state and surrounding flow field for a given MHK

kite. Each of these problems is a focus of a contribution of this dissertation, as discussed in the next four chapters.

Chapter 2: Co-optimization of the Spooling Motion and Cross-Current Trajectory of an Energy Harvesting Marine Hydro-kinetic Kite using Direct Transcription

2.1 Overview

This chapter addresses the challenge of simultaneously optimizing the spooling motion and cross-current trajectory of a tethered MHK kite. The co-optimization work in this chapter is adapted from a peer-reviewed publication by the dissertation's author [33]. This co-optimization work builds on a simple physics-based kite model developed in a peer-reviewed publication by Dr. Miguel Alvarez, in collaboration with this dissertation's author [34]. The chapter presents this physics-based model, the direct transcription algorithm used for co-optimization, and finally a discussion of the co-optimization results.

The work in this chapter is motivated by the potential of tethered kites to provide attractive levelized costs of electricity, especially when cross-current motion is exploited in order to maximize energy harvesting. The literature explores trajectory optimization for tethered energy harvesting, for both airborne and marine hydro-kinetic energy systems. However, as explained in the previous chapter, the simultaneous co-optimization of both the spooling and cross-current trajectories of a marine hydro-kinetic kite remains relatively unexplored. The chapter formulates

this co-optimization problem using a 3 degree-of-freedom kite model, coupled with an inelastic tether. A Fourier series expansion is then used for solving this co-optimization problem, and the key features of the resulting optimal trajectory are analyzed. Significant energy harvesting is achieved through co-optimization, approaching theoretical maximum power for cross-current systems.

2.2 Equations of Motion

The kite model used in this chapter approximates the kite's tether as a massless, drag-free straight-line kinematic connector between the kite and the launch platform. Previous work by Alvarez et al. suggests that this is a reasonable approximation, compared to an alternative model that uses a PDE representation to capture the dynamics of the tether's distributed inertia and compliance [34]. The kite is modeled with the following assumptions:

1. The kite's motion can be controlled through the manipulation of its angle of attack, induced roll angle, and the magnitude of the tether tension force.

2. The kite is neutrally buoyant, *i.e.*, there is zero net impact of gravitational and buoyancy forces on the kite.

The first assumption enables the modeling of the kite as a point mass in three dimensions. Building such a point mass model implicitly assumes the presence of lower-level controllers capable of manipulating the kite's rotational dynamics to achieve the desired angle of attack and induced roll angle. This implicit assumption is reasonable if the kite's rotational dynamics are controllable and its closed-loop attitude dynamics are sufficiently fast compared to the desired

rates of change of its angle of attack and induced roll angle. The second assumption implies that the most important forces acting on the kite are tether tension and hydrodynamic forces such as lift, drag, and the side force. The remainder of this chapter ignores the side force acting on the kite, implicitly assuming that the kite's yaw dynamics induce a fast and stable weathercock effect.

In order to model the system, two coordinate systems are defined: (i) an inertial Cartesian coordinate system with the origin at the tether anchor point and (ii) a traditional "wind frame" coordinate system. The anchor point is assumed to be sufficiently deep underwater to the point where the kite remains fully submerged throughout its trajectory. The position $\vec{r}$ and velocity $\vec{V}$ of the kite are defined in the inertial xyz frame, as follows.

$$\vec{r} = x\hat{\imath} + y\hat{\jmath} + z\hat{k} \tag{2.1}$$

$$\vec{V} = \dot{x}\hat{\imath} + \dot{y}\hat{\jmath} + \dot{z}\hat{k} \tag{2.2}$$

A unit vector, $\hat{e}_r$, is defined in the direction of the kite position:

$$\hat{e}_r = \frac{\vec{r}}{\|\vec{r}\|} \tag{2.3}$$

It is assumed that the free-stream water velocity vector, $\vec{V}_w$ is in the x-direction of the inertial frame. The apparent velocity that the kite experiences, $\vec{V}_{rel}$, is then defined as the difference between the kite and fluid velocities.

13

$$\vec{V}_w = u_w \hat{\imath} \tag{2.4}$$

$$\vec{V}_{rel} = (\dot{x} - u_w)\hat{\imath} + \dot{y}\hat{\jmath} + \dot{z}\hat{k} \tag{2.5}$$

The second coordinate system is the fluid or "wind" frame. The x-direction in this fluid frame, $\hat{x}_w$, is defined as the unit vector in the direction of the apparent velocity. Moreover, the y-direction, $\hat{y}_w$, is chosen to be orthogonal to both $\hat{x}_w$ and $\hat{e}_r$: a well-posed definition as long as the apparent fluid velocity is not parallel to the tether. Finally, the unit vector $\hat{z}_w$ is chosen to create a Cartesian fluid frame.

$$\hat{x}_w = \frac{\vec{V}_{rel}}{\|\vec{V}_{rel}\|} \tag{2.6}$$

$$\hat{z}_w = \frac{\hat{x}_w \times \hat{e}_r}{\|\hat{x}_w \times \hat{e}_r\|} \tag{2.7}$$

$$\hat{y}_w = \frac{\hat{z}_w \times \hat{x}_w}{\|\hat{z}_w \times \hat{x}_w\|} \tag{2.8}$$

The tension force, $\vec{T}$, and drag force, $\vec{D}$, act along and in the opposite direction to the unit vectors $\hat{e}_r$ and $\hat{x}_w$, respectively. The lift force, $\vec{L}$, is always perpendicular to the drag force and therefore lies in a plane perpendicular to $\hat{x}_w$. Therefore, these forces can be expressed as follows:

$$\vec{L} = \frac{1}{2}\rho C_L(\alpha)A\|\vec{V}_{rel}\|^2(\cos\tilde{\phi}\hat{y}_w + \sin\tilde{\phi}\hat{z}_w) \tag{2.9}$$

$$\vec{D} = -\frac{1}{2}\rho C_D(\alpha)A\|\vec{V}_{rel}\|^2\hat{x}_w \tag{2.10}$$

$$\vec{T} = T\hat{e}_r \tag{2.11}$$

where $\rho, C_L, C_D, \alpha, A,$ and $\tilde{\phi}$ are, respectively, the water density, the lift coefficient, the drag coefficient, the angle of attack, the wing area, and the induced kite roll angle with respect to the $\hat{y}_w$ unit vector. The density of water and the area of the kite are $1000 kg/m^3$ and, $10m^2$ respectively. The drag and lift coefficients are computed for a representative MHK kite geometry using the curve fits in Equation (2.12) and (2.13), where the angle of attack, α is assumed to be in degrees and the values of $a, b, p_1, p_2,$ and p_3 are $3.123\times10^{-2}, 6.675\times10^{-2}, 1.221e\times10^{-4}, 5.309\times 10^{-4},$ and 0.01 respectively.

$$C_l = 2(\alpha a + b) \tag{2.12}$$

$$C_d = 2(\alpha^2 p_1 + \alpha p_2 + p_3) \tag{2.13}$$

Therefore, the total force acting on the kite is

$$\vec{F}_{total} = \vec{L} + \vec{T} + \vec{D} \tag{2.14}$$

Taking $\tilde{\phi}, \alpha,$ and T as input variables, the kite's state equations can be written as in Equation (2.15). The mass of kite, m, is $1000 kg$.

$$\frac{d}{dt}\begin{bmatrix} x \\ y \\ z \\ u \\ v \\ w \end{bmatrix} = \begin{bmatrix} u \\ v \\ w \\ \frac{1}{m}\vec{F}_{total} \cdot \hat{i} \\ \frac{1}{m}\vec{F}_{total} \cdot \hat{j} \\ \frac{1}{m}\vec{F}_{total} \cdot \hat{k} \end{bmatrix} \tag{2.15}$$

Since, the tether tension can be controlled by through spooling, the optimization problem is effectively a spool rate control problem.

2.3   Optimization Approach

Based on the state equations presented in Section 2.2, the optimization statement can be written as follows:

$$\min J = \frac{1}{t_f - t_i}\begin{Bmatrix} -\int_{t_i}^{t_f} P_{mech} dt \\ \int_{t_i}^{t_f} (\dot{\tilde{\phi}}^2 + \dot{\alpha}^2 + \dot{\xi}^2) dt \end{Bmatrix} \tag{2.16}$$

subject to the kite's state-space model as a dynamic constraint, with the following added con-

straints:

$$\vec{X}_{t_i} = \vec{X}_{t_f} \tag{2.17}$$

$$P_{mech} = \vec{T}^T\vec{V} \tag{2.18}$$

$$T = T_{min} + (T_{max} - T_{min})\frac{e^\xi}{1 + e^\xi} \tag{2.19}$$

This is a classical multi-objective, or Pareto, trajectory optimization problem statement, with a vector of two potentially competing optimization objectives. The first objective is to maximize the time-averaged value of P_{mech}, the mechanical power produced at every instant in time over the course of the spooling cycle. Averaging is performed over one time period, where t_i is the initial time and t_f is the final time. One time period is defined as the total time taken for the kite to reel in and reel out once. Equation (2.17) therefore ensures the periodicity of the states, with $\vec{X}_t$ representing the state vector at any time t. Optimization proceeds with respect to the time histories of the state and control input variables, as well as the time period, $t_f - t_i$. Tether tension, T, is one of the kite system's control input variables. However, a sigmoidal nonlinear coordinate transformation is used for expressing this tension as a function of a new, fictitious control input variable ξ. This makes it possible to force the tether tension to remain between two bounds: a lower bound T_{min} that prevents undesirable tether slack, and an upper bound T_{max} that prevents undesirable mechanical failure. The second optimization objective is the sum of the mean square rates of change of the kite's three actuation/control inputs. Penalizing the time rates of change of the three inputs to the kite dynamics model is important for achieving a smooth motion trajectory. From a mathematical perspective, one consequence of this rate penalty is that the true control input variables are now the rate variables, $\dot{\phi}$, $\dot{\alpha}$, and $\dot{\xi}$.
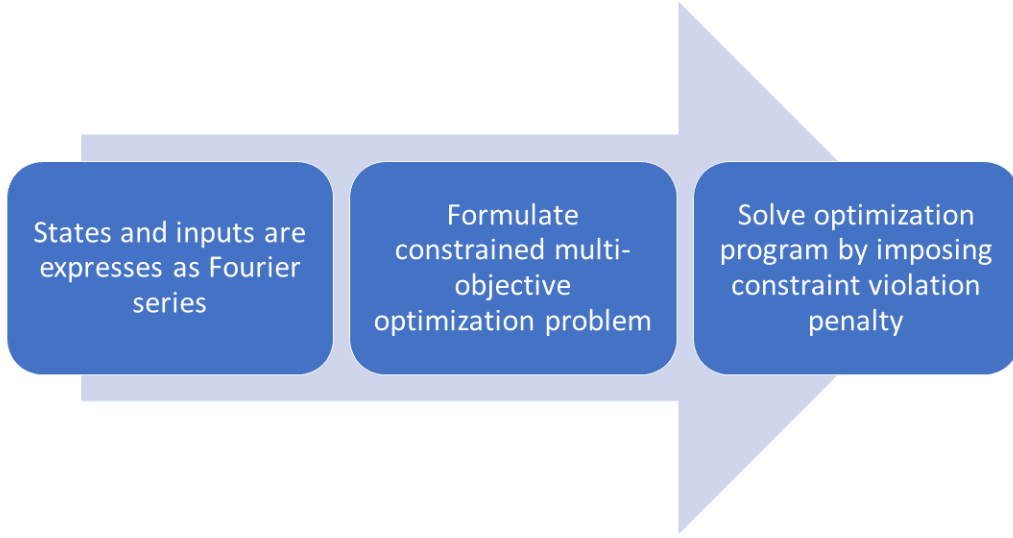
17

Figure 2.1: Power Maximization Algorithm

Figure 2.1 provides a high-level representation of the process used for solving the above optimization problem. The key idea behind this process is to utilize a series expansion method to convert the problem into a nonlinear program. Since this is a periodic optimal control problem, we use truncated Fourier series to represent the state and control input trajectories, as shown below:

$$\vec{X} = \frac{\vec{a}\,(0)}{2} + \sum_{n=1}^{3} \left[\vec{a}\,(n) \cos \frac{2\pi n}{T_{period}} + \vec{b}\,(n) \sin \frac{2\pi n}{T_{period}} \right] \tag{2.20}$$

$$\vec{U} = \frac{\vec{c}\,(0)}{2} + \sum_{n=1}^{3} \left[\vec{c}\,(n) \cos \frac{2\pi n}{T_{period}} + \vec{d}\,(n) \sin \frac{2\pi n}{T_{period}} \right] \tag{2.21}$$

18

In the above Fourier expansions, the vectors $\vec{X}$ and $\vec{U}$ represent the state and input vectors of a new state-space system model driven by the rate variables, $\dot{\tilde{\phi}}$, $\dot{\alpha}$, and $\dot{\xi}$. The vectors $\vec{a}(n)$, $\vec{b}(n)$, $\vec{c}(n)$, and $\vec{d}(n)$ are expansion coefficients corresponding to the nth harmonic of the Fourier expansion. The period of the Fourier series is $T_{period} = t_f - t_i$, and optimization is performed over three harmonics for simplicity. This Fourier expansion approach allows for the optimization of the initial kite position and velocity, as part of trajectory optimization. Thus, the set of optimization variables now consists of the coefficient vectors $\vec{a}(n)$, $\vec{b}(n)$, $\vec{c}(n)$, and $\vec{d}(n)$ and the period T_{period}. These optimization variables cannot be chosen freely, one reason being that collectively, the state and control input trajectories must satisfy the underlying state-space model's dynamics. One possible remedy to this challenge is to define a "discrepancy cost" reflecting inconsistencies between the state and control trajectory Fourier expansions. Specifically, as shown in Figure 2.1, one can use the kite's equations of motion to compute the force, $\vec{F}_{req}(t)$, required for the perfect instantaneous achievement of the Fourier expansion of the kite state trajectory at every instant in time. One can also use the kite's equations of motion to compute the net force, $\vec{F}_{net}(t)$, that would act on the kite at every instant in time if the Fourier expansions of both the state and control input trajectories were simultaneously implemented. The L_2 norm of the discrepancy between these two force vectors can then provide a quantification of constraint violation, as shown below:

$$J_{discrepancy} = ||\vec{F}_{req}(t) - \vec{F}_{net}(t)||_2^2 \tag{2.22}$$

Given the above definition, this chapter solves the kite trajectory optimization problem as a multi-objective problem where a penalty on the discrepancy cost in Equation (2.22) is used

in order to enforce constraint satisfaction. Doing so converts the chapter's constrained optimization problem into an unconstrained problem with a constraint violation penalty, consistent with penalty-based approaches to constrained nonlinear programming. The chapter uses a linear scalarization approach to convert the problem's two competing objectives (namely, maximizing power and minimizing the rates of change of the input variables) into a single aggregate objective. This aggregate objective is a weighted sum of the two individual objectives, with the weights both being equal to unity throughout the remainder of the chapter. The nonlinearity of the kite's dynamics causes this trajectory optimization problem to be non-convex. A particle swarm algorithm is used for the initial exploration of the optimization space. This is followed by the use of the Nelder-Meade simplex algorithm for the local refinement of the particle swarm solution.

2.4   Results

This section presents simulation results showing that the chapter's optimization algorithm paired with the 3-DOF MHK kite model is successful in maximizing mechanical power. Per Loyd's calculation in [4], a kite of the area considered in this study is theoretically capable of producing 83.9kW of power in cross-current reel-out flight, assuming a free-stream flow speed of $1m/s$. The corresponding optimal steady reel-out speed is $\frac{1}{3}m/s$. It should be noted that this 21.3kW is quite optimistic for a number of reasons, including the fact that a practical kite cannot be reeled out indefinitely and cannot achieve purely cross-current motion.

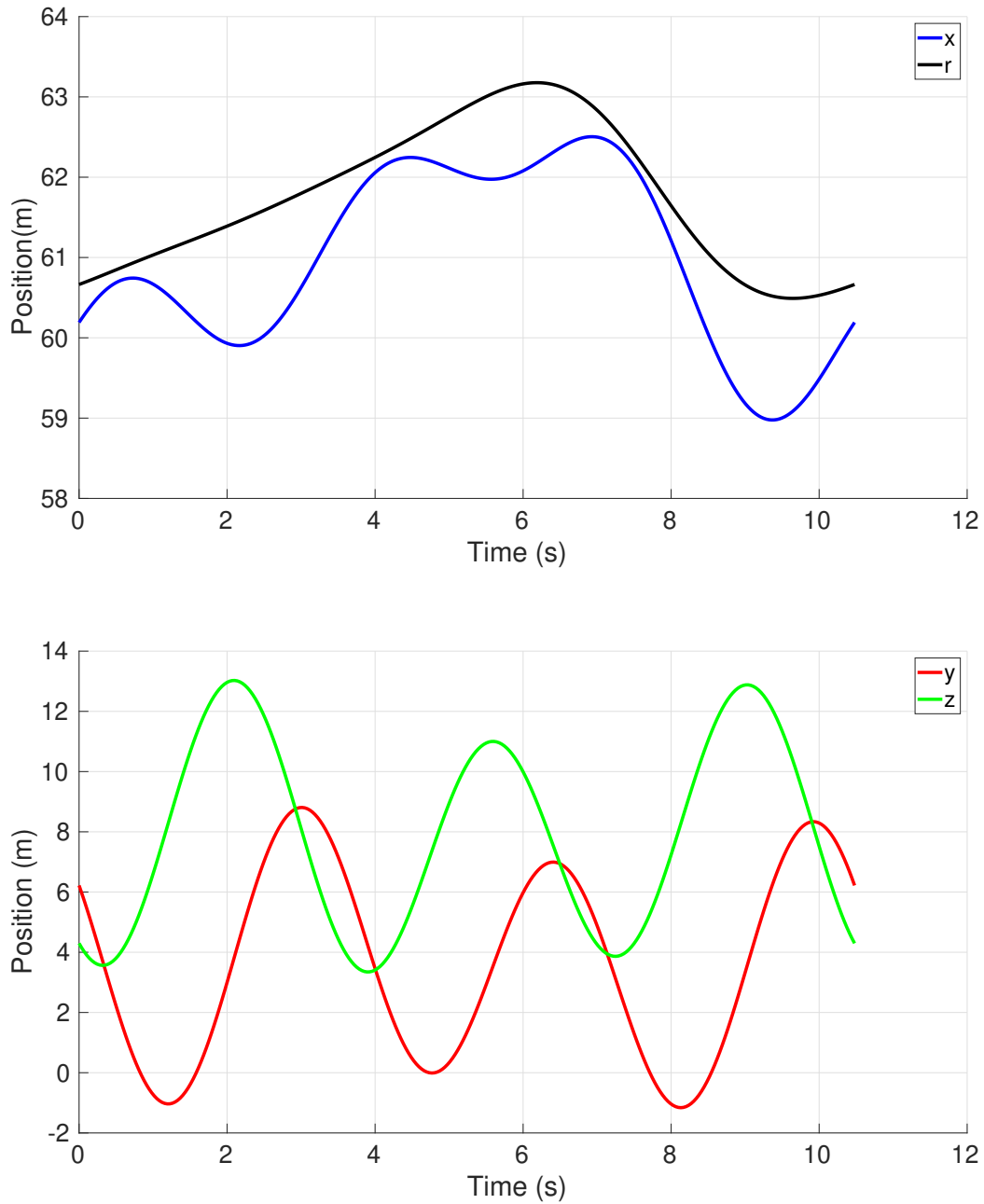The following observations can be made from the simulation results:

Figure 2.2: Position of Kite with Time

1. The optimizer successfully furnishes a smooth kite trajectory with a fairly short time period of approximately 10.5 seconds, as shown in Figure 2.2.

2. The optimal spooling trajectory is very simple, consisting of a spool-out episode followed

by a spool-in episode, as evident from the plot of radial kite distance, r, from the origin in

Figure 2.2.

3. The average tether reel-out rate in Figure 2.3 is close to the ideal theoretical value of $\frac{1}{3}m/s$

   predicted by Loyd.

4. The contrast between the kite's velocities in the x, y, and z directions, visible in Figure 2.3,

   highlights the degree to which the kite exploits the energy harvesting benefits of cross-

   current motion. The kite's velocity in both the y and z directions is very substantial, even

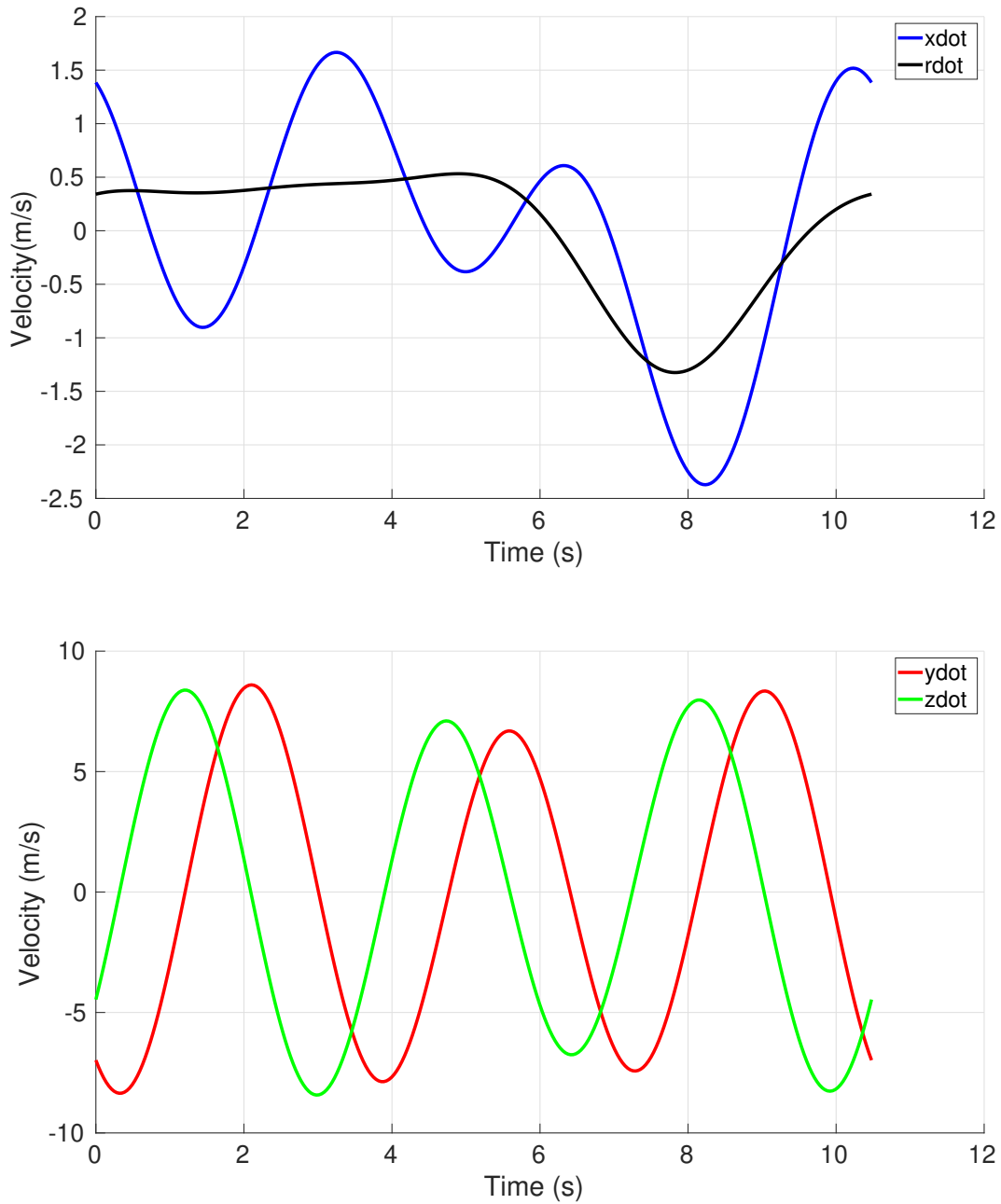   as its velocity in x direction remains small.

Figure 2.3: Velocity of Kite with Time

5. The trajectory shape as seen in Figure 2.4 is not a figure-8, as is common in literature. Since the kite is neutrally buoyant, the safety benefits of a figure-8 trajectory where the kite always "tacks" upwards are not critical, and not reflected in the optimization problem

formulation. The optimal trajectory, when projected onto the yz plane, can be intuitively approximated as a set of concentric circles. This trajectory reflects the optimization problem's emphasis on minimizing the rate of change of the induced kite roll angle, $\tilde{\phi}$. We also notice that the the radius of curvature at instant of time is very tight. This is due to the significant unmodeled variation in relative velocity across the wingspan and potentially unrealistic yaw rates. The first cause leads to errors in lift modeling and unmodeled local stall at different points along the wingspan.
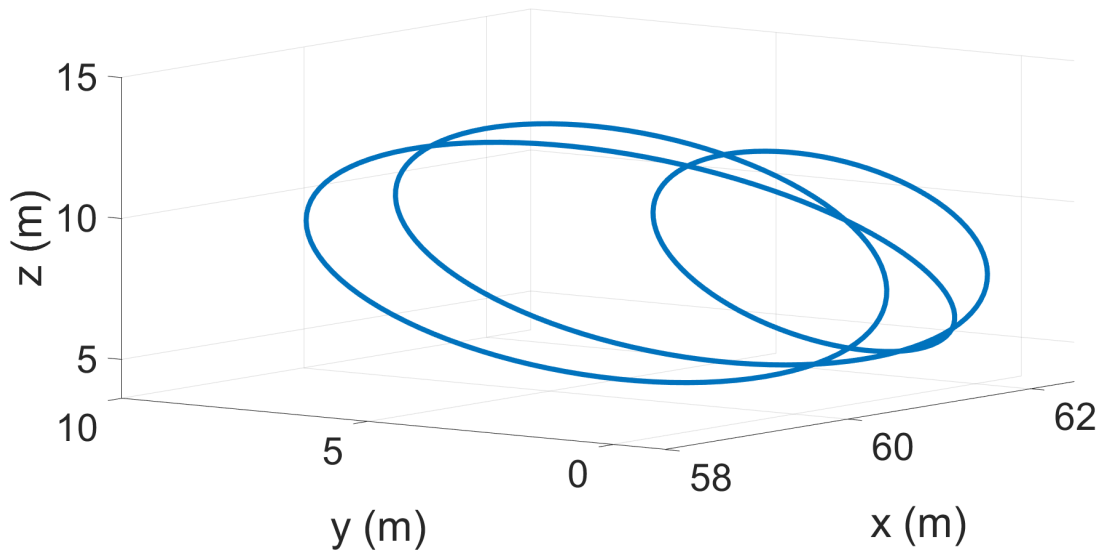

Figure 2.4: Optimized Path Shape

6. The induced roll angle $\tilde{\phi}$ never changes sign during the periodic kite trajectory, as shown in Figure 2.5. The magnitude of this roll angle is most substantial during reel in, when a sharp increase in the roll angle causes the tether tension and lift vectors to be misaligned, thereby enabling low-tension reel-in.
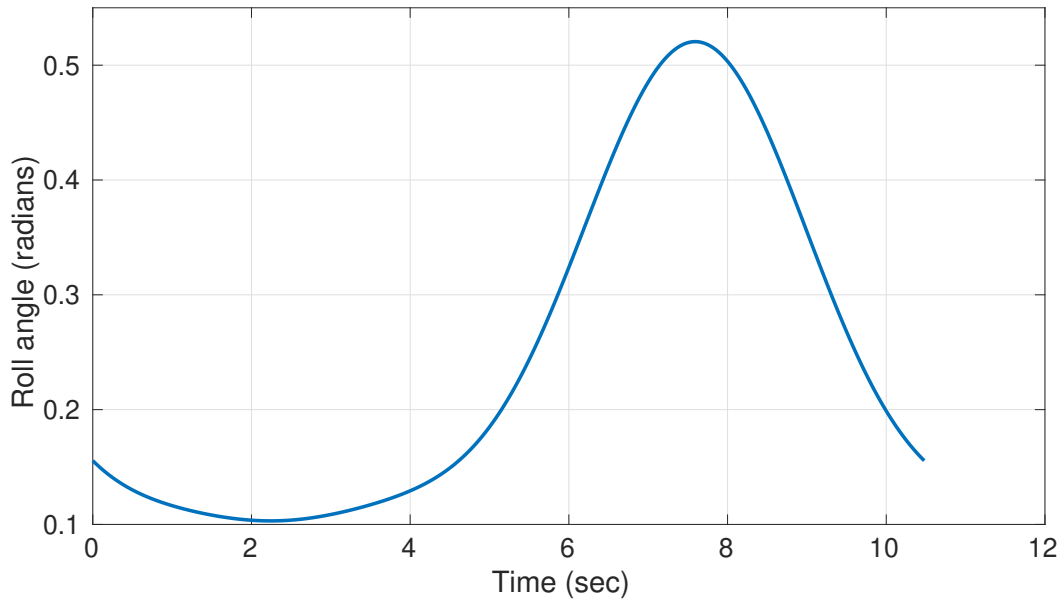
Figure 2.5: Roll Angle of the Kite with Time

7. As Figure 2.6 shows, the kite's lift-to-drag ratio attains a maximum value at an angle of attack close to 5 degrees. The optimal trajectory exploits this as follows. During reel-out, it achieves an angle of attack of approximately 4 degrees, as shown in Figure 2.7, thereby attaining a lift-to-drag ratio close to the maximum achievable ratio. This allows lift, and therefore tether tension, to be maximized. In contrast, during reel-in, a negative angle of attack is used in order to minimize lift, thereby minimizing tension.
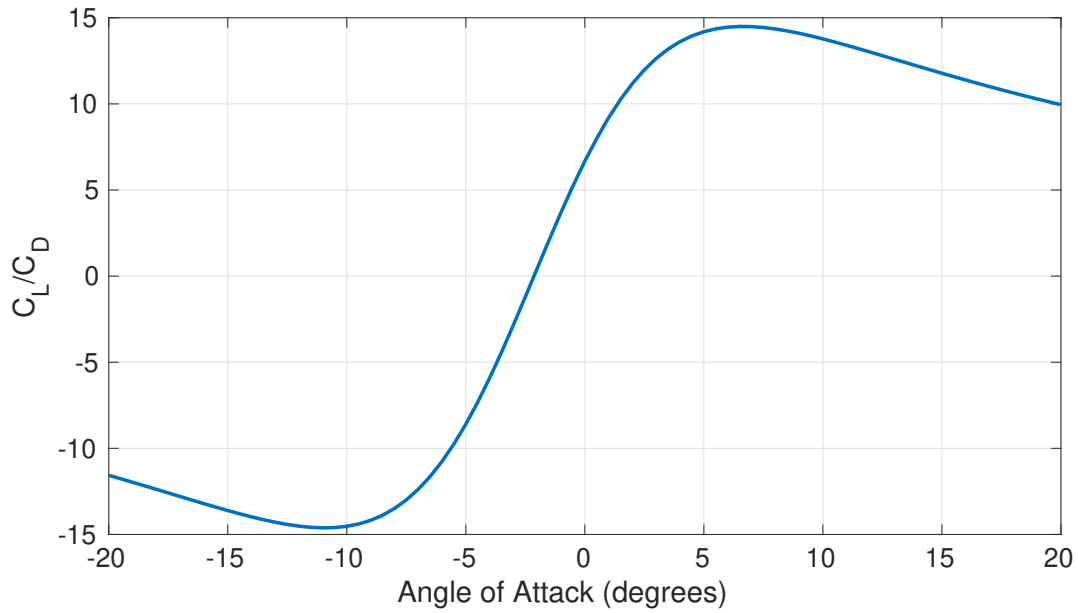
Figure 2.6: Variation of the Lift-to-Drag Ratio with Angle of Attack

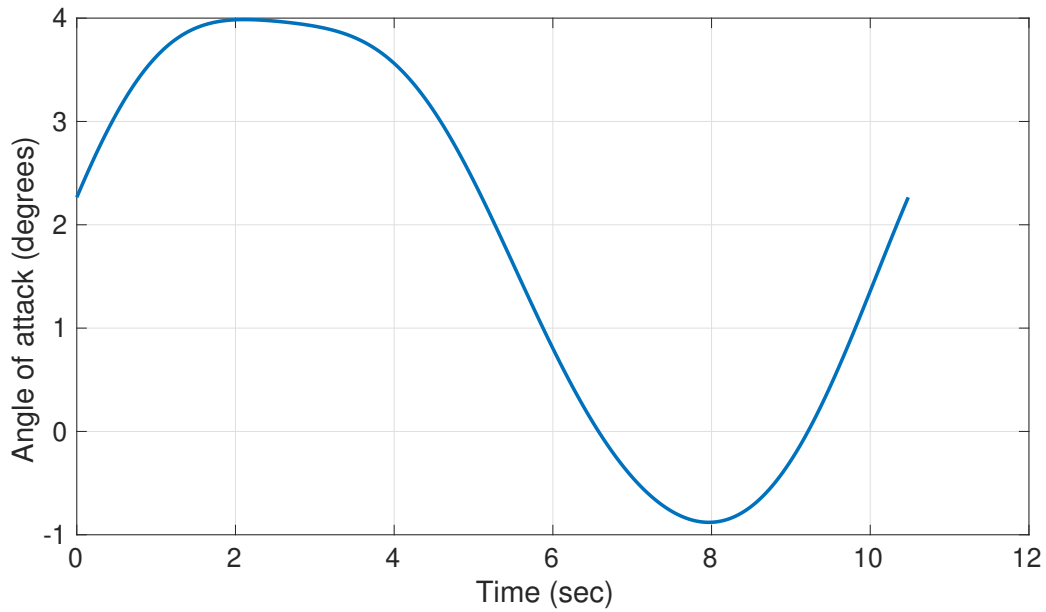

Figure 2.7: Angle of Attack of the Kite with Time

8. Tether tension is high during reel-out and low during reel-in, thanks to the above fluctua-

   tions in angle of attack with time. Moreover, the resulting lift force is used more heavily for

turning during reel-in compared to reel-out, thanks to the above fluctuations in the induced roll angle with time. The kite manipulates its attitude to exploit lift for power generation during reel-out and for turning during reel-in.
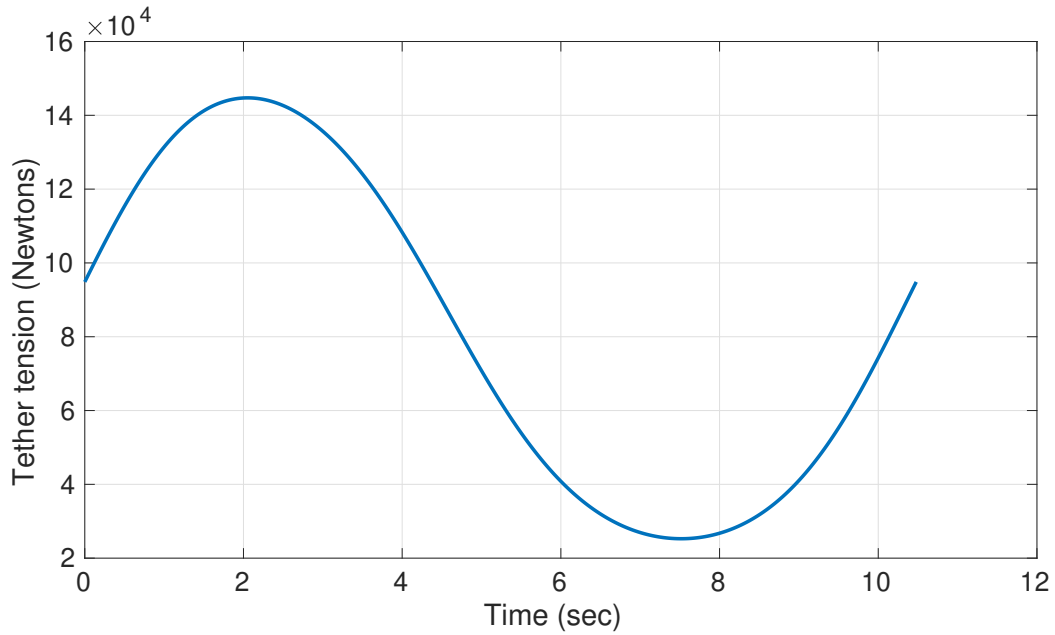

Figure 2.8: Tether Tension of the Kite with Time

9. The above trajectory furnishes substantial power during reel-out and consumes much less power during reel-in, as shown in Figure 2.9.
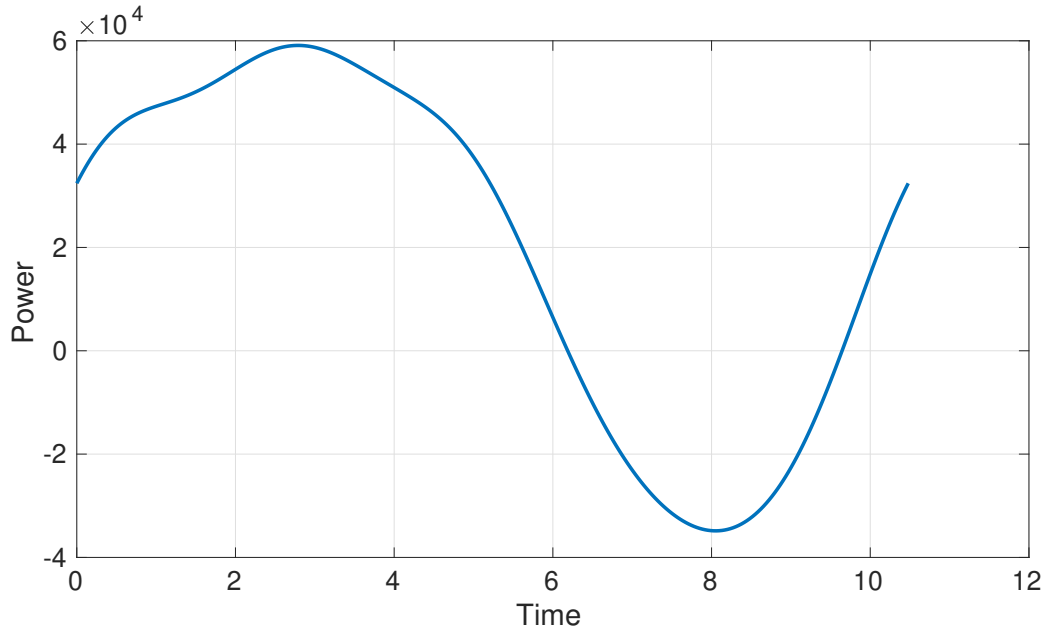
27

Figure 2.9: Power Trajectory of the Kite with Time

2.5   Discussion and Conclusions

It has been widely noted that AWE systems produce more power on average during cross-current motion than stationary flight. This chapter highlights the fact that this is true for MHK systems as well. Moreover, the chapter's results highlight the degree to which trajectory co-optimization can be beneficial for these systems. It is particularly important to note the manner in which variables describing the kite's cross-current motion (such as its angle of attack and induced roll angle) are coordinated with its spooling motion in order to facilitate optimal energy harvesting.

Beyond the optimization work in this chapter, the performance of practical MHK systems is likely to be further constrained by actuator dynamics, lower-level controllers for the system's actuators, unmodeled fluid-structure interactions, and tether dynamics. Analyzing these effects, both in simulation and experimentally, is an important potential future direction for MHK kite

research. One important potential future research question, for instance, is how much the results of this optimization study change when added fluid mass effects are modeled. Another important potential future research question is whether accounting for tether slack, perhaps through a switching model of tether dynamics, can alter the optimization results in this chapter significantly. Finally, the fact that the optimization results in this chapter rely on the use of a penalty function to approximate the kite's dynamics raises an important question, namely: can this chapter's optimization study be repeated using an exact solution of the kite's dynamics? To address this question, the next chapter of this dissertation presents an analytic solution of the inverse kite dynamics, thereby enabling a more accurate subsequent optimization study in the following chapter.

Chapter 3:   An Analytic Solution to the Inverse Dynamics of an Energy Harvesting Tethered Kite

3.1   Overview

This chapter presents and discusses an analytic solution to the inverse dynamics of a tethered MHK kite. The work in this chapter is adapted from a peer-reviewed journal article by the author [35]. The intent of this work is to enable the optimization of MHK kite trajectories without requiring the use of penalty functions to approximate the underlying kite dynamics.

The literature for both AWES and MHK kites focuses on characterizing and solving the *forward* kite dynamics, often with the goal of optimizing these dynamics (e.g., by optimizing the kite trajectory). Given a kite's position, velocity, and actuation inputs, the equations governing its forward dynamics furnish its accelerations. Solving the corresponding *inverse* dynamics, in the sense of being able to map a desired combination of kite position, velocity, and acceleration onto the corresponding actuation inputs, is equally important for multiple reasons. First, knowledge of a kite's inverse dynamics enables easy vetting of any prescribed trajectories, i.e., determination of whether the trajectories are feasible. Moreover, if the trajectories are not feasible, the inverse dynamics can provide insights into why they are infeasible. Second, the solution to the inverse kite dynamics problem is not necessarily unique, which means that solving these inverse dynamics

analytically provides insight into the multiplicity of possible solution arcs. Third, an analytic solution to the inverse dynamics problem can be quite valuable for solving trajectory optimization, online estimation, and tracking control problems, both exactly and in a computationally tractable manner. Previous work by the author examined the problem of optimizing energy harvesting kite trajectories using direct transcription methods [33]. In the absence of the analytic inverse dynamics solution approach presented here, such optimization may require the approximate solution of inverse kite dynamics. Such an approximate inverse dynamics solution can be obtained using tools such as the DASSL solver in OpenModelica [34], but adds to the computational complexity of the optimization approach. The approach presented in this chapter improves computational tractability and accuracy by solving the inverse kite dynamics exactly in terms of the roots of a fourth-order polynomial.To the best of the author's knowledge, the problem of obtaining an analytic solution to the inverse kite dynamics problem remains relatively unexplored. The goal of this chapter is to solve this inverse dynamics problem, under reasonable modeling assumptions, for translational kite motion.

3.2   Analytic Solution to the Inverse Dynamics

Given the forward dynamics model in Section 2.2, the desired solution for the inverse dynamics can be obtained as follows. We begin by noting the classical definition of the "inverse dynamics" problem, as the problem of determining the actuation inputs required for achieving a desired motion trajectory. This implies that the motion trajectory, expressed in terms of kite position, velocity, and acceleration versus time, is assumed to be given when solving inverse dynamics problems. The solution of the inverse dynamics therefore requires the joint resolution

31

of the kite's kinematics and kinetics. First, given the kite's position, velocity, the free-stream fluid velocity, and the tether tip orientation, one can compute the unit vectors $\hat{x}_w$, $\hat{y}_w$, and $\hat{z}_w$, as defined in Section 2.2. Second, because the tether tip orientation vector, $\hat{e}_r$, is orthogonal to $\hat{z}_w$ by definition of $\hat{z}_w$, it follows that the component of $\hat{e}_r$ along $\hat{z}_w$ must be zero. With this in mind, one can write $\hat{e}_r$ as follows:

$$\hat{e}_r = \mu \hat{x}_w + \gamma \hat{y}_w \tag{3.1}$$

where the constants μ and γ can be defined as:

$$\mu = \hat{e}_r \cdot \hat{x}_w \tag{3.2}$$

$$\gamma = \|\hat{e}_r - \mu \hat{x}_w\| = \hat{e}_r \cdot \hat{y}_w \tag{3.3}$$

Third, the net force required for achieving the desired kite acceleration, $\vec{F}_{total}$, can be computed by multiplying the kite's mass with its desired acceleration:

$$\vec{F}_{total} = m\dot{\vec{V}} \tag{3.4}$$

Fourth, the required "fluid plus tether force", $\vec{F}$, is defined as follows:

$$\vec{F} = \vec{F}_{total} - \vec{E} = \vec{L} + \vec{T} + \vec{D} \tag{3.5}$$

Fifth, projecting the above force onto the fluid, or wind, coordinate frame gives the forces f_0, f_1, and f_2 below:

$$f_0 = \vec{F} \cdot \hat{x}_w = -\beta(p_1\alpha^2 + p_2\alpha + p_3) - T\mu \tag{3.6}$$

$$f_1 = \vec{F} \cdot \hat{y}_w = \beta(a\alpha + b)cos(\tilde{\phi}) - T\gamma \tag{3.7}$$

$$f_2 = \vec{F} \cdot \hat{z}_w = \beta(a\alpha + b)sin(\tilde{\phi}) \tag{3.8}$$

where the expressions for the tether tension, lift, and drag forces plus the kite lift/drag coefficients have already been substituted into the above equation, and where β is equal to twice the fluid's dynamic pressure times the effective area, A, as shown below:

$$\beta = \rho A \|\vec{V}_{rel}\|^2 \tag{3.9}$$

Next, since both Equation (3.6) and Equation (3.7) are linear in T, it can be eliminated, and the resulting Equation can be squared in order to obtain an expression for $cos^2(\tilde{\phi})$:

$$f_1 - \frac{\gamma}{\mu}f_0 = \beta(a\alpha + b)cos\tilde{\phi} + \frac{\gamma}{\mu}\beta(p_1\alpha^2 + p_2\alpha + p_3) \qquad (3.10)$$

$$(f_1 - \frac{\gamma}{\mu}f_0) - (\frac{\gamma}{\mu}\beta(p_1\alpha^2 + p_2\alpha + p_3)) = \beta(a\alpha + b)cos\tilde{\phi} \qquad (3.11)$$

$$[(f_1 - \frac{\gamma}{\mu}f_0) - (\frac{\gamma}{\mu}\beta(p_1\alpha^2 + p_2\alpha + p_3))]^2 = \beta^2(a\alpha + b)^2 cos^2\tilde{\phi} \qquad (3.12)$$

Next, utilizing the trigonometric identity that the sum of the squares of the sine and cosine of an angle equals unity, and adding Equation (3.12) to the square of Equation (3.8), the following fourth order equation is obtained:

$$[(\frac{\gamma}{\mu}f_0 - f_1) - \frac{\gamma}{\mu}\beta(p_1\alpha^2 + p_2\alpha + p_3)]^2 + f_2^2 = \beta^2(a\alpha + b)^2 \qquad (3.13)$$

Equation (3.13) can finally be solved for α. The resulting values of α can then be substituted in Equation (3.6) to solve for T. Moreover, Equation (3.7) and Equation (3.8) can be used to solve for $\cos(\tilde{\phi})$ and $\sin(\tilde{\phi})$, respectively, which makes it possible to uniquely determine $\tilde{\phi}$.

The above procedure makes it possible to solve the kite's inverse dynamics analytically in terms of the roots of a fourth-order polynomial in α. The existence of four potential solutions for the kite's inverse dynamics is an interesting outcome of this work. This multiplicity of solutions can be explained as follows. First, the ratio of $\frac{L}{D}$ represents a particular force direction, and because the lift and drag coefficients are affine and quadratic functions of α, respectively, a particular ratio of $\frac{L}{D}$ can be achieved using either a relatively high or relatively low combination of values of lift, drag, and α. Second, each solution for α has a symmetric counterpart where the

34

kite flies "upside down", rolling by 180 degrees and simultaneously switching to a new value of α that recovers the original lift and drag forces. Therefore, there are two causes of multiplicity of inverse dynamics solutions (high/low angle of attack multiplicity and symmetry), with each cause creating a multiplicity of 2, and with both causes combined therefore creating a multiplicity of 4.

Once the solution to the above inverse dynamics is obtained, one can easily compute other quantities, including the orientation of the kite's body coordinate frame. To show this, we first note that when the angle of attack is zero, the three coordinate axes of the kite's body frame will be parallel to the relative wind velocity direction, $\hat{x}_w$, the lift force direction, $\cos(\tilde{\phi})\hat{y}_w + \sin(\tilde{\phi})\hat{z}_w$, and the cross product of these two directions, $-\sin(\tilde{\phi})\hat{y}_w + \cos(\tilde{\phi})\hat{z}_w$, respectively. Given an angle of attack α plus the fact that our earlier assumption of "weathercocking" translates to a sideslip angle of zero, the three coordinate vectors describing the kite's body frame must therefore equal:

1. A vector $\hat{x}_w \cos(\alpha) + \sin(\alpha)[\cos(\tilde{\phi})\hat{y}_w + \sin(\tilde{\phi})\hat{z}_w]$, pointing in the aft-forward direction.

2. A vector $-\hat{x}_w \sin(\alpha) + \cos(\alpha)[\cos(\tilde{\phi})\hat{y}_w + \sin(\tilde{\phi})\hat{z}_w]$, pointing upwards from the kite's body.

3. A third vector, $-\sin(\tilde{\phi})\hat{y}_w + \cos(\tilde{\phi})\hat{z}_w$, pointing in the port-starboard direction.

Together, the above three directions define the kite's body coordinate frame, and make it possible to compute additional variables such as the kite's Euler angles using standard formulas from the literature [53].

3.2.1   Geometric Force Balance

To see the above sources of multiplicity more clearly, consider the free-body diagram of the kite in the body coordinate frame (Figure 3.1). Moreover, let L and D represent the scalar

values of the lift and drag forces, respectively. This leads to the following definitions:

$$L = \beta(a\alpha + b), \quad D = \beta(p_1\alpha^2 + p_2\alpha + p_3) \tag{3.14}$$

In the above definitions, the scalar lift force, L, can be either positive or negative depending on the value of α. The scalar value of the drag force, D, is a positive quantity, but it acts along the $-\hat{x}_w$ direction vector. The tether force T acts along the unit vector $-\hat{e}_r$, which has projections μ and γ onto the x_w and y_w axes, respectively. The lift force L acts in the $y_w z_w$ plane. Its $\hat{z}_w$ component is f_2 in Equation (3.8), and the remaining component is $L cos(\tilde{\phi})$ along $\hat{y}_w$ as in Equation (2.9). Once we consider the added forces f_1 and f_2, we can study the force balances.

$$-D - f_0 = T\mu \tag{3.15}$$

$$L cos(\tilde{\phi}) - f_1 = T\gamma \tag{3.16}$$

$$f_2 = L sin(\tilde{\phi}) \tag{3.17}$$

The tension force T must balance the other forces on the kite. So the projection of the tension onto the x axis $T\mu$ must match $-D - f_0$, as shown in Equation (3.15), which matches Equation (3.6). Similarly, the tension projected onto the y_w axis $T\gamma$ must match the $L cos(\tilde{\phi})$ component of lift minus f_1 as shown in Equation (3.16), which is Equation (3.7). Finally, the z_w component of lift must match f_2 Equation (3.17) which matches Equation (3.8).

Given the above definitions, one can rewrite Equation (3.8) and Equation (3.10) as follows:

$$f_2 = Lsin(\tilde{\phi}) \tag{3.18}$$

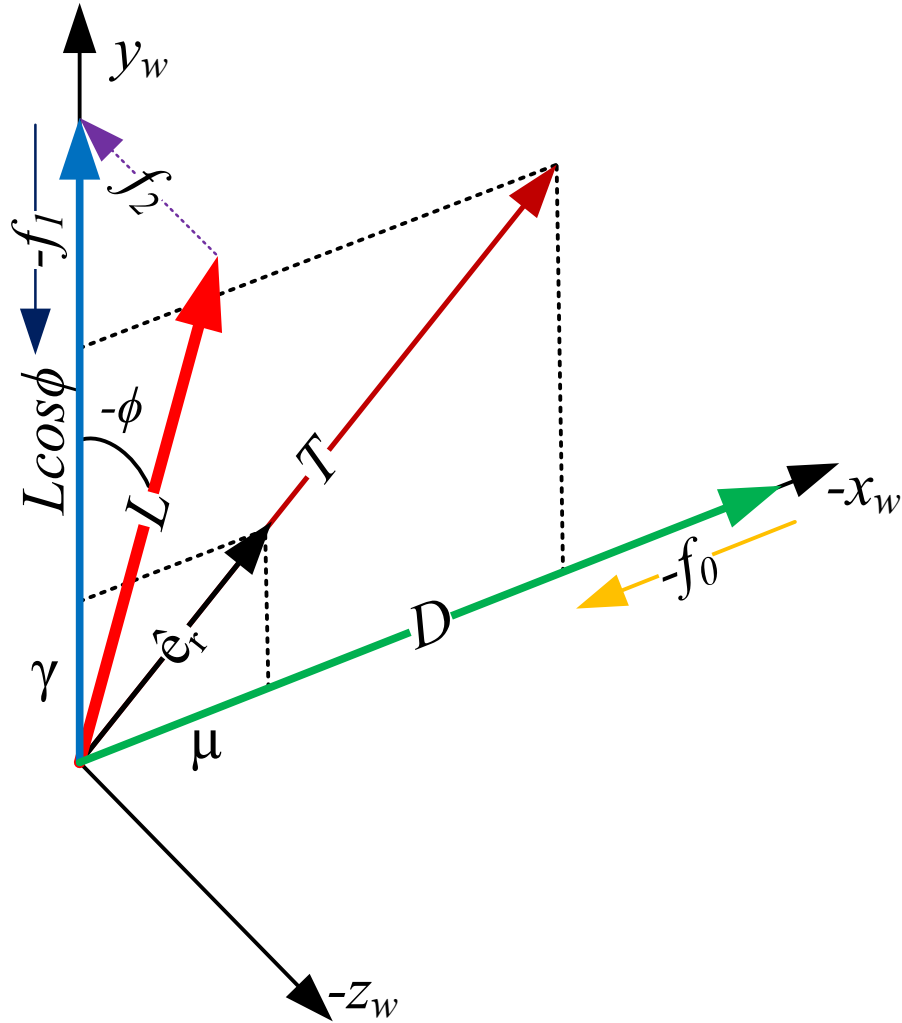$$f_1 - \frac{\gamma}{\mu}f_0 = Lcos\tilde{\phi} + \frac{\gamma}{\mu}D \tag{3.19}$$

Figure 3.1: Body forces diagram.

Based on the above two equations, one can construct a right-angle "lift force triangle", where the sides of the triangle represent L, $Lsin(\tilde{\phi})$, and $Lcos(\tilde{\phi})$, as shown in Figure 3.2.

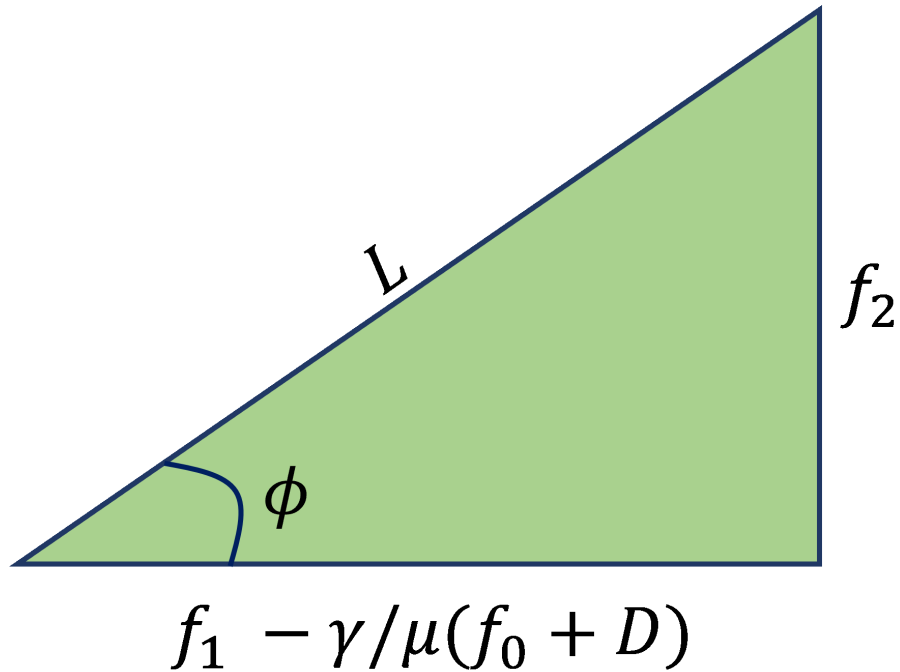In the lift force triangle (Figure 3.2), the length of the opposite edge, f_2, is not a func-

Figure 3.2: Lift force triangle

tion of α. However, the lengths of the adjacent edge and hypotenuse are both depend on α.

Equation (3.13) essentially states Pythagoras' theorem for this triangle. Because of the quadratic dependence of D on α, two fundamentally distinct groups of solutions can arise for angle of attack, as discussed above: a low-α solution pair and a high-α solution pair. The remainder of this chapter examines three special cases of the above lift force triangle that help shed more light on the multiplicity of solutions for α.

3.2.2 Special Case #1: Zero Force Requirements

Consider the scenario where the net hydrodynamic plus tether force needed for kite motion is zero, i.e., $f_0 = f_1 = f_2 = 0$. In this case, assuming $\tilde{\phi} = 0$ (and noting that $\tilde{\phi} = 180$ degrees is also a plausible scenario), the lift force triangle collapses to a straight line segment, where the lengths of the hypotenuse and adjacent edge must be equal, i.e.,

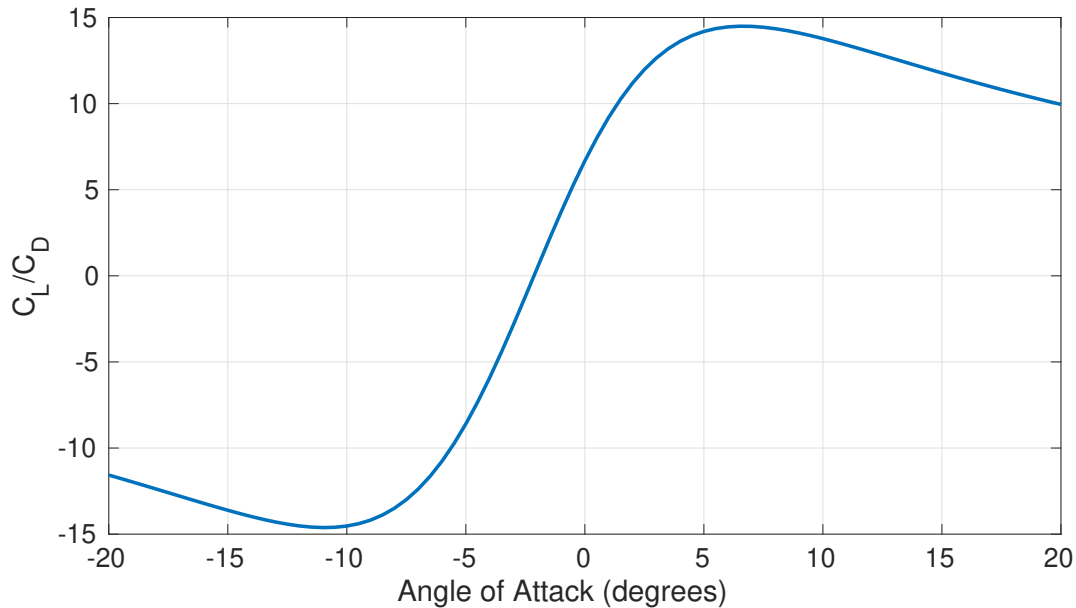$$L = -\frac{\gamma}{\mu}D \tag{3.20}$$

Figure 3.3: Impact of angle of attack on lift-to-drag ratio

The above equation can be interpreted as projecting the lift and drag forces onto an axis normal to the tether, and requiring the net force along this axis to be zero. Moreover, this equation can be interpreted as requiring a specific value for the lift-to-drag ratio. Figure 3.3 plots the kite's lift-to-drag ratio versus angle of attack. A unique value of α corresponds to the peak (positive or negative) lift-to-drag ratio. For all lift-to-drag ratios smaller in magnitude than this peak, it is mathematically possible to find two values of α satisfying Equation (3.20). Moreover, for each of these pairs of L and D, a symmetric counterpart exists where the kite flies "upside down" by switching between $\tilde{\phi} = 0$ and $\tilde{\phi} = 180$ degrees. This explains the potential for four solutions for α.

3.2.3   Special Case #2

Consider the special case where the required force f_2 equals zero, but f_0 and f_1 can be nonzero. We assume $f_2 = 0$ implies $\tilde{\phi} = 0$ via Equation (3.17). Note that $\tilde{\phi} = \pm 180$ degrees is also a plausible scenario, but would change the sign of lift. In this case, the lift force triangle collapses to a straight line where the hypotenuse and adjacent lengths must be equal, i.e.,

$$L = f_1 - \frac{\gamma}{\mu}(f_0 + D) \Rightarrow \mu(L - f_1) = -\gamma(D + f_o) \tag{3.21}$$

Equation (3.21) has an interesting geometric interpretation. The terms $L - f_1$ and $D + f_0$ represent the components of the lift and drag forces that remain once the required values of f_1 and f_0 have been achieved, respectively. Once again, these components must add up to a force that aligns with the kite's tether, similar to special case # 1. Once again, this leads to a quadratic Equation in terms of angle of attack, α, with up to two potentially distinct solutions. Moreover, symmetric inverted counterparts exist to these solutions, corresponding to $|\tilde{\phi}| \geq 90$ degrees.

We can directly solve for α via the quadratic formula by substituting for L and D with Equation (3.14) into Equation (3.21). This yields a quadratic in α which can potentially furnish as many as two real solutions,

$$\mu\left(\beta(\alpha a + b) - f_1\right) = -\gamma\left(\beta(\alpha^2 p_1 + \alpha p_2 + p_3) + f_0\right) \tag{3.22}$$

$$\frac{\mu}{\gamma}(\alpha a + b) + \frac{1}{\beta}(f_0 - \frac{\mu}{\gamma}f_1) = -(\alpha^2 p_1 + \alpha p_2 + p_3) \tag{3.23}$$

$$\alpha^2 p_1 + \alpha(p_2 + \frac{\mu}{\gamma}a) + \left(p_3 + \frac{\mu}{\gamma}b + \frac{1}{\beta}f_0 - \frac{\mu}{\gamma}f_1\right) = 0 \tag{3.24}$$

3.2.4 Special Case #3

Finally, consider the special case of a non-cambered kite wind. In such a case, one can reasonably assume that zero lift is achieved at a zero angle of attack, meaning that $b = 0$ in Equation (3.13) [54]. Moreover, one can reasonably assume that drag is minimum at zero lift, meaning that $p_2 = 0$ in the above equation [54]. The fourth-order Equation for α then simplifies to:

$$[(\frac{\gamma}{\mu}f_0 - f_1) - \frac{\gamma}{\mu}\beta(p_1\alpha^2 + p_3)]^2 + f_2^2 = \beta^2(a\alpha)^2 \tag{3.25}$$

This is a quadratic Equation in terms of α^2, meaning that for every value of α, there is indeed a symmetric counterpart solution where the sign of the angle of attack is flipped. Moreover, at least for some kite maneuvers, there will exist a solution with a higher angle of attack and a solution with a lower angle of attack, which explains the multiplicity of solutions for α.

3.3 Simulation Example

This section presents a simulation example highlighting the proposed inverse dynamics approach. The example builds on lessons learned in previous work by the authors, focusing on energy harvesting using tethered MHK kites [33]. One lesson from this previous work is that MHK kites can harvest significant amounts of energy by flying cross-current in circular patterns while reeling in and out at low and high tension levels, respectively. This represents an alternative to the more common approach in the literature, where cross-current flight trajectories often have

figure-8 shapes.

The specific trajectory examined in this section has a spatially uniform and temporally constant water flow speed of 1 m/s along the positive x-direction of the base frame. The kite flies in perfect circular cross-current patterns in the base frame's yz-plane, while reeling in and out periodically along the base frame's x-axis. The trajectory has a 125-second time period, and is described by the equations below:

$$\omega = \frac{2\pi}{125} \tag{3.26}$$

$$x = 100 + 10\sin\omega t \tag{3.27}$$

$$y = 25\sin\left(5\omega t\right) \tag{3.28}$$

$$z = 25\cos\left(5\omega t\right) \tag{3.29}$$

The above equations translate into the 3-dimensional trajectory shape shown in Figure 3.4.
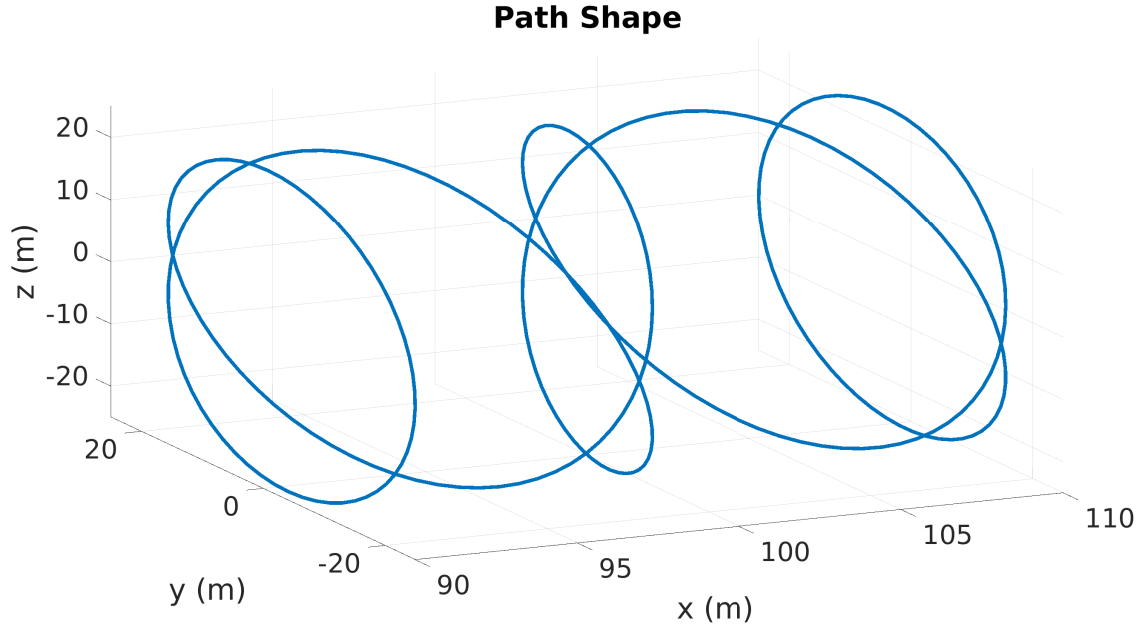
Figure 3.4: Prescribed Path Shape

Following the procedure outlined earlier in this chapter, four inverse dynamics solutions were obtained for the above trajectory. Each solution is characterized by a different set of trajectories for angle of attack, α, induced roll angle, $\tilde{\phi}$, and tether tension, T. Figure 3.5 shows the four solution trajectories for the angle of attack, α. These trajectories are all mathematically plausible. Moreover, all of these solution arcs satisfy the required values for the forces f_0, f_1, and f_2 at every instant in time, as shown in Figure 3.6. The errors between the required and solved f_0, f_1, and f_2 are very close to 0 (within numerical noise), given that the inverse dynamics is being solved exactly. Interestingly, the solution trajectories in Figure 3.5 are symmetric around $\alpha = -b/a$, the angle of attack corresponding to zero lift. However, not all of these trajectories are physically reasonable. For instance, the large-α solutions are likely to result in kite stall. Moreover, the solutions corresponding to negative values of α represent an "upside down" kite flight configuration. With this in mind, the remainder of this section focuses on the smallest positive

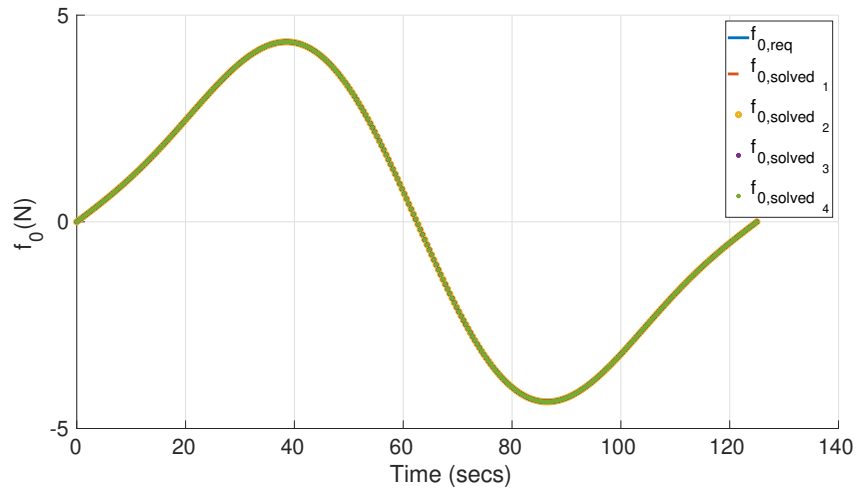solution trajectory for α, shown in Figure 3.5b.
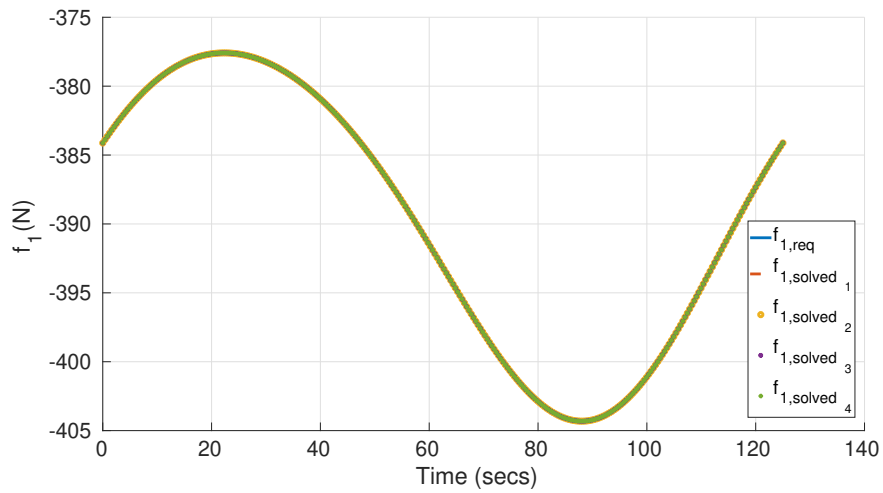

(a) All possible solutions for α
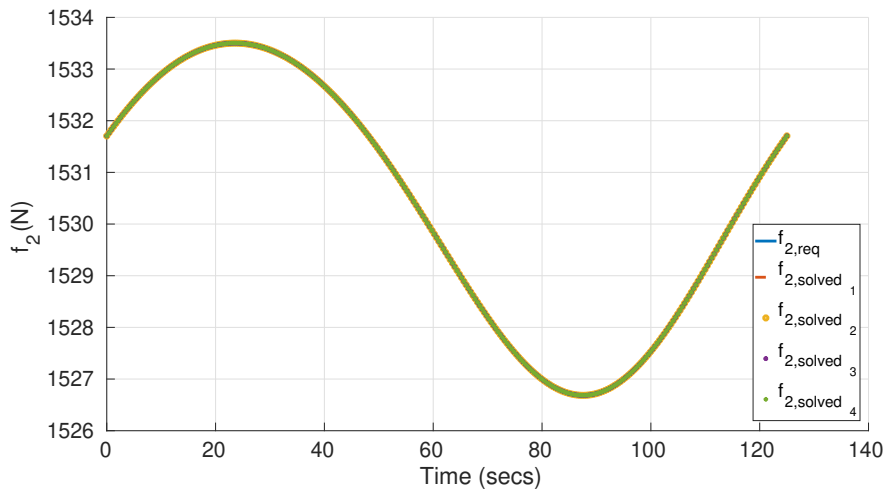

(b) Final solution chosen for α

Figure 3.5: Angle of Attack Solutions (degree)
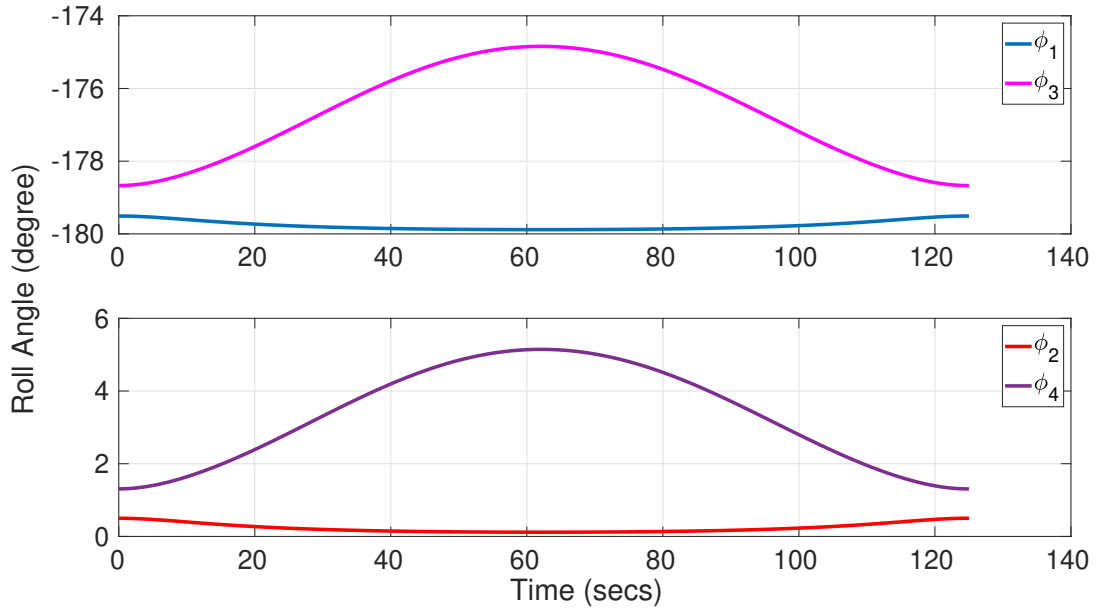
(a) Required and solved solution arcs of $f_0(\mathrm{N})$

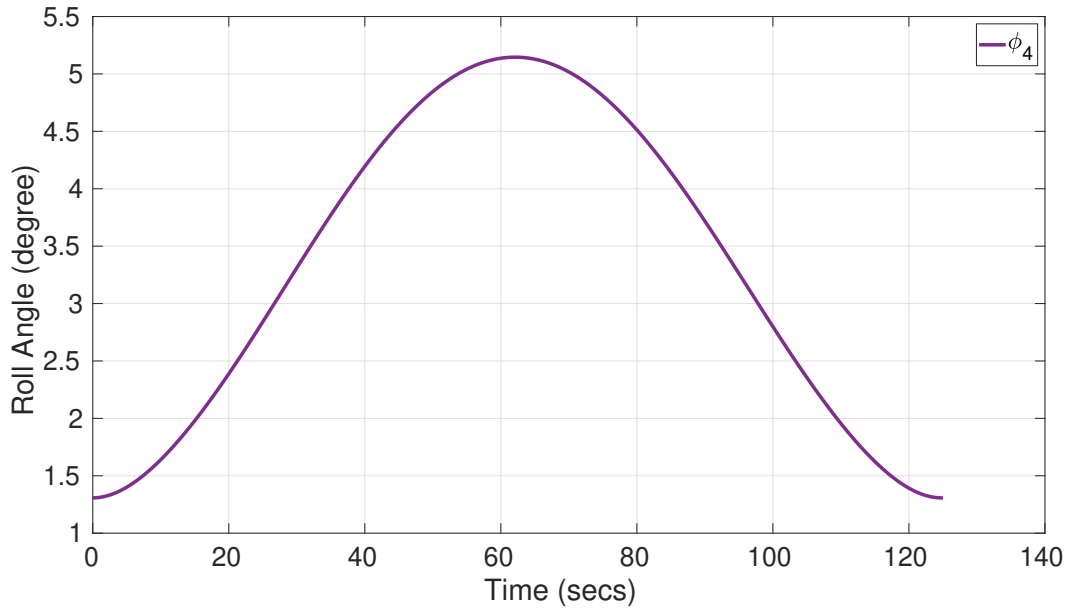(b) Required and solved solution arcs of $f_1(\mathrm{N})$

(c) Required and solved solution arcs of $f_2(\mathrm{N})$

Figure 3.6: Desired trajectories of the forces (a) $f_0(\mathrm{N})$, (b) $f_1(\mathrm{N})$, and (c) $f_2(\mathrm{N})$

45

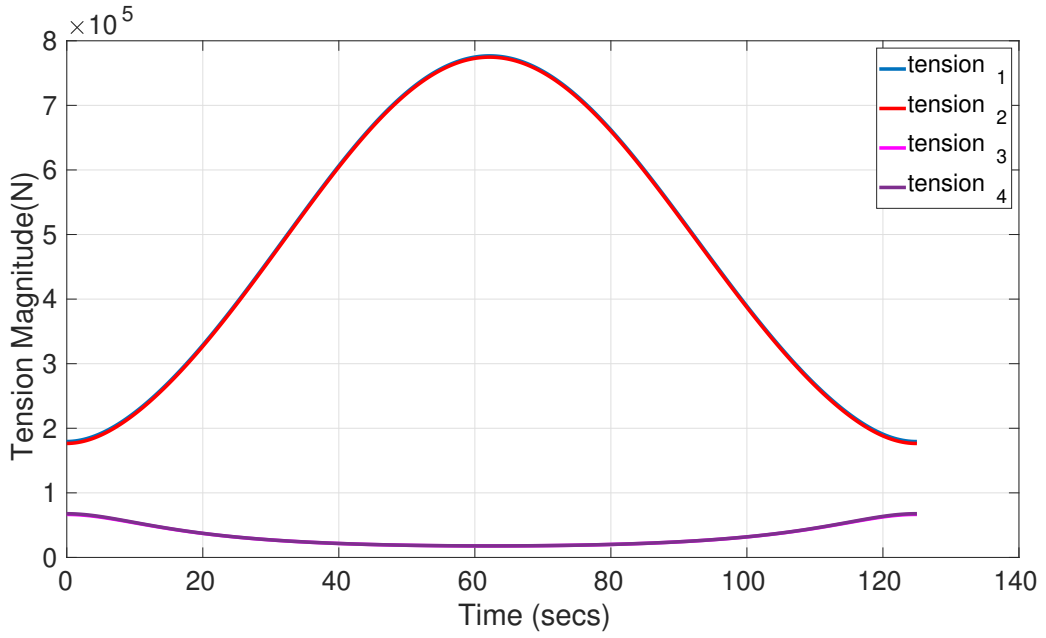(a) All possible solutions for $\tilde{\phi}$

(b) Final solution chosen for $\tilde{\phi}$

Figure 3.7: Roll Angle Solutions (degree)

Figure 3.7a shows the four solutions for roll angle, $\tilde{\phi}$ corresponding to the four solutions for α. Both angles are plotted in degrees. Two of the solutions correspond to an upside-down kite configuration, but the solution associated with the selected trajectory for α is associated

46

with small positive roll angles, as shown in Figure 3.7b. Interestingly, only a small roll angle magnitude is required versus time, reflecting the degree to which fast cross-current flight enables the achievement of significant flight path curvatures with only a small need for banking, or roll.

Figure 3.8 shows the four solution histories for tether tension versus time, corresponding to the four solutions for α. The inverse dynamics solution approach presented in this paper does not preclude negative tension solutions. However, such solutions would automatically imply trajectory infeasibility for tethered kite systems. All four solution arcs correspond to positive tension histories, implying that all four arcs are feasible in this case, at least from a tethered system's perspective. The solution arc corresponding to the selected history of α is shown in Figure 3.8b. Interestingly, this solution achieves high values of tension towards the beginning and end of the time period, when the kite is being reeled out in the x-direction. This is desirable from an energy harvesting perspective, and it also points to the following important insight. Optimizing the translational trajectory of the kite, as represented by $x(t)$, $y(t)$, and $z(t)$, may not be sufficient for optimal energy harvesting. One should also optimize the choice of control input solution arc that generates maximum power for this given trajectory.

(a) All possible solutions for T
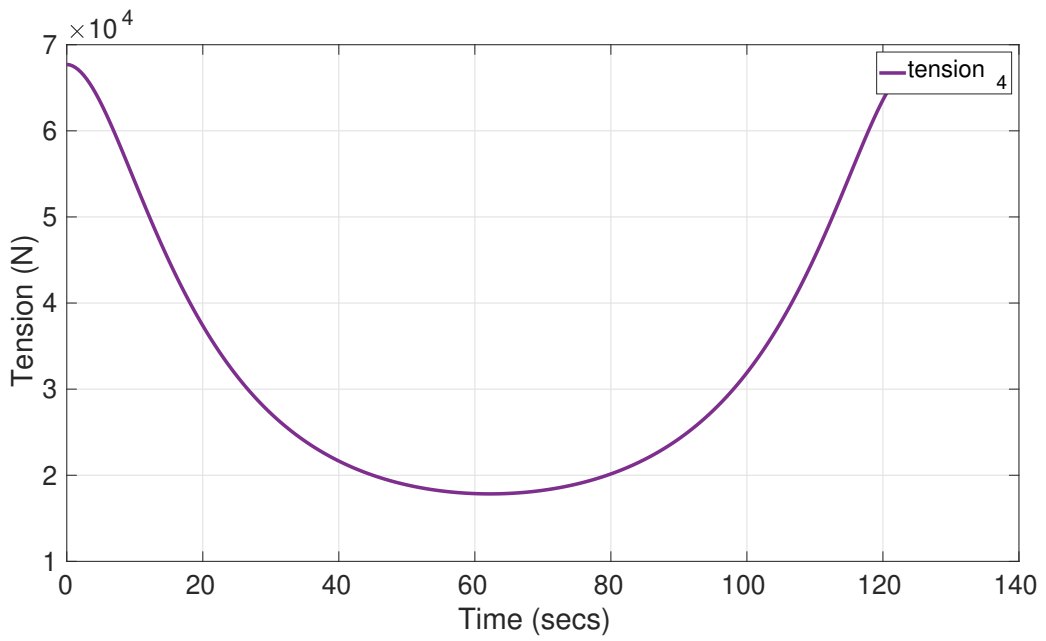
(b) Final solution chosen for T

Figure 3.8: Tension Magnitude Solutions (N)

3.4 Conclusion

While the modeling, control, and optimization of tethered kites have been explored in great detail, this chapter presents the first analytic solution of the inverse dynamics of the underlying kites. This analytic solution is useful for gaining fundamental insights and facilitating tractability in trajectory optimization, tracking, estimation, and control. The next chapter in this dissertation includes the use of the inverse dynamics solution for precise trajectory optimization and kite control. Finally, the framework presented in this chapter can potentially be extended to account for important effects such as tether curvature, provided models of those effects are available.

Chapter 4: Co-optimization of the Spooling Motion and Cross-Current Trajectories using Inverse Dynamics Analysis

4.1 Overview

This chapter addresses the challenge of simultaneously optimizing the spooling motion and cross-current trajectory of MHK kite using the inverse dynamics solution obtained in Chapter 3. This optimization is performed using a Fourier expansion of the kite's state trajectories over time that transforms the trajectory optimization problem into a non-linear program [55], [56]. The work in this chapter has been submitted for review to a peer-reviewed journal [36].

4.2 Optimization Approach

The model used in the optimization remained the same as in Chapter 2. However, the optimization statement now is:

$$\min J = \frac{1}{t_f - t_i} \int_{t_i}^{t_f} (-w_p P_{mech} + J_{rate} + J_\alpha + J_T + J_\phi) dt \tag{4.1}$$

subject to the kite dynamics plus the constraints:

$$\vec{X}_{t_i} = \vec{X}_{t_f} \tag{4.2}$$

$$P_{mech} = \vec{T}^T \vec{V} \tag{4.3}$$

The value of the Pareto weight, w_p, and the definitions of J_{rate}, J_α, J_T, and J_ϕ are as follows:

$$w_p = 2500 \tag{4.4}$$

$$J_{rate} = 10^4 (\dot{\alpha}^2 + \dot{T}^2 + \dot{\phi}^2) \tag{4.5}$$

$$J_\alpha = \begin{pmatrix} 10^{10}(20 - \alpha) & \text{if} & \alpha > 20° \\ \\ 10^{10}(\alpha + 5) & \text{if} & \alpha < -5° \end{pmatrix} \tag{4.6}$$

$$J_T = \begin{pmatrix} 10^{10}(10^5 - T) & \text{if} & T > 10^5 \text{N} \\ \\ 10^{10}(T) & \text{if} & T < 0\text{N} \end{pmatrix} \tag{4.7}$$

$$J_\phi = \begin{pmatrix} 10^{20}(|\phi| - \frac{1}{2}\pi) & \text{if} & |\phi| > \frac{1}{2}\pi \text{rad} \\ \\ 0 & & \end{pmatrix} \tag{4.8}$$

The above optimization statement has two objectives:

1. To maximize average mechanical power produced over one time period, defined as the time taken for the kite to spool in and out once. Here t_i is the initial time, and t_f is the final time.

2. To maintain a smooth motion trajectory by penalizing the time rate of change of the three control inputs.

3. To ensure that the control inputs do not surpass reasonable minimum and maximum bounds.

Since this is a periodic optimal control problem, Equation (4.2) ensures periodicity of the states, with $\vec{X}_t$ being the state at any time instant. The state variables of this kite model are the position and velocity of the kite in the base frame. They are approximated as truncated Fourier series because of periodicity.

$$\vec{X} = \frac{\vec{a}(0)}{2} + \sum_{n=1}^{3}\left[\vec{a}(n)\cos\frac{2\pi n}{T_{period}} + \vec{b}(n)\sin\frac{2\pi n}{T_{period}}\right] \qquad (4.9)$$

Similar to Chapter 2, the vectors $\vec{a}(n)$ and $\vec{b}(n)$ are expansion coefficients corresponding to the nth harmonic of the Fourier expansion. In this work, n is chosen to be 3 for simplicity. The period of the Fourier series is $T_{period} = t_f - t_i$. Expressing the state as a Fourier expansion allows for the optimization of the initial kite position and velocity, as part of trajectory optimization. Thus, the coefficient vectors $\vec{a}(n)$, $\vec{b}(n)$, and the time period T_{period} become the optimization variables. These optimization variables must satisfy the state dynamics. In the author's previous work, this was solved by representing both the states and the control inputs as Fourier series, and then imposing a penalty on the discrepancy between the kite forces produced by the assumed control input trajectories versus the forces required for achieving the desired state trajectories. In contrast, this chapter uses an analytic solution of the inverse dynamics, allowing one to solve the trajectory optimization exactly. Since the kite's dynamics are non-linear, the trajectory optimization problem is therefore non-convex. Similar to [33] and Chapter 2, a particle swarm algorithm is used for the initial exploration of the optimization space, followed by the use of the Nelder-Meade simplex algorithm for the local refinement of the particle swarm solution. Figure 4.1 shows the high level representation of the optimization approach.
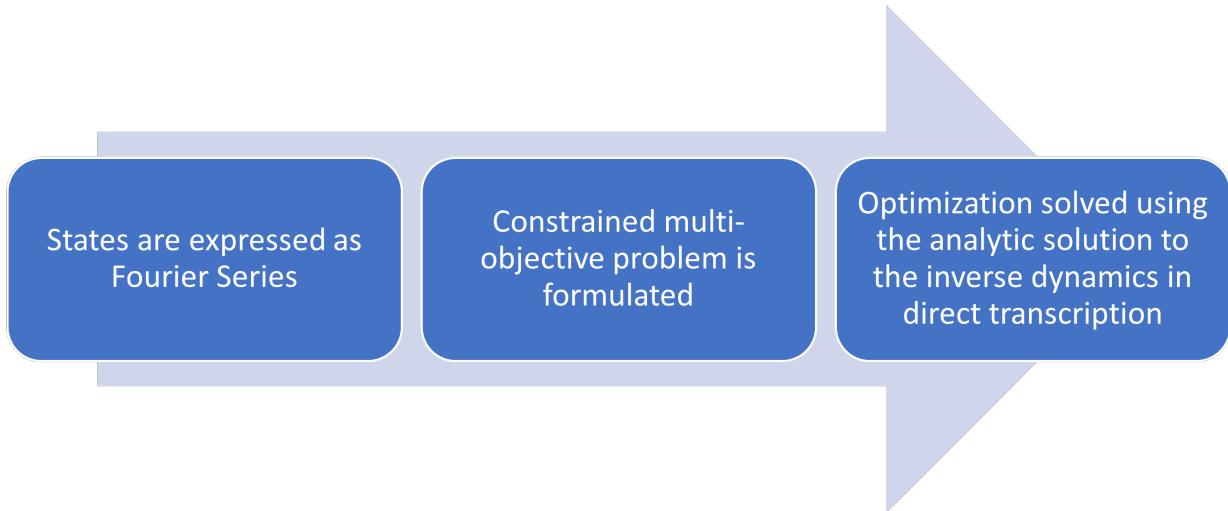
Figure 4.1: Power Maximization Algorithm

.

The numerical solution of the above optimization problem depends on the number of harmonics used in the underlying Fourier series expansion. Using higher harmonics leads to only a small increase in the power production. For example, as seen in Figure 4.2, while the Pareto cost decreases by 25.69% from $n = 4$ to $n = 5$, the power production only increases by 1.65%. From $n = 3$ to $n = 4$, the Pareto Cost decreases by 2.65% and power production increases by 6.31%. Increasing the number of Fourier coefficients also increases the computation time, and therefore, in the remainder of this chapter, $n = 3$ was chosen. In the above comparison between different orders of the Fourier expansion, the initial condition for each previous value of n was used to run the Nelder-Meade simplex algorithm to get the values of power and Pareto cost.
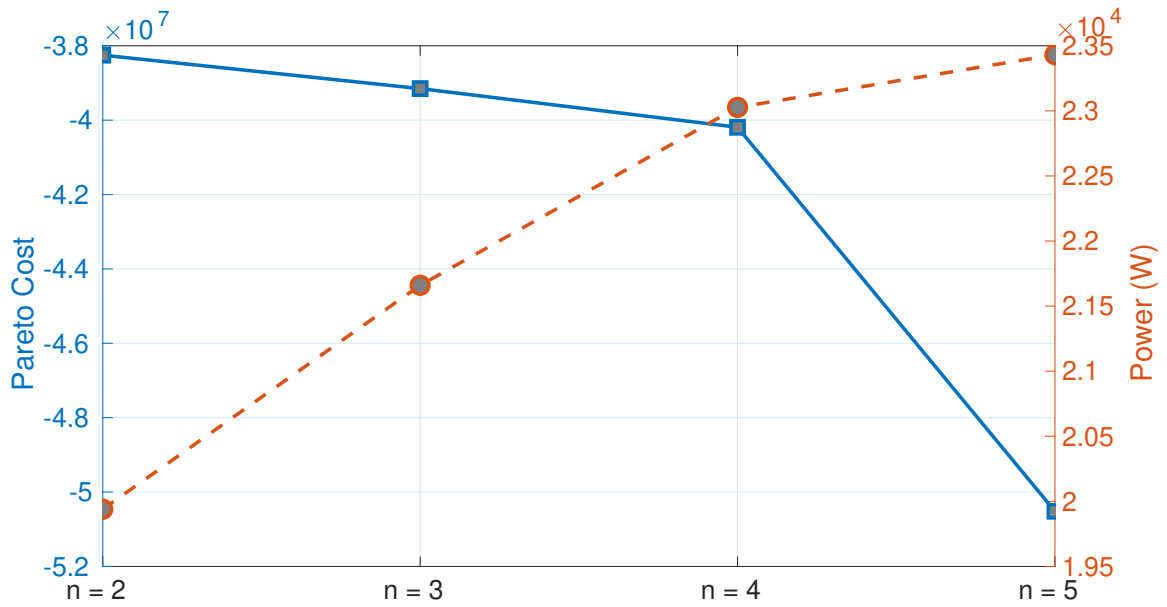
53

Figure 4.2: Comparison of Pareto Cost and Power with Different Number of Fourier Coefficients

The results of this chapter's numerical optimization also depend on the chosen value of the Pareto scalarization weight. An analysis of different Pareto weights shows that the increase in power and reduction in Pareto cost is minimal with higher Pareto weight. Therefore, $w_p = 2500$ is a reasonable choice for the subsequent simulation study.
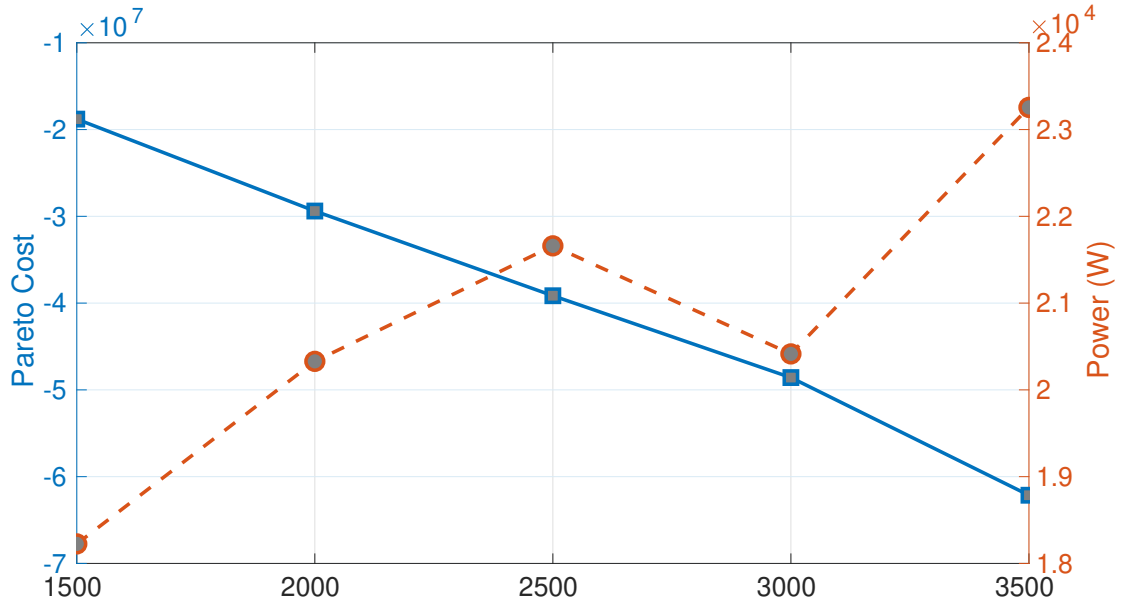
Figure 4.3: Comparison of Pareto Cost and Power with Different Pareto Weights

4.3 Results

This section presents simulation results showing that the optimization algorithm that incorporates the inverse dynamics solution and the 3-DOF kite model, successfully furnishes a trajectory with desirable power production. A kite of similar area would theoretically produce a maximum of 83.9kW of power during steady state reel-out [4]. The optimization algorithm was able to produce an average power of 21.3kW within one time period, consistent with the authors' previous work that approximated the kite's dynamics during optimization instead of solving them exactly [33]. This is important because it provides more confidence in the feasibility of achieving such a level of average power. Figure 4.4 further shows that the kite consumed very little power during reel-in, never exceeding 3kW. Moreover, during reel-out, the kite was able to produce instantaneous power much higher than the steady state theoretical limit, reaching almost 60kW. Therefore, the kite was able to achieve a Loyd factor, defined as the ratio of the generated power
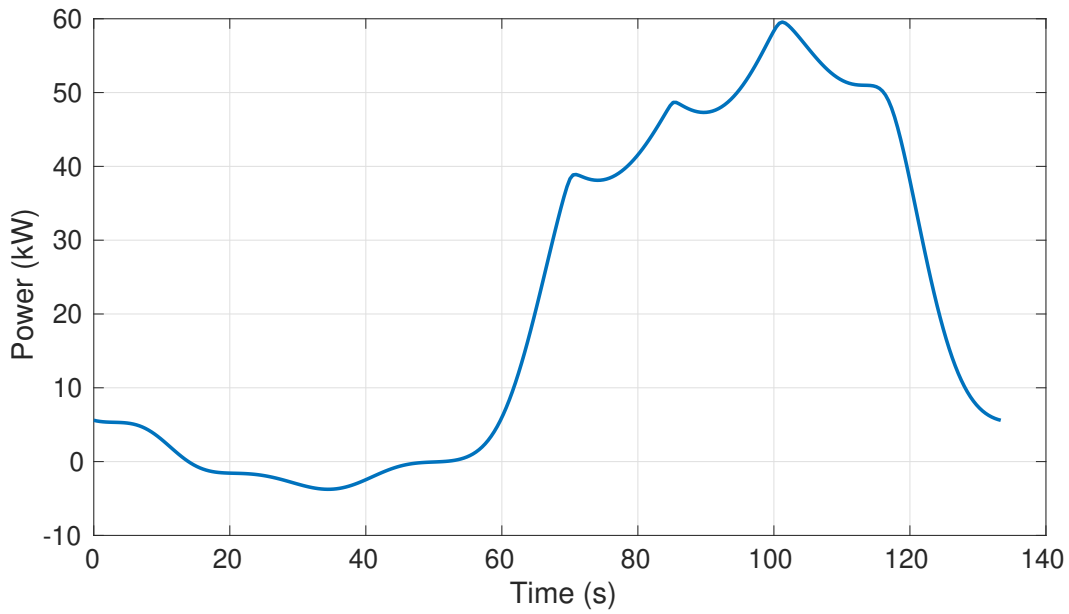
55

to the theoretical power, of 25.38%.

Figure 4.4: Power Produced by the Kite

The kite followed a simple trajectory of a short reel-out and reel-in episode, before being reeled-out for a longer period of time, as shown in Figure 4.5. It is assumed that the kite's anchor point is sufficiently underwater such that the kite does not rise above the surface as it traverses this trajectory.
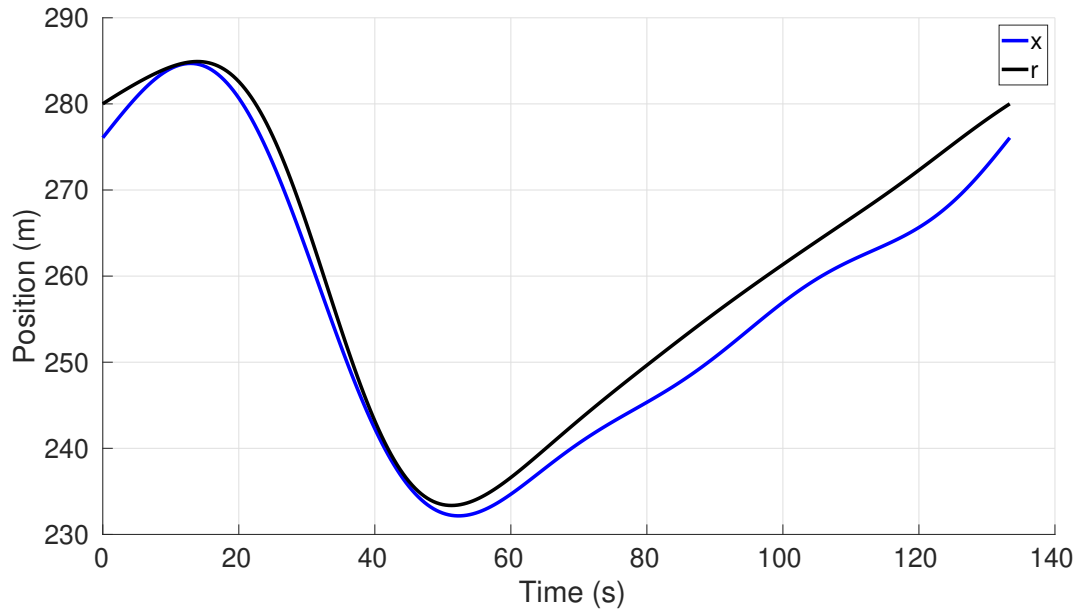
(a)
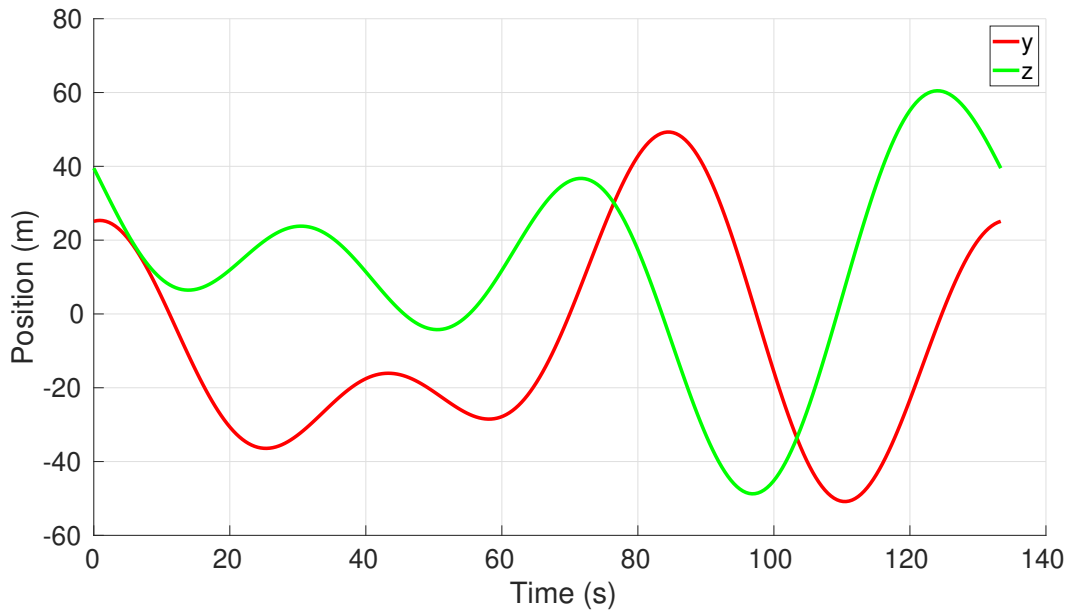
(b)

Figure 4.5: Position of the Kite

The full trajectory, as seen in Figure 4.6, is similar to results obtained in [33] in that the

optimal path shape is once again not figure-8, and can be approximated as a sequence of circles

in the yz-plane. The non-figure-8 path shape eliminates the need for switching the direction of

induced roll, which is attractive from the perspective of minimizing the rates of change of various actuation inputs. Moreover, this shape is acceptable due to the fact the kite is neutrally buoyant, and therefore does not need to exploit the potential safety benefits of a figure-8 trajectory where the kite turns upwards (as opposed to downwards) when it turns. As seen again, the radius of curvature is still pretty tight and that can attributed to the same reasons as mentioned in Chapter 2: (i) the variation in relative velocity across the wing span and (ii) potentially unrealistic yaw rate.
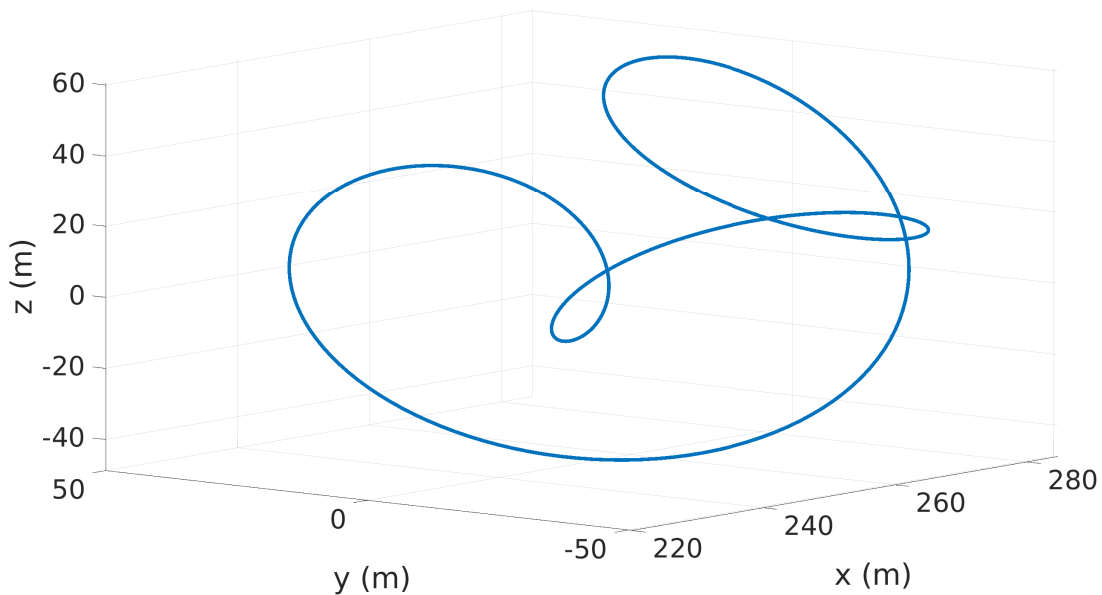

Figure 4.6: Optimized Path Shape

As shown in Figure 4.7, the velocity of the kite in the yz-plane is larger than in the x-direction, thereby showing that the kite is exploiting cross-current motion substantially. The speed with which the kite reels in and out, $\dot{r}$, does not always equal the speed of the kite parallel to the free-stream velocity, $\dot{x}$. This implies that the kite achieves a non-trivial portion of its reel-in/out motion by traveling either towards or away from the origin in the yz-plane. Such in-plane reel-in/out motion is intuitively attractive because it minimizes the total distance required for kite operation parallel to the free-stream fluid velocity. According to [4], the optimal velocity for the

58

kite to produce maximum power should be $\frac{1}{3}$ of the free stream velocity, which in this case is $\frac{1}{3}$ m s^{-1}. The kite's transient reel-out speeds are slightly higher, enabling higher levels of power generation during transient reel-out.
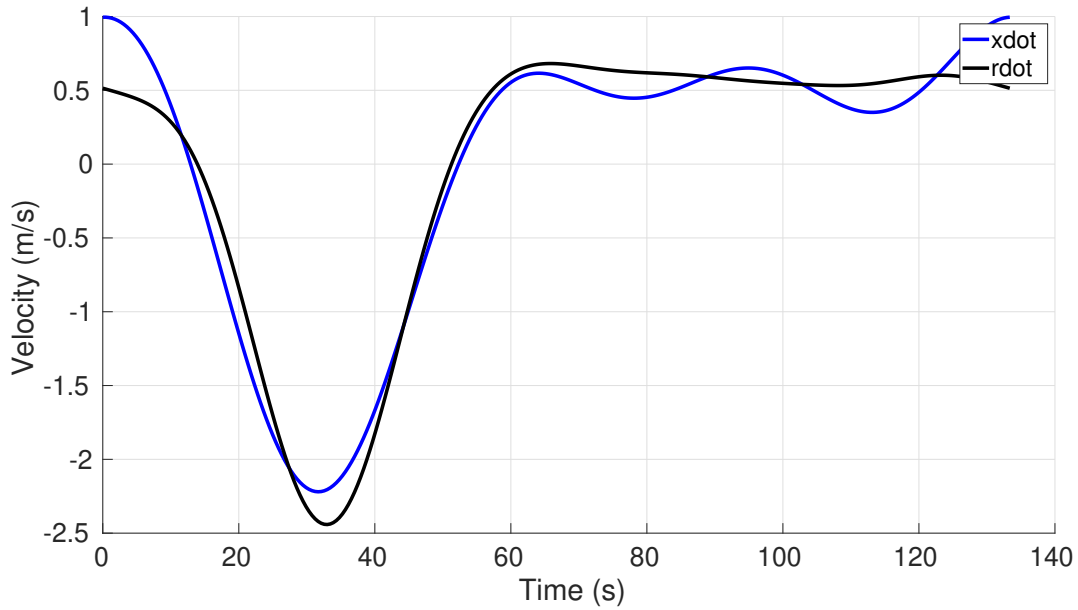

(a)
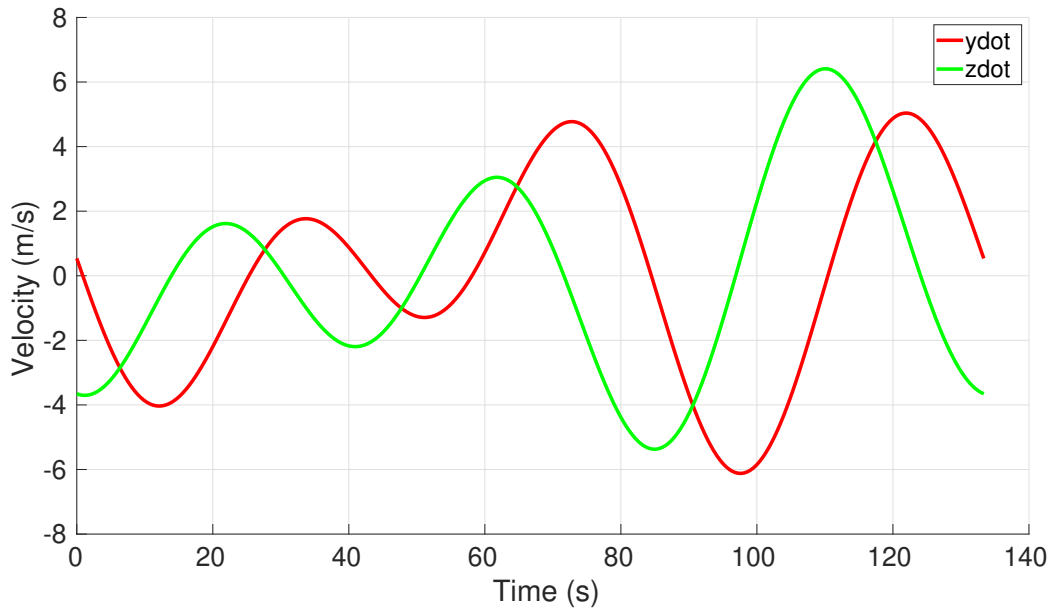
(b)

Figure 4.7: Velocity of the Kite

During spool-out, the angle of attack reaches a relatively high value, ensuring a high lift-to-drag ratio, as shown in Figure 4.8a and Figure 4.8b. This also ensures that the during spool-out, the tension is at a maximum, as seen in Figure 4.9. During spool-in, the angle of attack becomes negative, and the tether tension at the corresponding time reaches its minimum value.
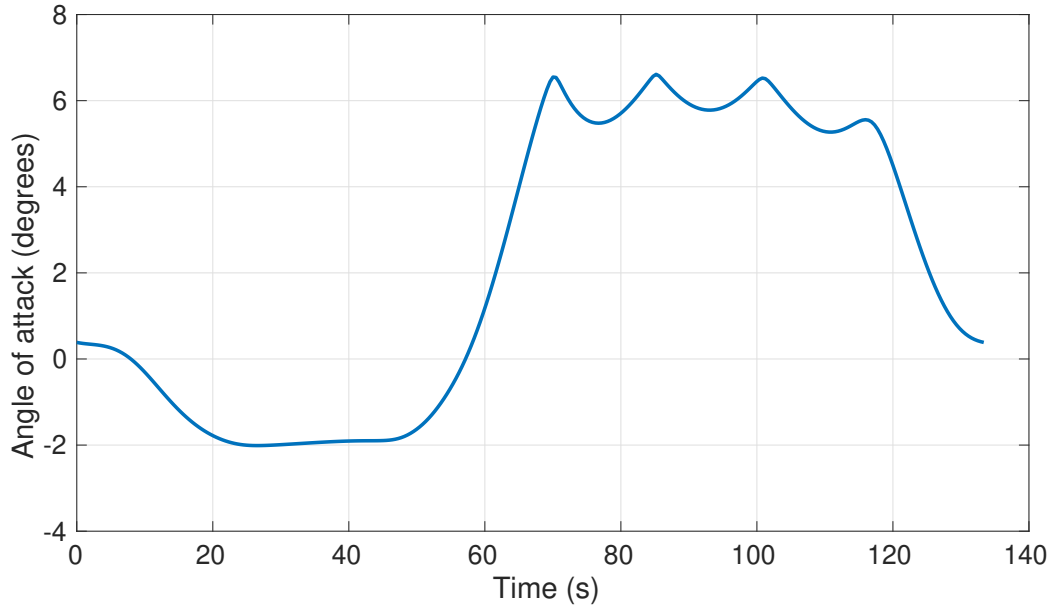
(a) Angle of Attack
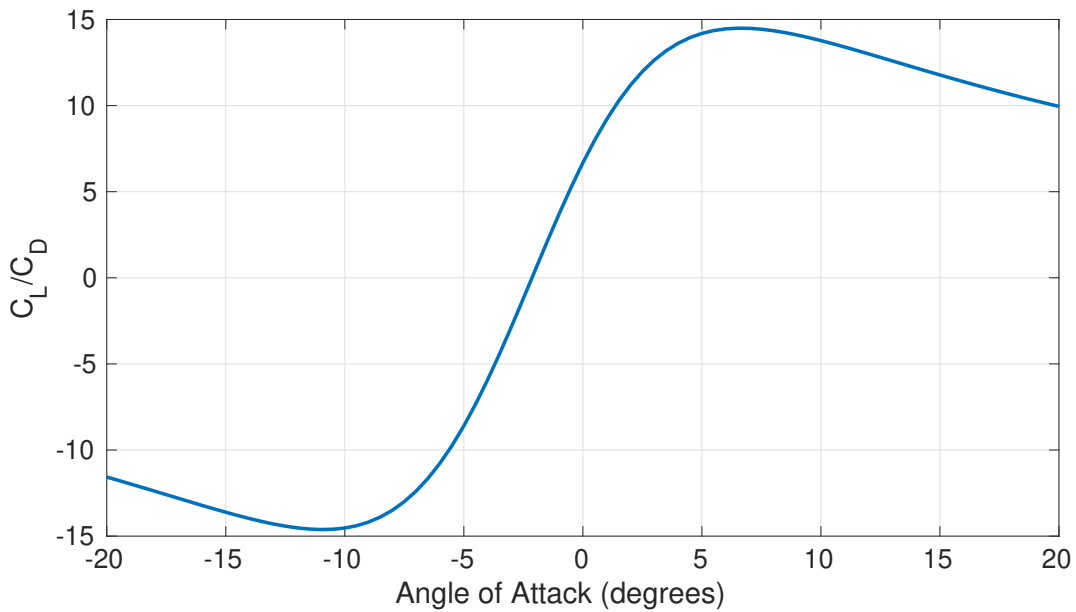
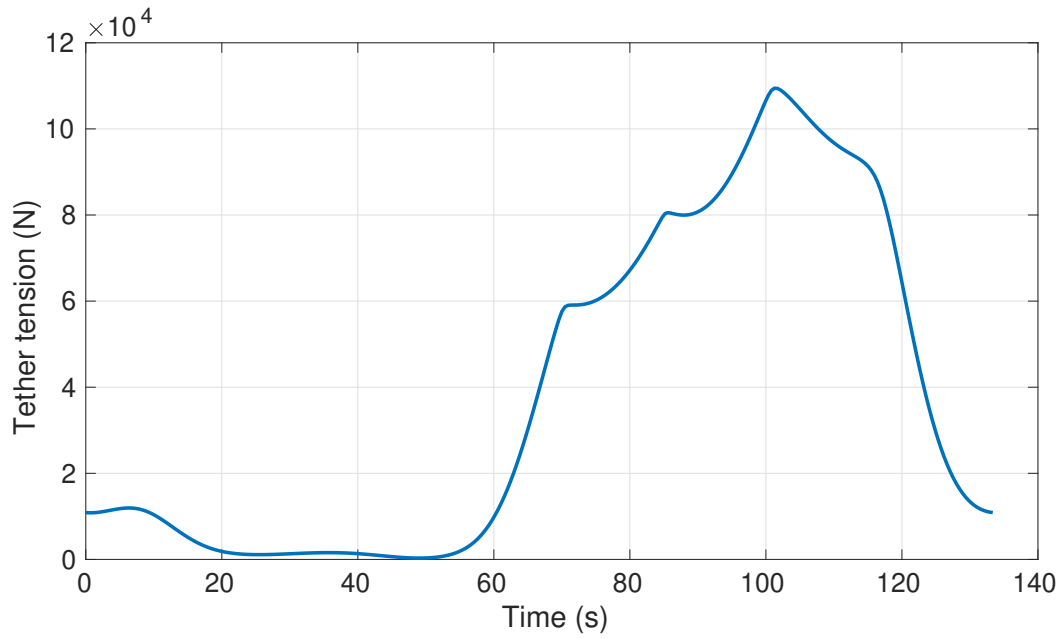(b) Lift-to-Drag Ratio Vs. Angle of Attack

Figure 4.9: Tether Tension

The roll angle does not change sign during the duration of the trajectory, and reaches a maximum value during spool-in, as shown in Figure 4.10. This causes the tether tension and lift vector to be misaligned, and thereby ensures low tension spool-in.
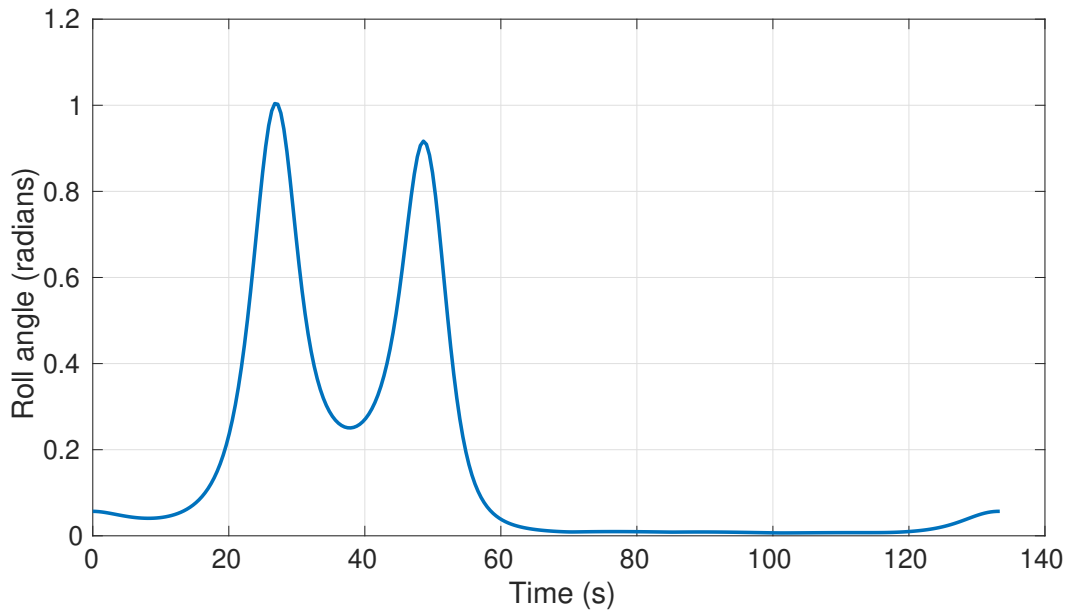

Figure 4.10: Roll Angle

The above results are appealing for at least four reasons. First, from a fundamental perspective, the results represent the first optimization study where both spooling and cross-current motion were co-optimized using direct transcription, with an underlying analytic solution of the inverse kite dynamics. Second, from a practical perspective, the results furnish a kite trajectory that confirms the attainability of significant energy harvesting through cross-current motion, confirming earlier findings by the author based on an approximate solution of the kite dynamics. Third, the results provide new insights into the shape of the optimal kite trajectory. In particular, they highlight the degree to which circular trajectories can potentially provide energy harvesting benefits similar to those seen in the literature with figure-8 trajectories. Moreover, they highlight the degree to which kite reeling motion can take place, at least partially, in plane, as opposed to in alignment with the free-stream fluid velocity. This is particularly attractive from the perspective of multi-kite spacing in a farm of kites, where the smaller the total distance taken up by each kite in the free-stream fluid direction, the greater the potential for maximizing effective overall farm power density.

4.4   Conclusion

This chapter presents the first effort to solve the co-optimization problem along with the inverse dynamics of the kite analytically. The simulation study highlights how the inverse dynamics can provide useful insights into the trajectory optimization, and the degree to which cross-current trajectory optimization are beneficial for MHK systems. Future work can take into account the actuator dynamics, lower-level controllers, tether dynamics, added/entrained mass, and other fluid-structure interaction effects.

Chapter 5:   Free Stream Velocity Estimation using Unscented Kalman Filter

5.1   Overview

The previous chapters in this dissertation assume that the free stream fluid velocity is both known and spatio-temporally constant at a rate of $1 \mathrm{m\,s}^{-1}$ in the inertial x-direction. However, this is not a realistic assumption. As mentioned in Section 1.2.2, several of the methods typically used for the fluid flow estimation are not suitable for use underwater. This chapter uses the MATLAB implementation of the unscented Kalman filter to estimate both the kite's state and the free stream fluid velocity. This is a combined state and disturbance estimation problem, where estimating the kite's state serves as a precursor to the critical goal of free stream fluid velocity estimation. In this estimation study, we assume we can measure the tether length, the azimuth and elevation angles, the Euler angles, and the relative velocity in the body frame. We estimate the Euler angles, the kite's inertial position and velocity, and the free stream fluid velocity. The rest of the chapter is organized as follows: Section 5.2 introduces the state space model used for estimation; Section 5.4 discusses the simulation results; Section 5.5 uses Fisher information analysis to analyze the results; finally, Section 5.6 provides a pathway for future work[1].

---

[1]The work in this chapter is currently in preparation for submission as a peer-reviewed publication.

5.2   Equations of Motion

The kite model presented in this section makes similar assumptions regarding the kite's tether as previous chapters, i.e., the kite's tether is a massless, drag-free straight light kinematic constraint. This assumption has been examined in previous work done by Alvarez *et al.* [34]. Two coordinate frames are used to model the kite system: *i* an inertial reference frame and *ii* a body frame (as opposed to the wind frame used in earlier chapters). The position $\vec{r}$ and velocity $\vec{V}$ of the kite, and the fluid velocity, are defined in the inertial frame, as shown in the previous chapters.

The body axes are normally aligned (x', y', z'), forward, right, and down. The "forward" axis is aligned with the longitudinal reference line of the kite, and the right and down axes are defined such that the down direction is in the kite's plane of symmetry. In this chapter, any vector described in the body frame will be denoted with a prime. Three Euler angles are defined to transform an inertial axis vector to a body axis vector. The Euler angles follow a classical 3-2-1 sequence, [53]. Therefore, starting from the reference system, the sequence of rotations is:

1. Right-handed rotation about the z-axis, or positive ψ (compass heading/yaw)

2. Right-handed rotation about the new y-axis, or positive θ (pitch)

3. Right-handed rotation about the new x-axis, or positive ϕ (roll)

5.2.1   State Variables

There are 12 state variables: the three Euler angles, the position of the kite in the inertial frame, the velocity in the inertial frame, and the wind velocity vector in the inertial frame. This

choice of state variables reflects the following important decisions and choices regarding the underlying unscented Kalman filtering problem. First, incorporating the three components of the free stream fluid velocity (or "wind velocity") as fictitious state variables allows the unscented Kalman filter to simultaneously estimate the kite's state and external wind disturbance, thereby furnishing a fluid velocity estimator. Second, the use of Euler angles to describe the kite's attitude simplifies the unscented Kalman filtering problem by eliminating the need for constrained estimation (in contrast to the use of quaternion parameters, where a constraint on the magnitude of the quaternion vector must be enforced at every instant in time). This simplification comes at a price, namely, the well-known vulnerability of Euler angle-based attitude representations to the Euler singularity: an issue that can be resolved by reverting to a quaternion parameter-based representation of kite attitude. Finally, the inclusion of kite velocity in the state vector, coupled with the exclusion of kite angular velocity from the same state vector, reflects a decision to perform estimation based on a combination of translational kinematics, rotational kinematics, and translational dynamics. With these decisions in mind, the state vector is given by:

$$
\begin{bmatrix} x_1 \\ x_2 \\ x_3 \\ x_4 \\ x_5 \\ x_6 \\ x_7 \\ x_8 \\ x_9 \\ x_{10} \\ x_{11} \\ x_{12} \end{bmatrix} = \begin{bmatrix} \psi \\ \theta \\ \phi \\ x_{kite} \\ y_{kite} \\ z_{kite} \\ u_{kite} \\ v_{kite} \\ w_{kite} \\ u_{wind} \\ v_{wind} \\ w_{wind} \end{bmatrix} \tag{5.1}
$$

5.2.2   Input Variables

The input variables are: the angular velocity vector in the body frame, and the measured acceleration vector in the body frame. These quantities do not necessarily represent physical actuation inputs to the tethered kite. Rather, they represent quantities that are assumed in this chapter to be measurable (using, say, an onboard inertial measurement unit), and can be employed as input variables in a kite plant model for the purposes of unscented Kalman filter-based state estimation. The prime indicates that the measurements are in the body frame, where p', q', and r' are the roll, pitch, and yaw rate components of the angular velocity respectively. This furnishes the input vector below:

$$
\begin{bmatrix} u_1 \\ u_2 \\ u_3 \\ u_4 \\ u_5 \\ u_6 \end{bmatrix} = \begin{bmatrix} p' \\ q' \\ r' \\ \dot{u}'_{kite} \\ \dot{v}'_{kite} \\ \dot{w}'_{kite} \end{bmatrix}
\tag{5.2}
$$

5.2.3   Output variables

To implement an unscented Kalman filter, one needs to define a set of underlying output equations. The output variables represented by these equations are physical quantities that are assumed to be directly measured, and potentially useful for kite state estimation. We start with the bare minimum of output equations. First, we assume that the velocity of the kite relative to the surrounding fluid, $\vec{V}'_{rel}$, can be measured in the kite's body frame. At least two different possible sets of sensors potentially enable such measurement, namely, either: (i) a set of 3 orthogonal Pitot tubes or (ii) a Pitot tube pointing along the kite's x-axis, plus an angle of attack sensor, plus a side-slip angle sensor (the latter sensor is not needed if the assumption of zero side-slip holds true). Regardless of how they are measured, the three components of the body frame relative velocity will constitute our first three output equations. In the base frame, the relative velocity is defined as the difference between the kite and the fluid velocity. This leads to the three output equations below:

$$\vec{V}'_{rel} = \mathbf{R} \begin{bmatrix} u_{kite} - u_{wind} \\ v_{kite} - v_{wind} \\ w_{kite} - w_{wind} \end{bmatrix} \tag{5.3}$$

$$\begin{bmatrix} y_1 \\ y_2 \\ y_3 \end{bmatrix} = \mathbf{R} \begin{bmatrix} x_7 - x_{10} \\ x_8 - x_{11} \\ x_9 - x_{12} \end{bmatrix} \tag{5.4}$$

The second set of output equations will pertain to the azimuth and elevation angles of the kite relative to its base station. We will assume that these angles can be measured by line angle sensors attached to the kite's tether, which we assume to be a straight-line kinematic constraint. Tether curvature can be substantial in practical MHK systems, as shown by Leonard et al. [40]. In situations where the kite's tether can no longer be approximated by a straight line kinematic constraints, corrections for tether curvature may be needed in order to infer the kite's azimuth and elevation angles from line angle sensor measurements. Developing algorithms to make such corrections is an important open question for future research. Regardless of how kite azimuth and elevation angle are measured, estimated, and/or corrected, the equations below define these two output quantities for the purpose of unscented Kalman filtering:

$$\beta = \arctan \frac{x_{kite}}{y_{kite}} \tag{5.5}$$

$$\epsilon = \arctan \frac{z_{kite}}{y_{kite}} \tag{5.6}$$

It is also assumed that the kite's Euler angles can be measured, making them the third set of output variables. The fourth and last set of output equations will be the tether length, l, which may potentially be measured using a kite platform-based tether release encoder, leading to the final output equation below:

$$l = \sqrt{x_4^2 + x_5^2 + x_6^2} \tag{5.7}$$

Altogether, the above equations define a total of 9 output variables for the purpose of kite state estimation, namely: three components of kite velocity relative to the surrounding fluid, the kite's azimuth and elevation angles as seen from its platform, the kite's Euler angles, and finally the total released tether length. Measuring all 9 of these output variables is possible and plausible, but may potentially be challenging. For example, a modern inertial measurement unit (IMU) may be able to infer the kite's orientation by detecting the earth's local magnetic field (using a magnetometer) and the direction of the acceleration of gravity (using an accelerometer). However, an important question arises regarding whether it is possible to estimate the kite's state variables without needing such IMU-based attitude measurements. One goal of this chapter is to compare the kite state estimation accuracy levels achieved with versus without direct measurements of kite

attitude.

5.2.4 Rotation Matrix

The above output equations contain a rotation matrix, $\mathbf{R}$, relating the kite's body frame to the inertial reference frame. Coordinate frame rotations are often described as a yaw-pitch-roll sequence, starting from the reference system. The rotation matrix for the particular sequence assumed in this chapter is is:

$$
\mathbf{R}_\psi = \begin{bmatrix} \cos(\psi) & \sin(\psi) & 0 \\ -\sin(\psi) & \cos(\psi) & 0 \\ 0 & 0 & 1 \end{bmatrix} \tag{5.8}
$$

$$
\mathbf{R}_\theta = \begin{bmatrix} \cos(\theta) & 0 & -\sin(\theta) \\ 0 & 1 & 0 \\ \sin(\theta) & 0 & \cos(\theta) \end{bmatrix} \tag{5.9}
$$

$$
\mathbf{R}_\phi = \begin{bmatrix} 1 & 0 & 0 \\ 0 & \cos(\phi) & \sin(\phi) \\ 0 & -\sin(\phi) & \cos(\phi) \end{bmatrix} \tag{5.10}
$$

$$
\mathbf{R} = \mathbf{R}_\phi \mathbf{R}_\theta \mathbf{R}_\psi \tag{5.11}
$$

5.2.5 Relation between Euler angles and angular velocity

To construct an unscented Kalman filter based on the above choices of kite state, input, and output variables, one must first write down the state and output equations in the underlying kite model. The kite's output equations are already listed in the above discussion. This section focuses on delineating three of the kite's state equations - namely, the state equations corresponding to the kite's rotational kinematics. Specifically, the state equations for the Euler angles with the angular velocity components as the inputs are:

$$
\begin{bmatrix} \dot{\phi} \\ \dot{\theta} \\ \dot{\psi} \end{bmatrix} = \begin{bmatrix} 1 & \sin\phi\tan\theta & \cos\phi\tan\theta \\ 0 & \cos\phi & -\sin\phi \\ 0 & \frac{\sin\phi}{\cos\theta} & \frac{\cos\phi}{\cos\theta} \end{bmatrix} \begin{bmatrix} p' \\ q' \\ r' \end{bmatrix} \tag{5.12}
$$

$$
\dot{\psi} = q'\frac{\sin\phi}{\cos\theta} + r'\frac{\cos\phi}{\cos\theta} \tag{5.13}
$$

$$
\dot{\theta} = q'\cos\phi - r'\sin\phi \tag{5.14}
$$

$$
\dot{\phi} = p' + (q'\sin\phi + r'\cos\phi)\tan\theta \tag{5.15}
$$

5.2.6 Remaining state equations

Beyond the above equations describing the kite's rotational kinematics, 9 more state equations are needed in order for the kite's state-space model to be complete. The state equations for the kite's velocity in the inertial frame can be written in terms of the kite's measured (i.e.,

"input") accelerations in the body frame plus the rotation matrix $\mathbf{R}$, as shown below:

$$\dot{u}_{kite} = \mathbf{R}^T \dot{u}'_{kite} \tag{5.16}$$

$$\dot{v}_{kite} = \mathbf{R}^T \dot{v}'_{kite} \tag{5.17}$$

$$\dot{w}_{kite} = \mathbf{R}^T \dot{w}'_{kite} \tag{5.18}$$

Moreover, three state equations for the position of the kite in the inertial frame can simply be expressed in terms of its inertial velocity components:

$$\dot{x}_{kite} = u_{kite} \tag{5.19}$$

$$\dot{y}_{kite} = v_{kite} \tag{5.20}$$

$$\dot{z}_{kite} = w_{kite} \tag{5.21}$$

Three state equations remain - namely, those pertaining to the free stream fluid velocity components in the inertial frame of reference. Writing these state equations down is essentially an exercise in creating a local "wind model", or "fluid model", in the physical neighborhood of the kite. From a control-theoretic perspective, this is an exercise in writing down a "disturbance model" for the purpose of combined state and disturbance estimation. Perhaps the simplest disturbance modeling approach in the literature, often employed in the context of Kalman filtering, is to assume the rate of change of the disturbance to be zero, thereby assuming the disturbance to be constant but unknown. This assumption leads to the final three state equations below, with

the understanding that more sophisticated disturbance models can be used if higher estimation fidelity is desired:

$$\dot{u}_{wind} = 0 \qquad (5.22)$$

$$\dot{v}_{wind} = 0 \qquad (5.23)$$

$$\dot{w}_{wind} = 0 \qquad (5.24)$$

5.3 Estimation Algorithm Settings

We used MATLAB's built-in unscented Kalman filter (UKF) to perform state estimation for the above model, including free stream velocity estimation. In order to do so, one needs to provide the estimator with initial guesses of the state, output, and input variables, as well as estimates of the measurement and process noise co-variance matrices. The UKF algorithm assumes that the measured kite outputs and the dynamics of the kite are corrupted by zero mean, white, and Gaussian measurement and process noise signals, respectively.

The true values of the kite model's output variables, at every instant in time, can be computed using Equations 5.3, 5.5, 5.6, and 5.7. This computation requires perfect knowledge of the state and input variables at every instant in time. These true state and input values, at every instant in time, are obtained from the simulation study in Chapter 4, together with Equations 5.1 and 5.2. This creates a simulation study where the true initial values of the state, input, and output variables are given by the three tables below. These true initial conditions are treated by the UKF algorithm as unknown.

States	Initial Value	Units
ψ	1.533	rad
θ	-1.424	rad
ϕ	3.0511	rad
x_{kite}	276.06	m
y_{kite}	25.105	m
z_{kite}	39.496	m
u_{kite}	0.9953	$\mathrm{m\,s^{-1}}$
v_{kite}	0.5371	$\mathrm{m\,s^{-1}}$
w_{kite}	-3.655	$\mathrm{m\,s^{-1}}$
u_{fluid}	1	$\mathrm{m\,s^{-1}}$
v_{fluid}	0	$\mathrm{m\,s^{-1}}$
w_{fluid}	0	$\mathrm{m\,s^{-1}}$

Table 5.1: True Initial State Values

Outputs	Initial Value	Units
ψ	1.5334	rad
θ	-1.424	rad
ϕ	3.051	rad
l	280.007	m
β	0.0906	rad
ϵ	0.1421	rad
u'_{rel}	-3.537	$\mathrm{m\,s^{-1}}$
v'_{rel}	-0.1207	$\mathrm{m\,s^{-1}}$
w'_{rel}	1.0572	$\mathrm{m\,s^{-1}}$

Table 5.2: True Initial Outputs

To run the UKF algorithm, one must provide guesses/estimates of the initial values of the state, input, and output variables. These assumed initial values should be sufficiently different from the true values to enable testing the UKF algorithm's convergence and estimation performance. Tables 5.4, 5.5, and 5.6 provide the initial estimates of the state, output, and input variables, respectively, that are used throughout the remainder of this chapter's simulation studies. One goal of the simulation studies is to examine the degree to which the discrepancies between these initial estimates and the true initial conditions of the kite diminish with time. A second goal is to examine the degree to which this estimation performance depends on the ability to measure

74

Inputs	Initial Value	Units
p'	-0.1339	$\mathrm{rad\,s^{-1}}$
q'	0.1644	$\mathrm{rad\,s^{-1}}$
r'	0.0263	$\mathrm{rad\,s^{-1}}$
$\dot{u}'_{kite}$	-0.0173	$\mathrm{m\,s^{-2}}$
$\dot{v}'_{kite}$	0.0781	$\mathrm{m\,s^{-2}}$
$\dot{w}'_{kite}$	-0.5843	$\mathrm{m\,s^{-2}}$

Table 5.3: True Initial Input Values

the kite's attitude (i.e., its Euler angles) versus time. A third goal is to examine the degree to which this estimation performance depends on the magnitudes of the process and measurement noise signals.

States	Initial Value	Units
ψ	5	rad
θ	0.5	rad
ϕ	1.5	rad
x_{kite}	250	m
y_{kite}	50	m
z_{kite}	100	m
u_{kite}	0.5	$\mathrm{m\,s^{-1}}$
v_{kite}	1.5	$\mathrm{m\,s^{-1}}$
w_{kite}	0.01	$\mathrm{m\,s^{-1}}$
u_{fluid}	2	$\mathrm{m\,s^{-1}}$
v_{fluid}	1	$\mathrm{m\,s^{-1}}$
w_{fluid}	1	$\mathrm{m\,s^{-1}}$

Table 5.4: Initial Estimate of the States

Throughout the remainder of this chapter, the process and measurement noise signals are assumed to have diagonal covariance matrices. One goal of this work is to analyze the degree to which the magnitudes of the diagonal elements of these matrices affect the performance of the UKF algorithm. Towards this goal, assumed nominal values of the diagonal elements of the measurement and process noise covariance matrices are given below, in Tables 5.7 and 5.8. Our UKF simulation studies below can be categorized into "high covariance" and "low covariance"

Outputs	Initial Value	Units
ψ	0.01	rad
θ	0.01	rad
ϕ	0.01	rad
l	120	m
β	0.1	rad
ϵ	0.1	rad
u'_{rel}	0	$\mathrm{m\,s^{-1}}$
v'_{rel}	0	$\mathrm{m\,s^{-1}}$
w'_{rel}	0	$\mathrm{m\,s^{-1}}$

Table 5.5: Initial Estimate of the Outputs

Inputs	Initial Value	Units
p'	0.1	$\mathrm{rad\,s^{-1}}$
q'	0.1	$\mathrm{rad\,s^{-1}}$
r'	0.1	$\mathrm{rad\,s^{-1}}$
$\dot{u}'_{kite}$	1	$\mathrm{m\,s^{-2}}$
$\dot{v}'_{kite}$	1	$\mathrm{m\,s^{-2}}$
$\dot{w}'_{kite}$	1	$\mathrm{m\,s^{-2}}$

Table 5.6: Initial Estimate of the Inputs

cases. In the "high covariance" case, the tabulated process and measurement noise covariance are used for both UKF design and simulation-based UKF validation. In the "low covariance" case, the tabulated process and measurement covariance are used for UKF design, without any modifications. However, when the UKF algorithm's performance is simulated, the simulated process and measurement noise signals have covariance that are six orders of magnitude (i.e., $1,000,000$ times) smaller than the tabulated values. This is a very significant reduction in process and measurement covariance, representing a scenario where the noise processes affecting the UKF algorithm are almost nonexistent.

Outputs	Covariance
ψ	0.01
θ	0.01
ϕ	0.01
l	1
β	0.004
ϵ	0.004
u'_{rel}	0.04
v'_{rel}	0.04
w'_{rel}	0.04

Table 5.7: Measurement Noise Covariance

States	Covariance
ψ	0.01
θ	0.01
ϕ	0.01
x_{kite}	0.25
y_{kite}	0.25
z_{kite}	0.25
u_{kite}	0.25
v_{kite}	0.25
w_{kite}	0.25
u_{fluid}	0.3
v_{fluid}	0.3
w_{fluid}	0.3

Table 5.8: Process Noise Covariance

5.4   Results

This section provides three sets of simulation results. The first set of results shows the performance of the unscented Kalman filter without attitude measurement, assuming low process and measurement noise covariance. The second set of results shows estimation performance with attitude measurement, assuming low process and measurement noise covariance. Finally, the third set of results shows estimation performance with attitude measurement, assuming high process and measurement noise covariance.

5.4.1   Estimation Results without Attitude Measurement

The following results show that without the measurement of attitude, there are significant discrepancies between the estimated and true value of the kite's state variables, as well as the free stream fluid velocity. We begin by noting that in the presence of low process and measurement noise covariance, the kite's position in the inertial frame is estimated with good accuracy, as shown in Fig. 5.1. This makes intuitive sense, considering the fact that kite position can be inferred directly from measurements of the tether length, kite azimuth angle, and kite elevation angle.

In the absence of direct measurement of the kite's attitude, the UKF fails to converge to acceptable Euler angle estimates in this simulation study, as shown in Fig. 5.2. Intuitively, errors in estimating the kite's Euler angles have the potential to translate to errors in inferring its accelerations in the inertial frame of reference from measurements of its accelerations in the body frame of reference. This, in turn, has the potential to result in substantial errors in estimating the kite's inertial velocity and position vectors.The fact that the kite's position is essentially known from measurements of tether length, kite azimuth, and kite elevation, therefore provides an intuitively plausible pathway for making feedback corrections to the kite's Euler angle estimates. Unfortunately, simulating the UKF algorithm for low process and measurement noise covariance values shows that the algorithm is unable to converge to the kite's correct attitude. Errors in attitude estimation cause the kite's velocity estimation accuracy to also be poor, as evident from Fig. 5.3. However, the fact that kite position is related to kite velocity via integration with respect to time, coupled with the fact that such integration is essentially a low-pass operator in the frequency domain, causes kite position estimates to be good even while kite velocity estimates are less than

ideal. Because of the significant errors in estimating kite attitude and velocity, free stream fluid velocity estimates are quite poor in this scenario, as shown in Fig. 5.4. Significant fluctuations are seen in estimated free stream fluid velocity, even though the true fluid velocity does not fluctuate in this study. The former fluctuations can be at least partially traced to inaccuracies in kite attitude estimation, since the kite is only able to measure its velocity relative to the fluid in the body frame, as opposed to the inertial frame of reference. Thus, even with accuracy body frame relative velocity measurements, the accuracy of inertial frame relative (and fluid) velocity estimation can suffer if kite attitude is not known accurately.

5.4.2 Estimation Simulation with Attitude Measurement: Low Noise Covariance Case

This section examines the performance of the UKF algorithm in the scenario where kite attitude is measured directly. The simulation study in this section assumes low process and measurement noise covariance. The high noise covariance case is examined in the following section. The results of this section's simulation show that when kite attitude is measured, UKF estimation accuracy improves substantially across the board, especially free stream fluid velocity estimation accuracy. As shown in Fig. 5.5, once the UKF algorithm has access to low-noise kite attitude measurements, it has no difficulty generating its own accurate Euler angle trajectories matching these measurements. Moreover, as in the previous simulation study, the availability of direct measurements of tether length, kite azimuth angle, and kite elevation angle provides an intuitive explanation for the very high kite position estimation accuracy seen in Fig. 5.6. Given these accurate estimates of kite attitude and position, kite velocity estimates are quite accurate,

as shown in Fig. 5.7, leading to good free stream fluid velocity estimation accuracy, as shown in Fig. 5.8.

5.4.3 Estimation Simulation with Attitude Measurement: High Noise Covariance Case

Incorporating higher values of process and measurement noise covariance in the simulation-based validation of the UKF algorithm does not fundamentally alter the results of the previous section. Estimation accuracy continues to be attractive, across the board, provided the kite's attitude is measured directly. Specifically, kite attitude estimation accuracy continues to be reasonable, as shown in Fig. 5.9. Moreover, kite position estimation accuracy continues to be reasonable, as shown in Fig. 5.10. Noisy kite velocity estimates are generated by the UKF algorithm, as shown in Fig. 5.11, but these noisy estimates do track the true kite velocity trajectory well. Similarly, noisy estimates of free stream fluid velocity are generated by the UKF algorithm, as shown in Fig. 5.12, but on average these estimates do track the true free stream fluid velocity well. This suggests the possibility of using additional signal processing (e.g., moving average filtering, etc.) to attenuate the noise in free stream velocity estimation. One high-level insight from both this simulation cases and the preceding two simulation cases is that the availability of attitude measurements appears to improve UKF estimation accuracy substantially. This motivates the next section of this chapter, which focuses on quantifying the best achievable estimation accuracy for the given kite dynamics model, using the tool of Fisher information analysis.

For the high noise covariance case, plotting the rate of change of Euler angles, show that for our study we are not facing any Euler singularities.
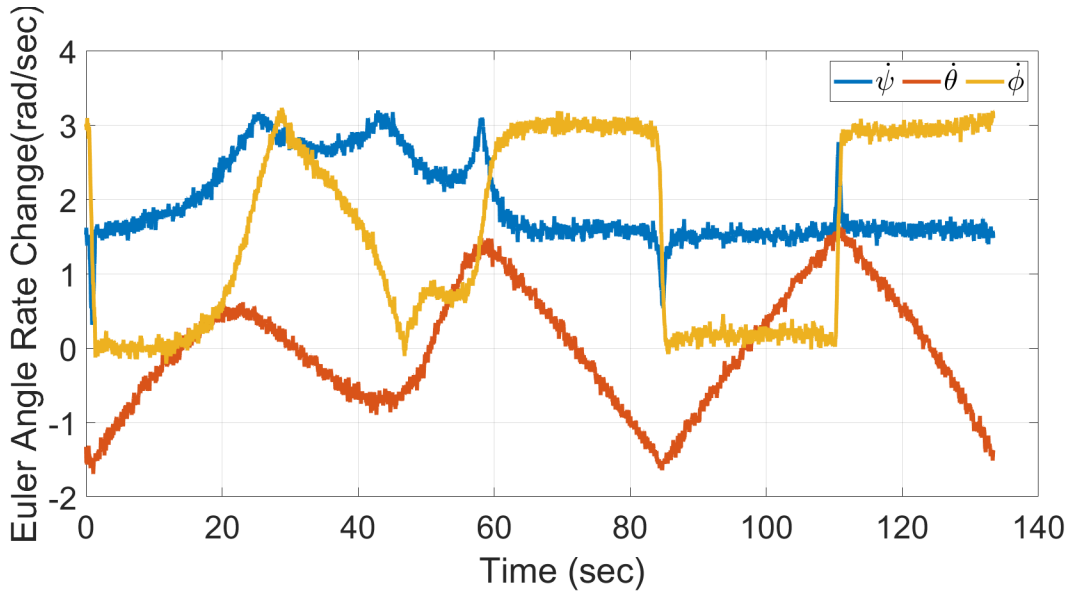
Figure 5.13: Rate of Change of Euler Angles

5.5 Fisher Information Analysis

The fact that the availability of kite attitude measurements can improve UKF estimation performance substantially raises the question of whether this improvement is a fundamental property of the kite model, a property of the specific UKF algorithm used in this chapter, or both. To address this question, this section performs classical Fisher information analysis on the kite's dynamic model. A simplified Fisher analysis is performed that accounts for output measurement noise, but neglects process noise for simplicity. Fisher analysis then proceeds as follows:

- First, the kite model is simulated from the true initial state, for the true kite input trajectory, to generate nominal histories of the kite's output variables.

- Second, the above simulation is repeated for a small perturbation in the initial condition for one of the kite's state variables, to generate perturbed output histories. The difference between each perturbed output's history and the corresponding nominal output history,

81

divided by the initial state perturbation, generates a sensitivity vector associated with that particular combination of output variable and initial condition.

- Third, each output sensitivity vector from the above step is divided by the square root of the corresponding measurement noise variance (i.e., diagonal element of the measurement noise covariance matrix). This is essentially a normalization step.

- Fourth, the scaled/normalized output sensitivity vectors corresponding to a given initial state perturbation are stacked to form a single column vector. If the number of output variables is n_o and the number of time instants in the simulation study is n_t, the end result is a column vector with $n_o \times n_t$ elements.

- Fifth, the above stacked sensitivity vectors are collected into a sensitivity matrix, $\mathbf{S}$ where each column of the matrix corresponds to a perturbation in the initial value of a given state variable. Since the kite has $n_s = 12$ state variables, the matrix $\mathbf{S}$ has $n_o \times n_t$ rows and n_s columns.

- Sixth, the product $\mathbf{S}^T\mathbf{S}$ is computed to generate (a numerical approximation of) the Fisher information matrix, $\mathbf{F}$.

- Seventh, the inverse of the Fisher information matrix is computer, furnishing the corresponding Cramér-Rao matrix.

Table 5.9 shows the values of the square roots of the diagonal elements of the above Cramér-Rao matrix, both for the case where attitude measurements are not available and for the case where those measurements are available. To interpret these results, recall that Fisher information analysis is an elementary tool from estimation theory for assessing the accuracy with

which a given estimation problem can be solved [57]. More specifically, the Fisher information matrix represents a local quantification, in an unknown parameter space, of the information associated with noisy measurements of the outputs used for parameter estimation. In the context of this particular work, the above Fisher analysis quantifies the information associated with the problem of estimating the initial values of the kite's state variables. Estimating the kite's initial states makes it possible to propagate the resulting estimates forward in time, using the kite's dynamic model. Hence, quantifying the information associated with the kite's initial states helps shed light on the accuracy with which one may be able to estimate the kite's state at subsequent moments in time. The Cramér-Rao theorem states that, for any unbiased estimator, the best achievable state estimation covariance equals the inverse of the Fisher information matrix, assuming this inverse exists. Therefore, the square roots of the diagonal terms of this inverse, as tabulated below, represent the best achievable standard deviations associated with initial kite state estimation. It is important to note that for nonlinear estimation problems, the above Fisher analysis provides a local approximation of the best achievable estimation accuracy levels.

Examining Table 5.9 in light of the above discussion reveals that the availability of direct attitude measurements reduces the best achievable attitude angle estimation errors by a factor of 4 or more. Intuitively, it makes sense for the direct measurement of attitude angles, even with measurement noise, to enable significant improvements in attitude estimation accuracy. Position estimation accuracy does not improve significantly when direct attitude measurements are available, which also makes sense considering the fact that kite position can be inferred directly from tether length, kite azimuth, and kite elevation measurements. Interestingly, improvements in the best achievable kite and free stream fluid velocity estimates, when they exist, are seen to be relatively small from this Fisher analysis. This raises the possibility that perhaps other esti-

mation algorithms, beyond the UKF algorithm explored in this work, may be able to lessen the accuracy penalty associated with the absence of direct attitude measurement. The exploration of this question is left open as a topic for potential future research.

States	Attitude Not Measured	Attitude Measured
ψ	0.0452	0.01093
θ	0.0115	0.00181
ϕ	0.04569	0.0105
x_{kite}	0.2308	0.1888
y_{kite}	1.325	1.315
z_{kite}	1.659	1.536
u_{kite}	0.0176	0.0049
v_{kite}	0.0406	0.01609
w_{kite}	0.02013	0.01664
u_{fluid}	0.0126	0.0117
v_{fluid}	0.016	0.0189
w_{fluid}	0.0238	0.0203

Table 5.9: Standard Deviation of States With & Without Attitude Measurement

5.6   Conclusion

This chapter provides an approach for estimating the kite's state and free stream fluid velocity online, instead of assuming the latter to be spatio-temporally constant. The proposed estimator can be included with a controller for real time tracking and estimation. While the unscented Kalman filter provide accurate state and disturbance estimates when kite attitude is measured directly, future work will focus on building a more sophisticated estimation algorithm for estimating fluid velocity without measuring the attitude.Moreover, future work will focus on incorporating the estimator into onboard algorithms for real time trajectory optimization.
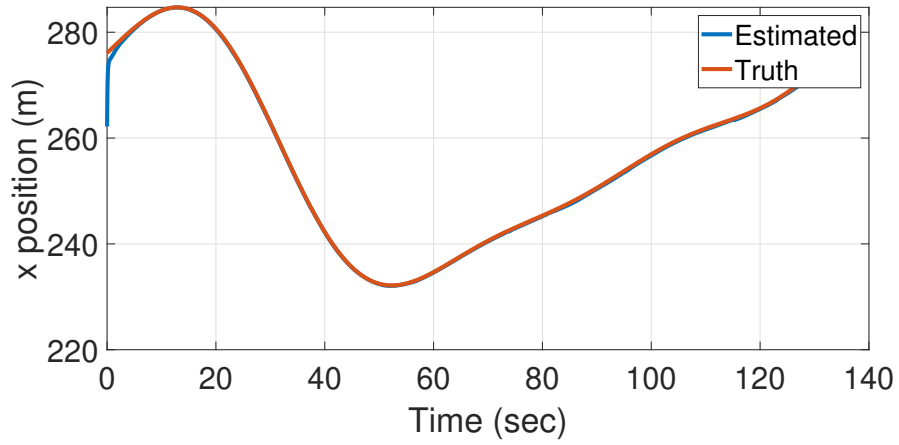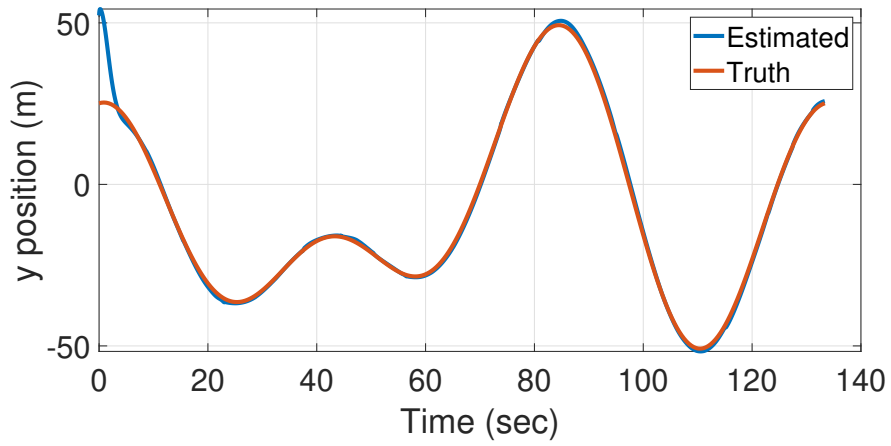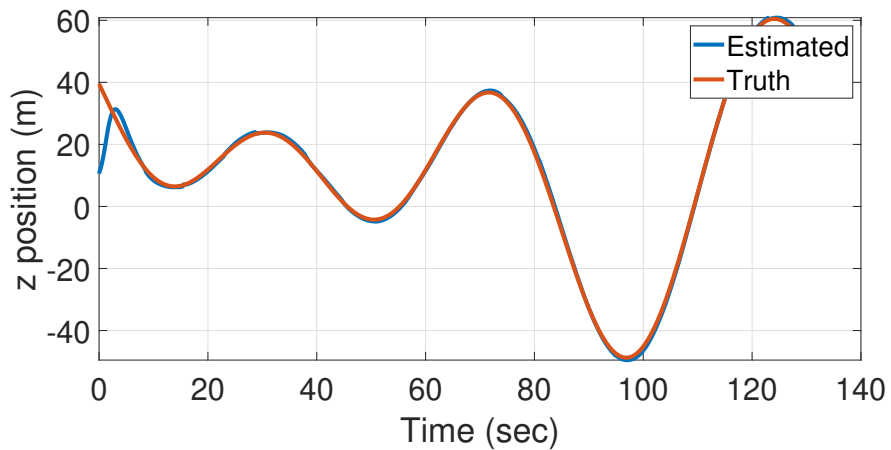
Figure 5.1: Estimated and True Values of Inertial Kite Position
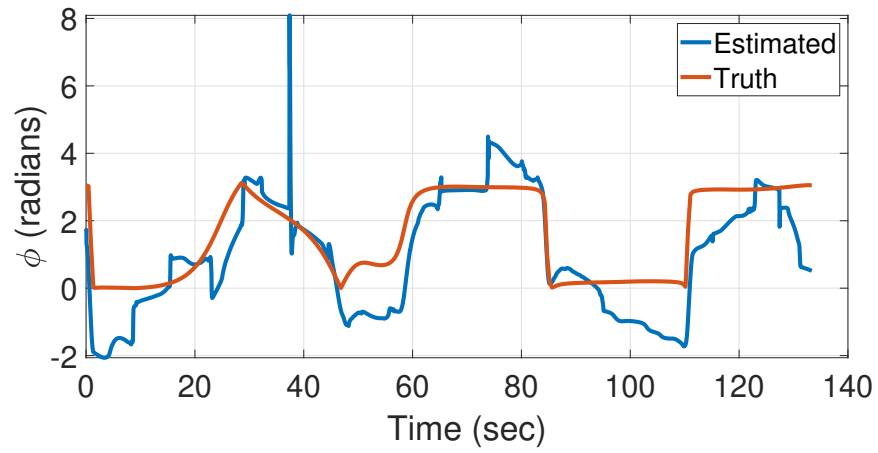
(a)
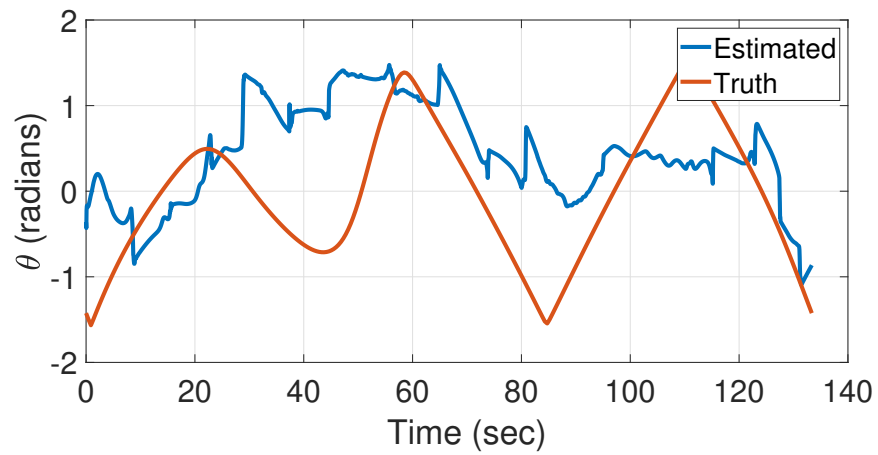
(b)
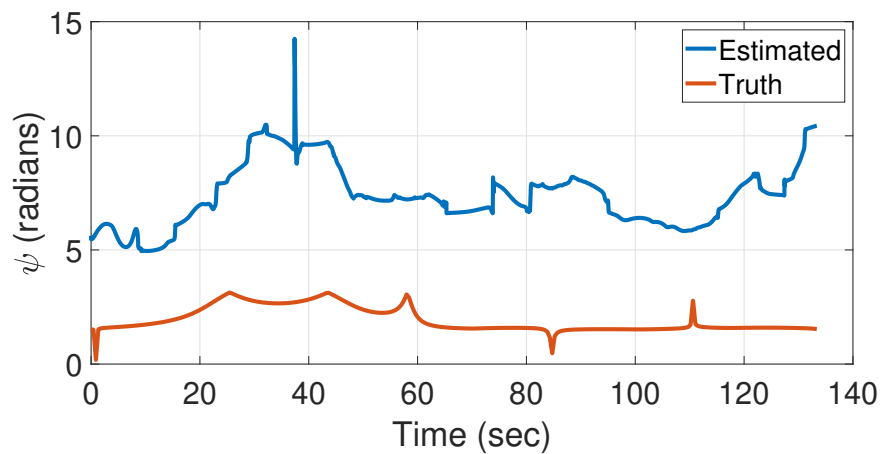
(c)

Figure 5.2: Estimated and True Values of Euler Angles

86
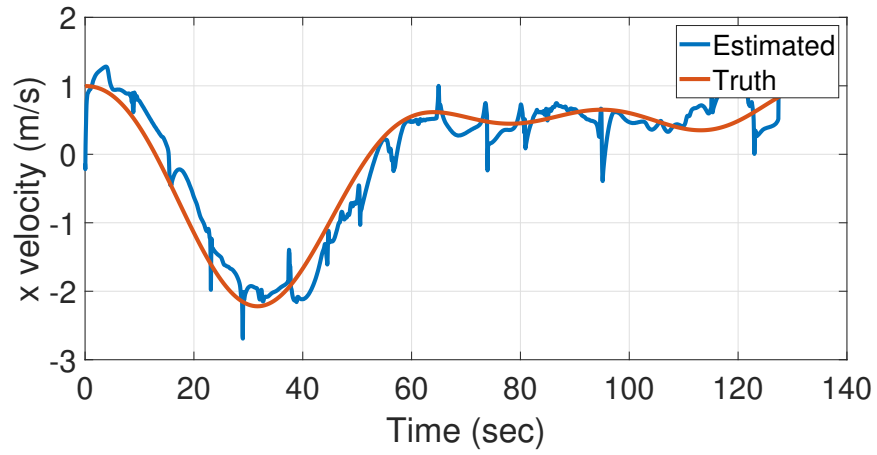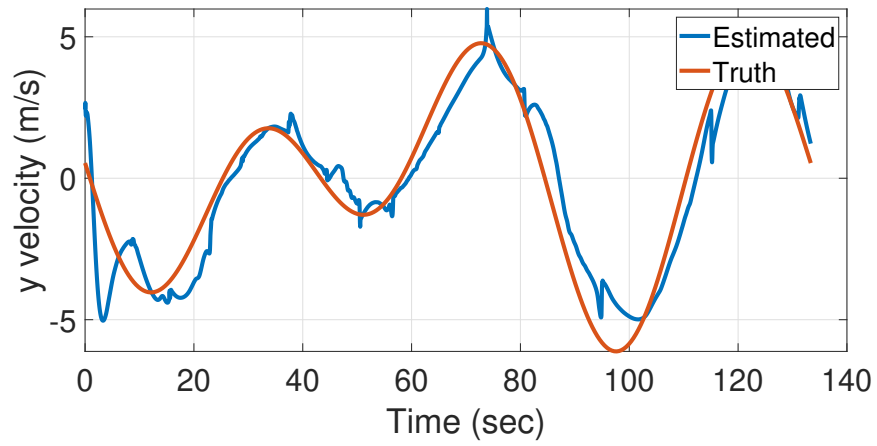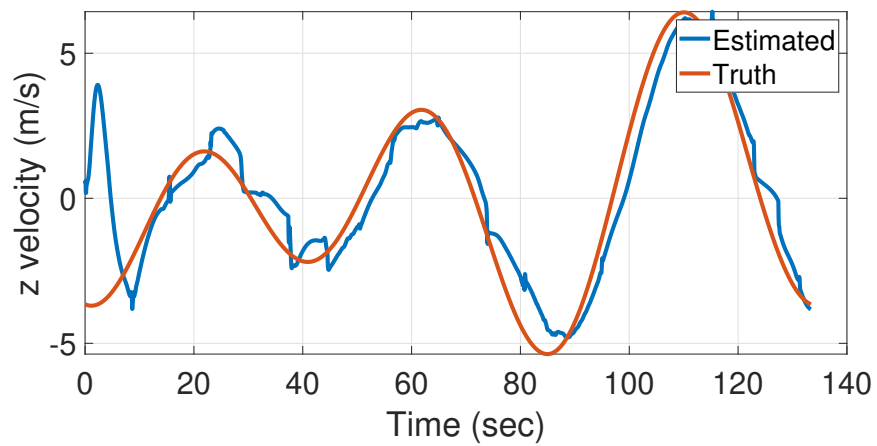
Figure 5.3: Estimated and True Values of Inertial Kite Velocity
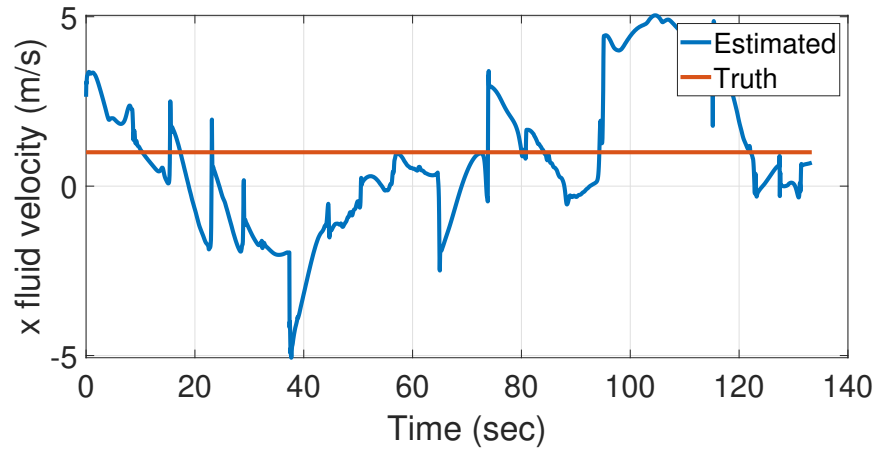
(a)
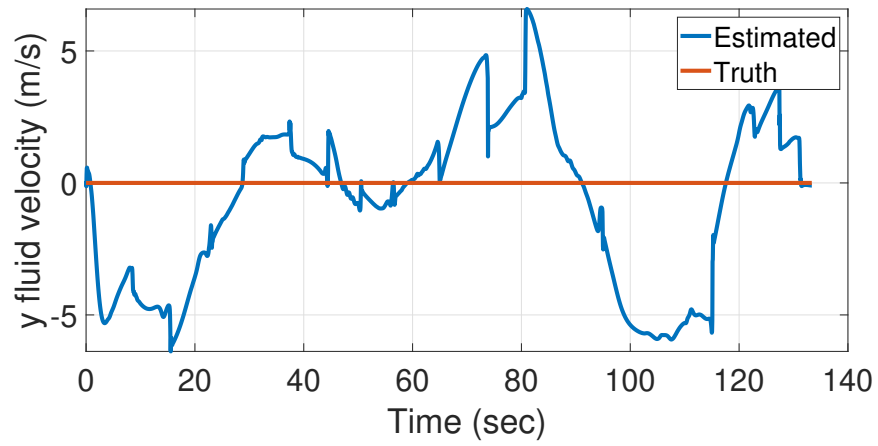
(b)
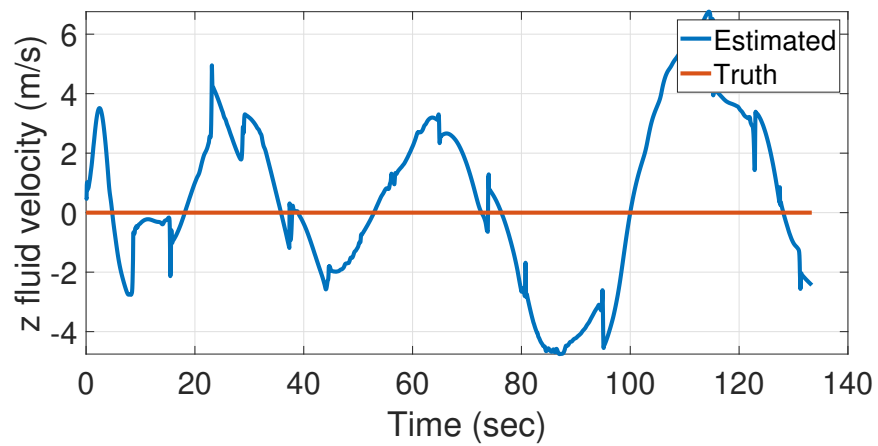
(c)

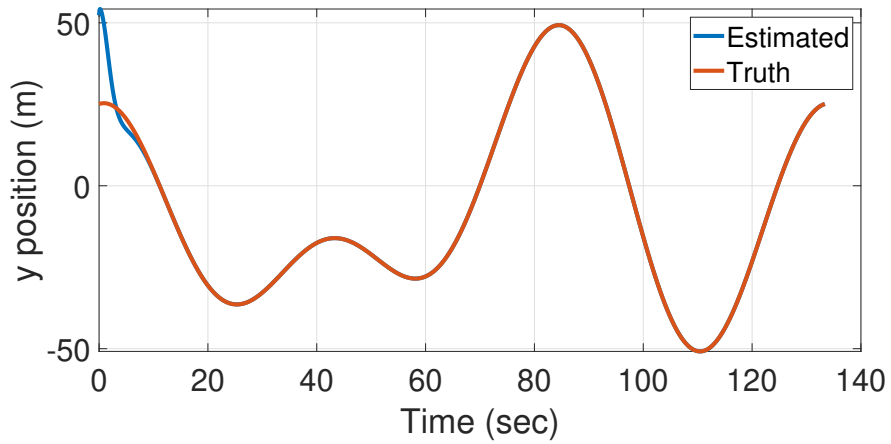Figure 5.4: Estimated and True Values of Free Stream Velocity
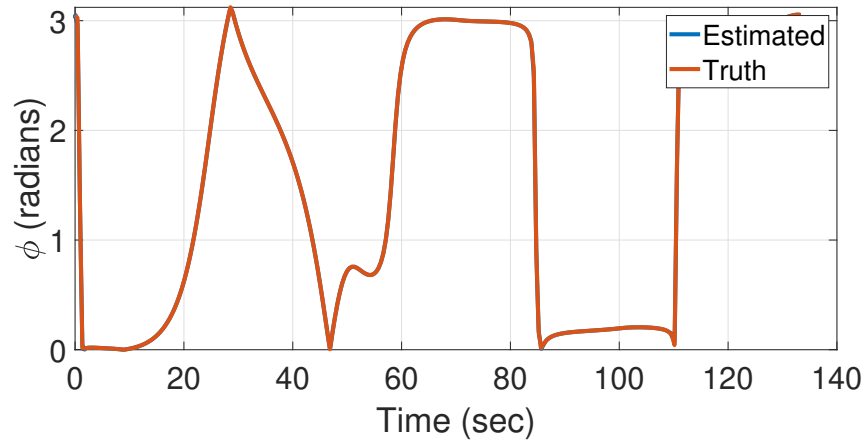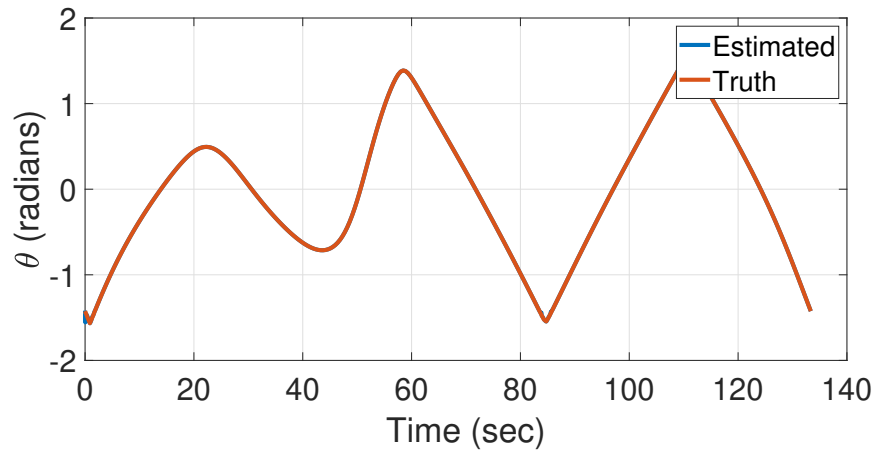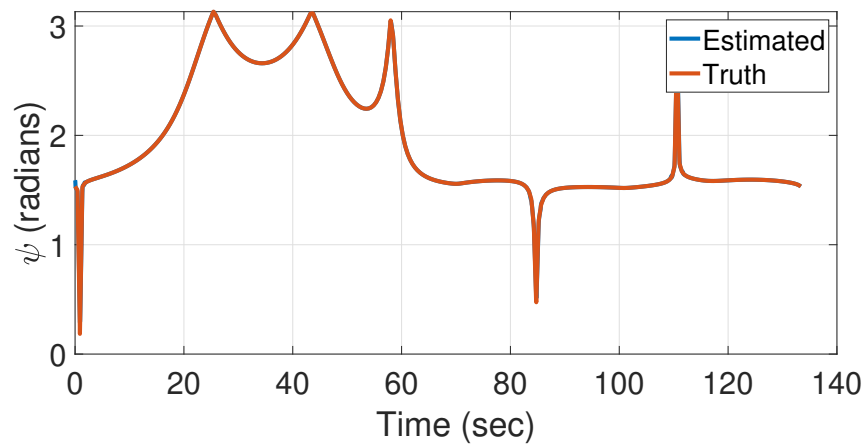
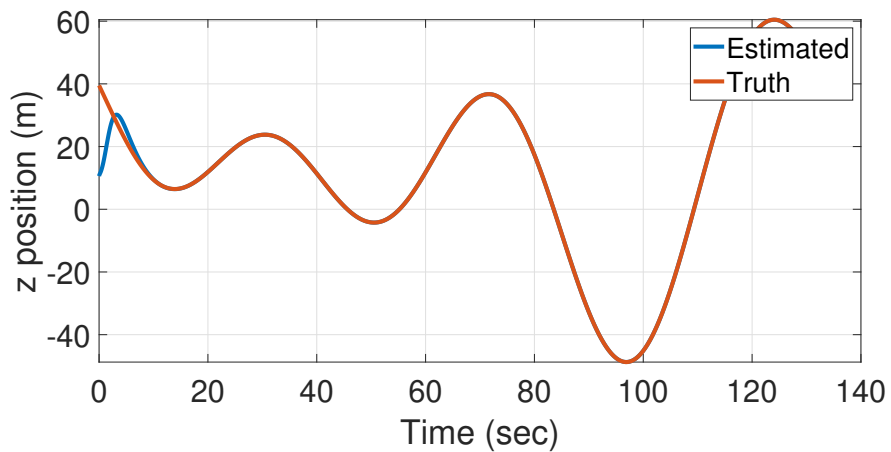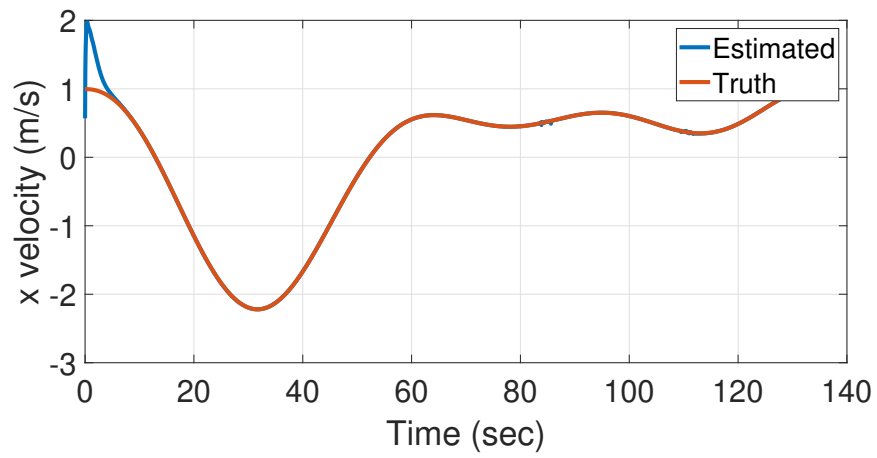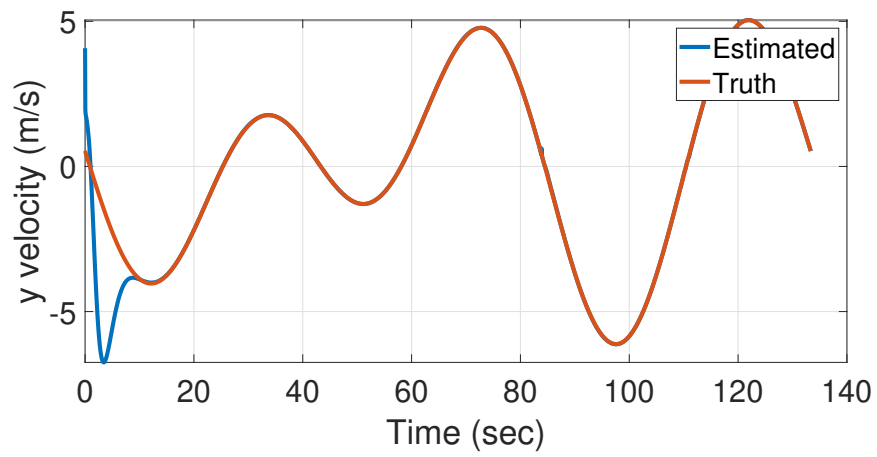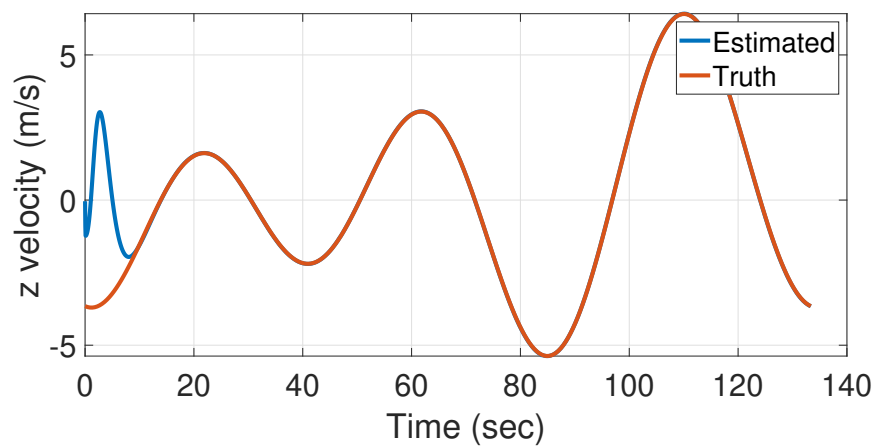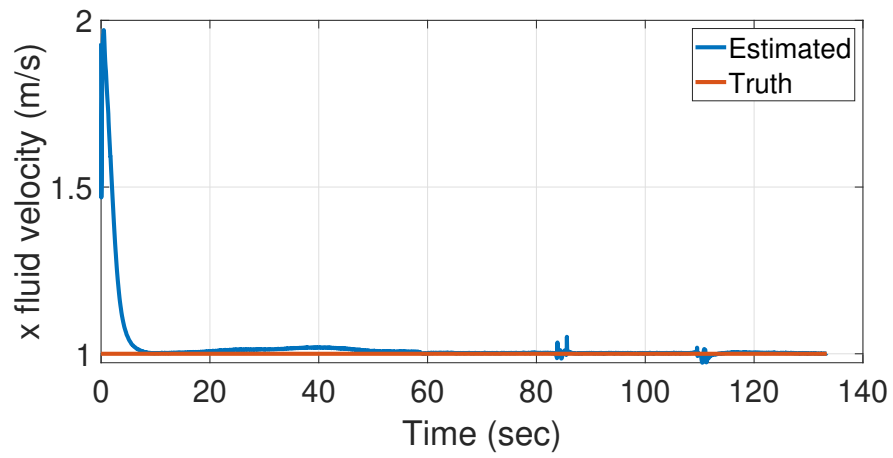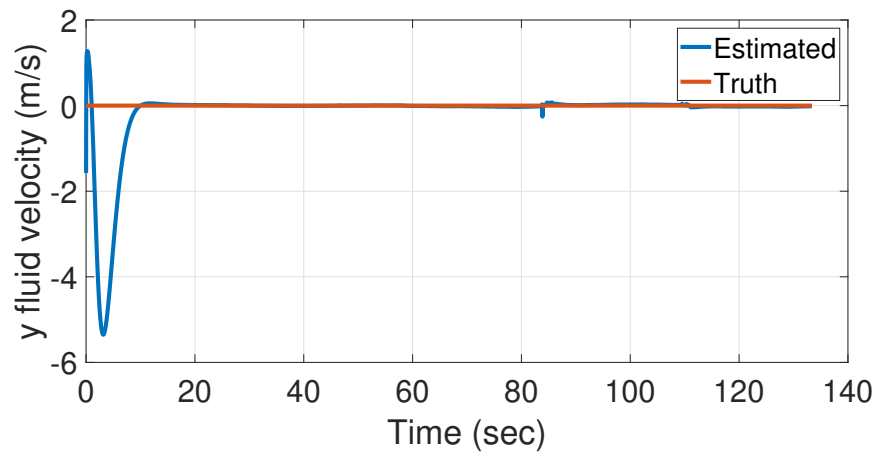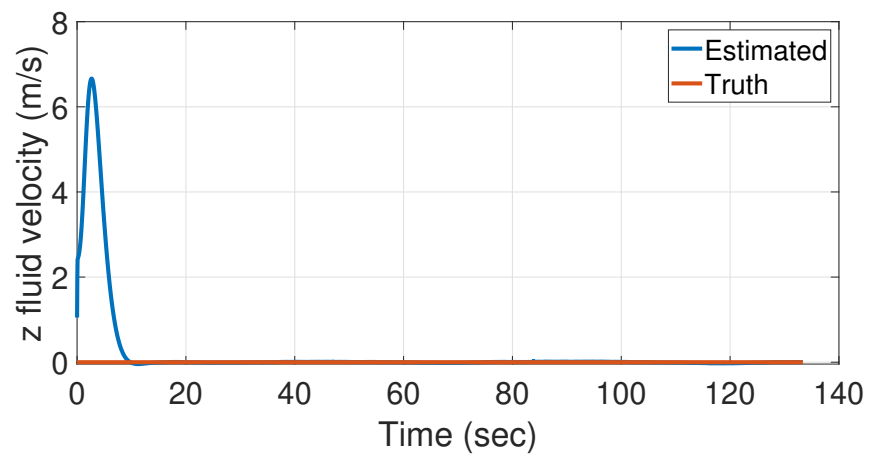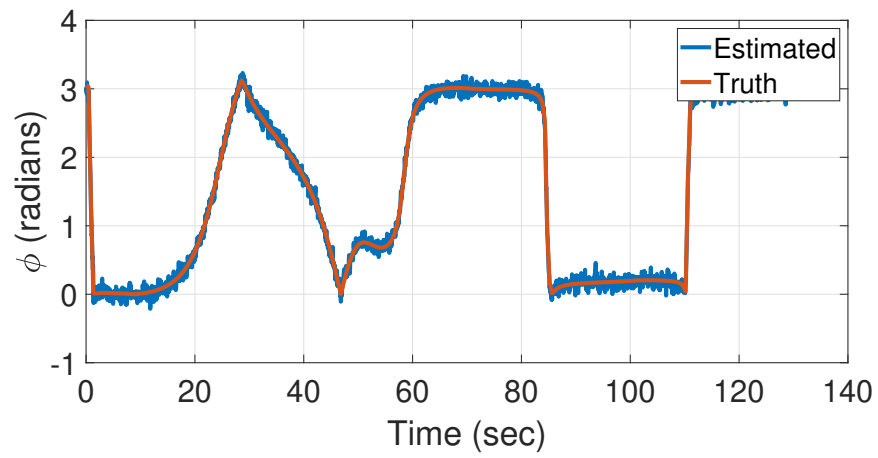Figure 5.5: Estimated and True Values of Euler Angles
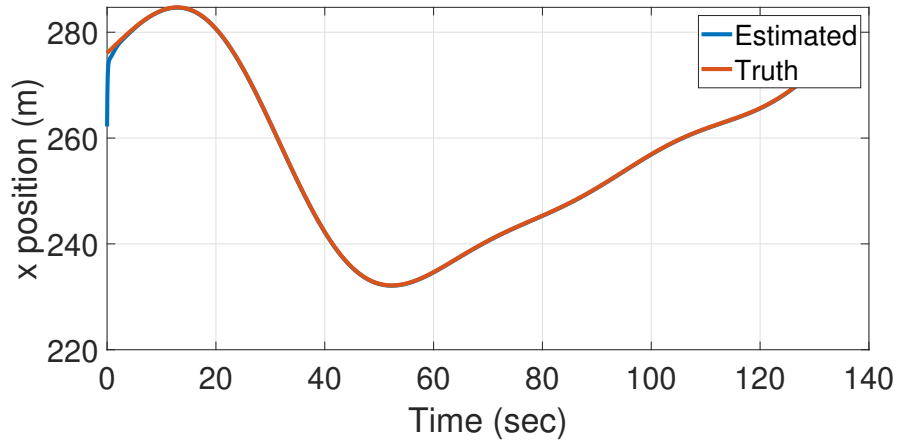
Figure 5.6: Estimated and True Values of Inertial Kite Position

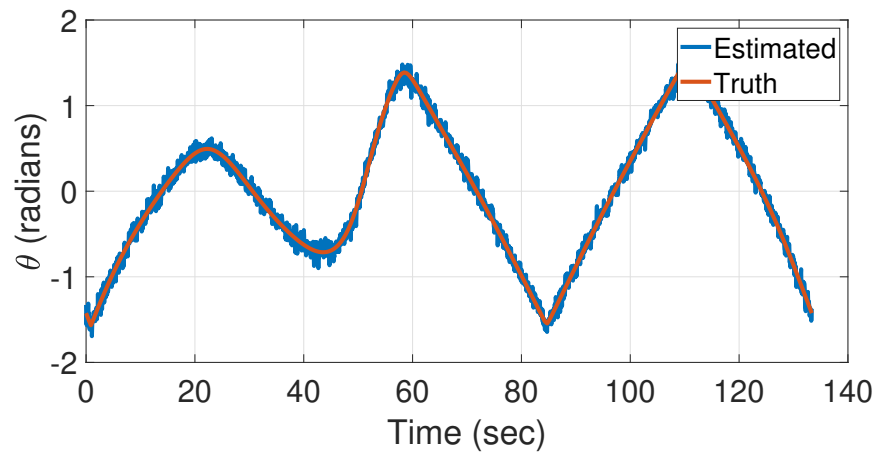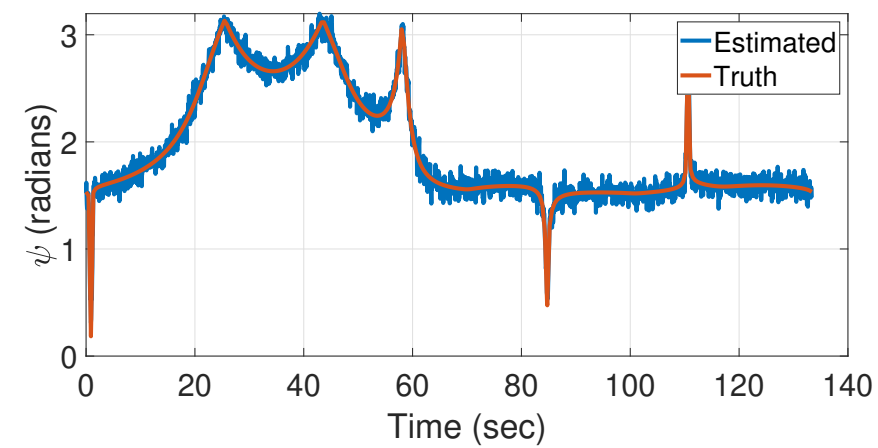Figure 5.7: Estimated and True Values of Inertial Kite Velocity

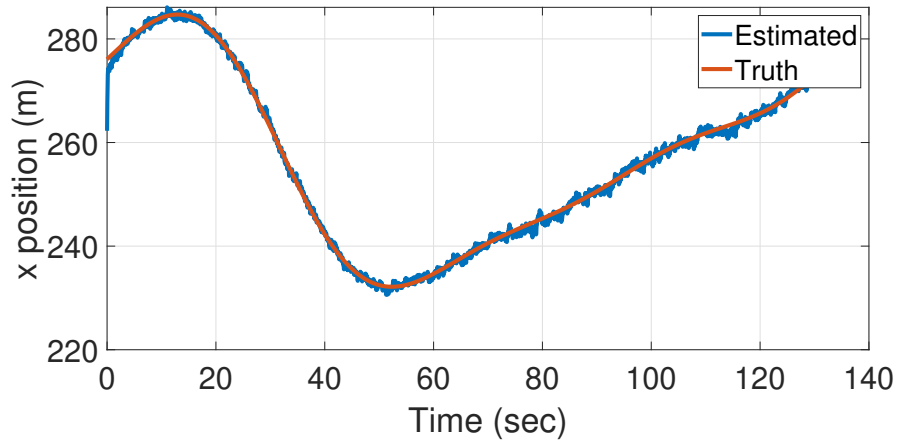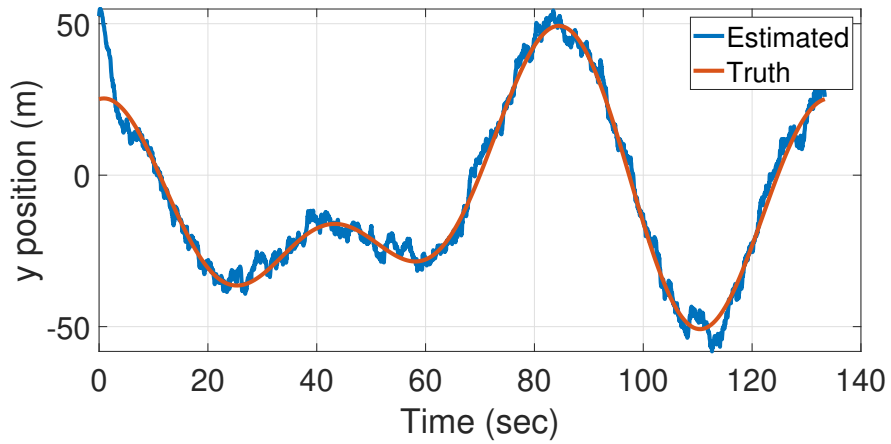Figure 5.8: Estimated and True Values of Free Stream Velocity
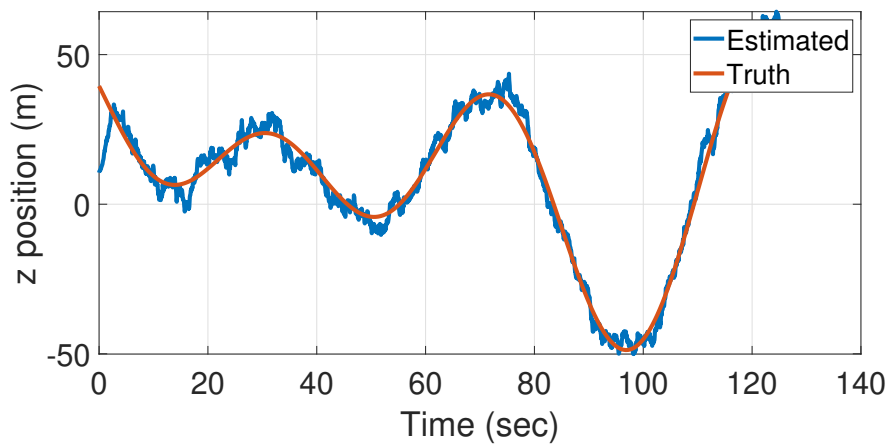
(a)

(b)

(c)

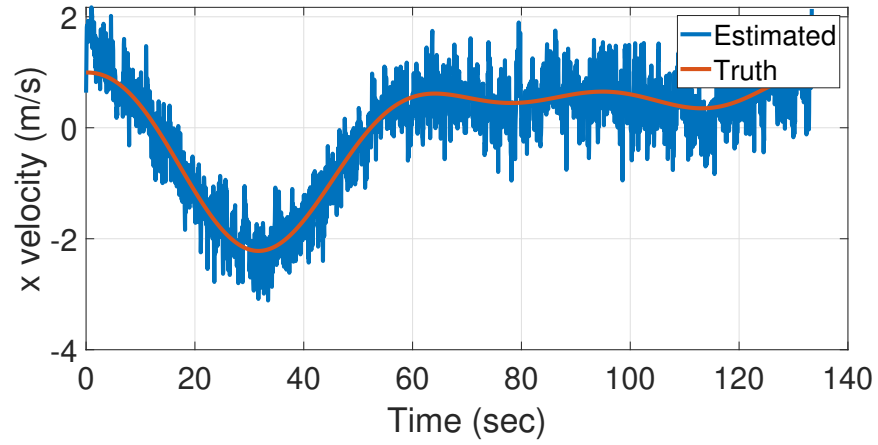Figure 5.9: Estimated and True Values of Euler Angles
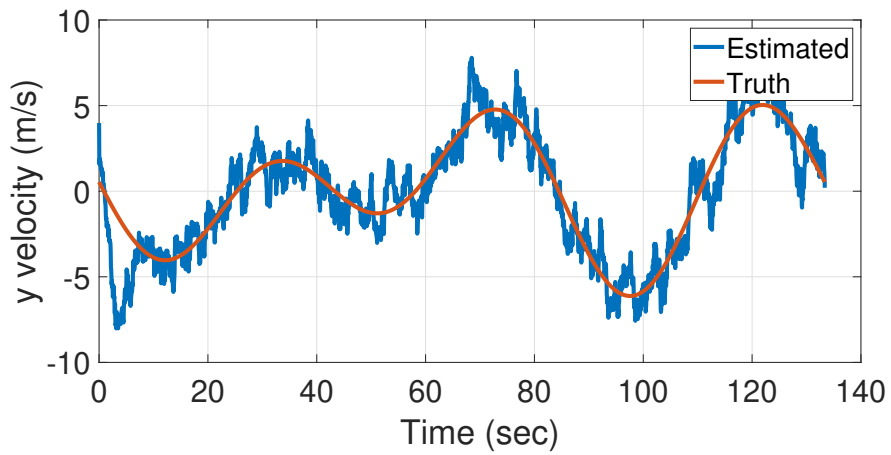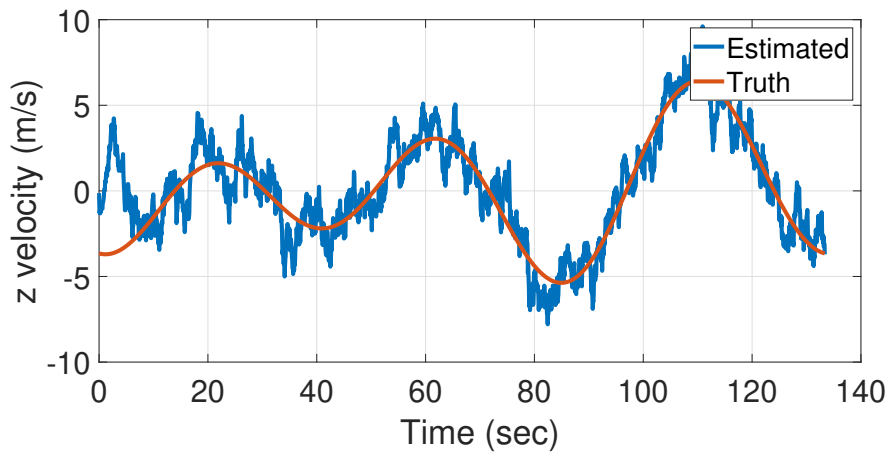
(a)

(b)

(c)

Figure 5.10: Estimated and True Values of Inertial Kite Position

(a)
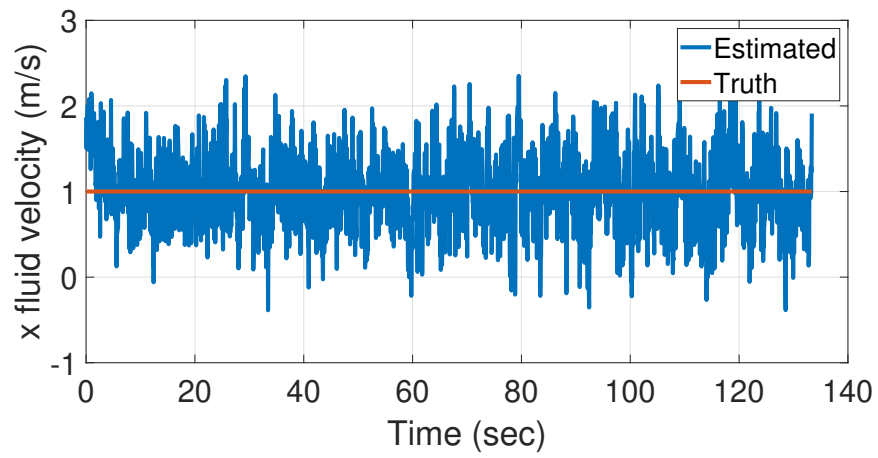
(b)
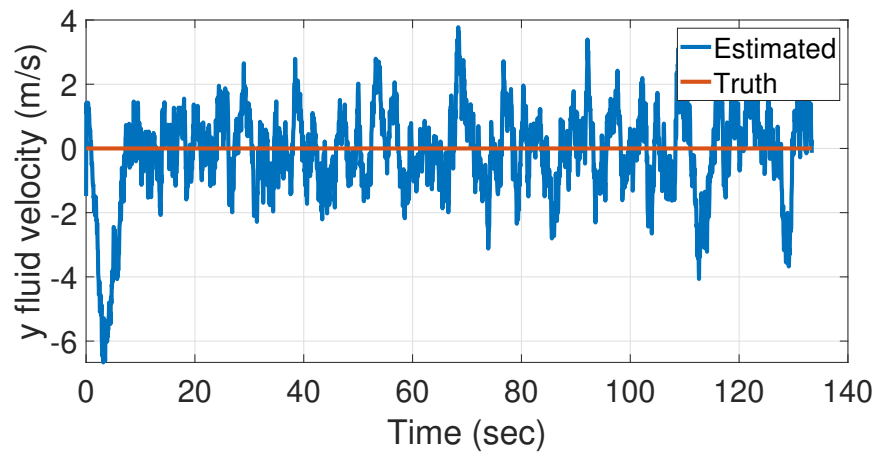
(c)

Figure 5.11: Estimated and True Values of Inertial Kite Velocity
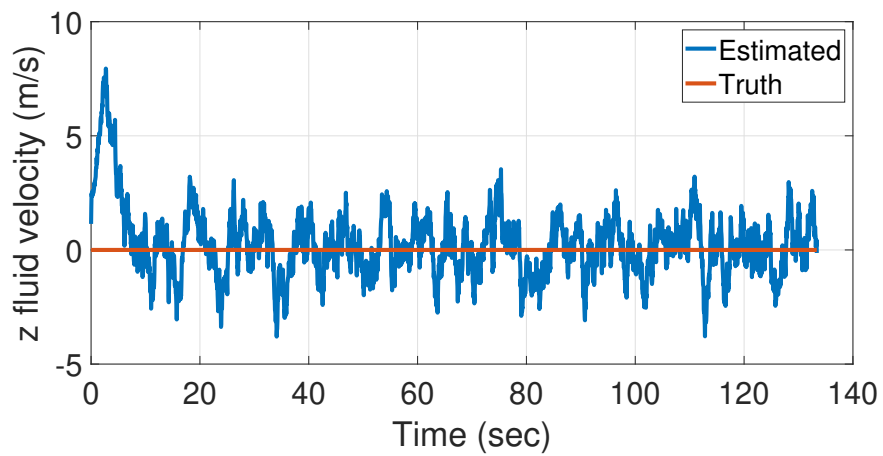
Figure 5.12: Estimated and True Values of Free Stream Velocity

Chapter 6: Conclusion

6.1 Summary

The goal of this dissertation is to provide the scientific community with algorithms for MHK kite trajectory optimization and state estimation. The dissertation presents four research contributions towards this overarching goal:

1. A direct transcription-based algorithm for nonlinear MHK kite trajectory optimization.

2. An analytic solution to the inverse dynamics of the kite model.

3. Trajectory optimization using the above inverse dynamics solution, eliminating the need for the use of penalty functions to approximate the inverse dynamics as part of direct transcription-based trajectory optimization.

4. Estimation of the kite's state and fluid velocity, modeled as a disturbance.

More specifically, Chapter 2 co-optimizes the spooling motion and the cross-current trajectory of the kite by approximating the states and inputs as truncated Fourier series, and imposing a penalty to implement the kite dynamics. To improve computational tractability and accuracy of future optimization, we develop a solution to the inverse dynamics of the kite model in Chapter 3. One interesting outcome from this study is the existence of multiple potential solution arcs: an

outcome that has intuitive graphical explanations for multiple special case scenarios. In Chapter 4 we use the inverse dynamics solution to carry on the optimization work, without needing a penalty function to approximate the kite's inverse dynamics. This results in greater accuracy by bypassing the need to impose a penalty function to ensure the dynamics. In all these chapters, we assume that the free stream fluid velocity is known and spatio-temporally constant. Therefore, in Chapter 5 we utilize unscented Kalman filtering to estimate the free stream fluid velocity plus the kite's state variables. The results provide insights into what we need and need not measure for the estimation algorithm to work properly.

6.2   Future Work

Based on the results presented in this dissertation, future work can include:

- Formulating a more advanced estimation algorithm to estimate the fluid velocity without measuring the kite Euler angles.

- Optimizing the trajectory online by incorporating the estimation algorithm into a real-time optimization framework.

- Doing trajectory optimization using other methods, such as, Pontryagin's minimum principle.

- Building a higher fidelity model for the optimization and including added/entrained mass, tether drag, the possibility of a slack tether, etc.

- Building a model of a MHK kite farm and repeating the optimization and estimation work at the farm level.

Bibliography

[1] https://www.noaa.gov/education/resource-collections/ocean-coasts.

[2] U.S. Department Of Energy. Quadrennial Technology Review: An Assessment of Energy Technologies and Research Opportunities. Technical Report September, U.S. Department of Energy, 2015.

[3] Cristina L. Archer and Ken Caldeira. Global assessment of high-altitude wind power. *Energies*, 2(2):307–319, 2009.

[4] Miles L. Loyd. Crosswind kite power (for large-scale wind power production). *Journal of Energy*, 4(3):106–111, 1980.

[5] Haocheng Li, D. J. Olinger, and M. A. Demetriou. Control of an airborne wind energy system using an aircraft dynamics model. In *2015 American Control Conference (ACC)*, pages 2389–2394, July 2015.

[6] H. Li, D. J. Olinger, and M. A. Demetriou. Control of a tethered undersea kite energy system using a six degree of freedom model. *Proceedings of the IEEE Conference on Decision and Control*, 54rd IEEE Conference on Decision and Control,CDC 2015:688–693, 2015.

[7] Haocheng Li, David J. Olinger, and Michael A. Demetriou. Modeling and control of tethered undersea kites. *Ocean Engineering*, 190:106390, 2019.

[8] Chris Vermillion, Trey Grunnagle, Ronny Lim, and Ilya Kolmanovsky. Model-based plant design and hierarchical control of a prototype lighter-than-air wind energy system, with experimental flight test results. *IEEE Transactions on Control Systems Technology*, 22(2):531–542, 2014.

[9] Chris Vermillion, Ben Glass, and Sam Greenwood. Evaluation of a water channel-based platform for characterizing aerostat flight dynamics: A case study on a lighter-than-air wind energy system. In *21st AIAA Lighter-Than-Air Systems Technology Conference*, pages 1–10, June 2014.

[10] Michelle Denlinger. *Extremum Seeking Algorithms for Optimal Periodic Cotnrol with Application to Buoyant Air Turbines*. PhD thesis, The Pennsylvania State University, 2018.

[11] Mitchell Cobb, Kira Barton, Hosam Fathy, and Chris Vermillion. An Iterative Learning Approach for Online Flight Path Optimization for Tethered Energy Systems Undergoing Cyclic Spooling Motion. In *Proceedings of the American Control Conference*, volume 2019-July, pages 2164–2170. IEEE, 2019.

[12] Mitchell Cobb, James Reed, Joshua Daniels, Ayaz Siddiqui, Max Wu, Hosam Fathy, Kira Barton, and Chris Vermillion. Iterative Learning-Based Path Optimization With Application to Marine Hydrokinetic Energy Systems. *IEEE Transactions on Control Systems Technology*, 30(2):639–653, March 2022.

[13] Massimo Canale, Lorenzo Fagiano, M Ippolito, and Mario Milanese. Control of tethered airfoils for a new class of wind energy generator. In *Proceedings of the 45th IEEE Conference on Decision and Control*, pages 4020–4026. IEEE, 2006.

[14] Massimo Canale, Lorenzo Fagiano, and Mario Milanese. Power kites for wind energy generation: Fast predictive control of tethered airfoils. *IEEE Control Systems Magazine*, 27(6):25–38, 2007.

[15] Massimo Canale, Lorenzo Fagiano, and Mario Milanese. High Altitude Wind Energy Generation Using Controlled Power Kites. *IEEE Transactions on Control Systems Technology*, 18(2):279–293, mar 2010.

[16] Boris Houska and Moritz Diehl. Optimal Control for Power Generating Kites. In *Proceedings of European Control Conference*, 2007.

[17] Boris Houska and Moritz Diehl. Optimal Control of Towing Kites. In *Proceedings of the 45th IEEE Conference on Decision and Control*, pages 2693–2697. IEEE, 2006.

[18] Tony A. Wood, Henrik Hesse, Aldo U. Zgraggen, and Roy S. Smith. Model-Based Identification and Control of the Velocity Vector Orientation for Autonomous Kites. In *2015 American Control Conference (ACC)*, volume 2015-July, pages 2377–2382. IEEE, jul 2015.

[19] Tony A. Wood, Henrik Hesse, and Roy S. Smith. Predictive Control of Autonomous Kites in Tow Test Experiments. *IEEE Control Systems Letters*, 1(1):110–115, jul 2017.

[20] Sebastian Rapp, Roland Schmehl, Espen Oland, and Thomas Haas. Cascaded Pumping Cycle Control for Rigid Wing Airborne Wind Energy Systems. *Journal of Guidance, Control, and Dynamics*, 42(11):2456–2473, nov 2019.

[21] Sebastian Rapp, Roland Schmehl, Espen Oland, Sture Smidt, Thomas Haas, and Johan Meyers. A Modular Control Architecture for Airborne Wind Energy Systems. In *AIAA Scitech 2019 Forum*, pages 1–25. American Institute of Aeronautics and Astronautics, jan 2019.

[22] James Reed, Mitchell Cobb, Joshua Daniels, Ayaz Siddiqui, Michael Muglia, and Chris Vermillion. Hierarchical Control Design and Performance Assessment of an Ocean Kite in a Turbulent Flow Environment. *IFAC-PapersOnLine*, 53(2):12726–12732, 2020.

[23] James Reed, Joshua Daniels, Ayaz Siddiqui, Mitchell Cobb, and Chris Vermillion. Optimal Exploration and Charging for an Autonomous Underwater Vehicle with Energy-Harvesting Kite. *Proceedings of the American Control Conference*, 2020-July(i):4134–4139, 2020.

[24] Minesto: Power to change the world. `https://minesto.com/`.

[25] Windlift: Airborne power generator. `https://windlift.com/`.

[26] Makani. `https://x.company/projects/makani/`.

[27] Paul Williams, Bas Lansdorp, and Wubbo Ockels. Optimal Crosswind Towing and Power Generation with Tethered Kites. *Journal of Guidance, Control, and Dynamics*, 31(1):81–93, 2008.

[28] Luís Tiago Paiva and Fernando A.C.C. Fontes. Optimal Electric Power Generation with Underwater Kite Systems. *Computing*, 100(11):1137–1153, 2018.

[29] Joshua Daniels, James Reed, Ayaz Siddiqui, Mitchell Cobb, Michael Muglia, and Chris Vermillion. Optimal Cyclic Control of an Ocean Kite System in a Spatiotemporally Varying Flow Environment. In *Proceedings of the American Control Conference*, 2021.

[30] Mitchell Cobb, James Reed, Joshua Daniels, Ayaz Siddiqui, Max Wu, Hosam Fathy, Kira Barton, and Chris Vermillion. Iterative Learning-Based Path Optimization with Application to Marine Hydrokinetic Energy Systems. *IEEE Transactions on Control Systems Technology*, 2021.

[31] Boris Houska and Moritz Diehl. Optimal Control for Power Generating Kites. In *Proceedings of the European Control Conference (ECC)*, 2007.

[32] A. U. Zgraggen, L. Fagiano, and M. Morari. On real-time optimization of airborne wind energy generators. In *52nd IEEE Conference on Decision and Control*, pages 385–390, 2013.

[33] Debapriya Bhattacharjee, Miguel Alvarez Tiburcio, and Hosam Fathy. Co-optimization of the spooling motion and cross-current trajectory of an energy-harvesting marine hydrokinetic kite. In *2021 60th IEEE Conference on Decision and Control (CDC)*, pages 2065–2070, 2021.

[34] M. Alvarez, D. Bhattacharjee, H. Fathy, and C. Vermillion. An integrated model of the flight and tether dynamics of a marine hydrokinetic energy harvesting system. In *2021 European Control Conference (ECC)*, 2021.

[35] Debapriya Bhattacharjee, Miguel Alvarez Tiburcio, Daniel F. Opila, Christopher Vermillion, and Hosam K. Fathy. An Analytic Solution to the Inverse Dynamics of an Energy Harvesting Tethered Kite. *Journal of Dynamic Systems, Measurement, and Control*, 144(11), 08 2022.

[36] Debapriya Bhattacharjee, Miguel Alvarez Tiburcio, Daniel F. Opila, Christopher Vermillion, and Hosam K. Fathy. Co-optimization of the spooling and cross-current trajectories of an energy harvesting marine hydro-kinetic kite. *IEEE Transactions on Control Systems Technology*.

[37] Mitchell K. Cobb, Kira Barton, Hosam Fathy, and Chris Vermillion. Iterative learning-based path optimization for repetitive path planning, with application to 3-d crosswind flight of airborne wind energy systems. *IEEE Transactions on Control Systems Technology*, 28:1447–1459, 2020.

[38] Mitchell K. Cobb, Kira Barton, Hosam Fathy, and Chris Vermillion. Iterative learning-based path optimization for repetitive path planning, with application to 3-d crosswind flight of airborne wind energy systems. *IEEE Transactions on Control Systems Technology*, pages 1–13, 5 2019.

[39] Polzin Eva Ahbe, Tony A Wood, Henrik Hesse, Tony A Wood, Polzin Eva Ahbe, Polzin Eva Ahbe, Tony A Wood Henrik, Roy Hesse, and S Smith. Modeling, identification, estimation and adaptation for the control of power-generating kites. *IFAC-PapersOnLine*, 51:981–989, 2018.

[40] Zak Leonard, Samuel Bryant, Kartik Naik, Andrew Abney, Dillon Herbert, Hosam Fathy, Kenneth Granlund, Andre Mazzoleni, Matthew Bryant, and Chris Vermillion. Sensor fusion observer design and experimental validation for an underwater kite. In *2022 American Control Conference (ACC)*, pages 3114–3119. IEEE, 2022.

[41] S Kapp and M Kühn. A five-parameter wind field estimation method based on spherical upwind lidar measurements. *Journal of Physics: Conference Series*, 555:012112, dec 2014.

[42] P. Towers and B. Ll. Jones. Real-time wind field reconstruction from lidar measurements using a dynamic wind model and state estimation. *Wind Energy*, 19(1):133–150, 2016.

[43] B. M. Doekemeijer, S. Boersma, L. Y. Pao, and J. W. van Wingerden. Ensemble kalman filtering for wind field estimation in wind farms. In *2017 American Control Conference (ACC)*, pages 19–24, 2017.

[44] S. Boersma, B.M. Doekemeijer, M. Vali, Johan Meyers, and J.W. van Wingerden. A control-oriented dynamic wind farm model: Wfsim. *Wind Energy Science*, 3(1):75–95, 2018.

[45] B M Doekemeijer, J W van Wingerden, S Boersma, and L Y Pao. Enhanced kalman filtering for a 2d CFD NS wind farm flow model. *Journal of Physics: Conference Series*, 753:052015, sep 2016.

[46] W M Hollister, E R Bradford, and J D Welch. Using aircraft radar tracks to estimate winds aloft. *The Lincoln Laboratory Journal*, 2:555–565, 1989.

[47] John Osborne and Rolf Rysdyk. Waypoint guidance for small uavs in wind. In *Infotech@Aerospace*. American Institute of Aeronautics and Astronautics, 9 2005.

[48] Meir Pachter, Nicola Ceccarelli, and Phillip R. Chandler. Estimating mav's heading and the wind speed and direction using gps, inertial, and air speed measurements. In *AIAA Guidance, Navigation and Control Conference and Exhibit*. American Institute of Aeronautics and Astronautics Inc., 2008.

[49] Harish J. Palanthandalam-Madapusi, Anouck Girard, and Dennis S. Bernstein. Wind-field reconstruction using flight data. In *2008 American Control Conference*, pages 1863–1868. IEEE, 6 2008.

[50] Jan Petrich and Kamesh Subbarao. On-board wind speed estimation for uavs. *AIAA Guidance, Navigation, and Control Conference 2011*, 2011.

[51] Jack W. Langelaan, Nicholas Alley, and James Neidhoefer. Wind field estimation for small unmanned aerial vehicles. *Journal of Guidance, Control, and Dynamics*, 34:1016–1030, 7 2011.

[52] Je Hyeon Lee, Hakki Erhan Sevil, Atilla Dogan, and David Hullender. Estimation of maneuvering aircraft states and time-varying wind with turbulence. *Aerospace Science and Technology*, 31:87–98, 2013.

[53] Brian L. Stevens, Frank L. Lewis, and Eric N. Johnson. *Aircraft Control and Simulation*. Wiley, 2015.

[54] Egbert Torenbeek. *Synthesis of subsonic airplane design: an introduction to the preliminary design of subsonic general aviation and transport aircraft, with emphasis on layout, aerodynamic design, propulsion and performance*. Springer, Dordrecht, 1982.

[55] L. Beiner and S. W. Paris. Direct trajectory optimization using nonlinear programming and collocation. *Journal of Guidance, Control, and Dynamics*, 10(4):338–342, 1987.

[56] O. von Stryk and R. Bulirsch. Direct and indirect methods for trajectory optimization. *Annals of Operations Research*, 37(1):357–373, 1992.

[57] John P Norton. *An introduction to identification*. Courier Corporation, 2009.